

Silicon photonic crystal nanocavity modulator and receiver fabricated by photolithography

February 2019

A thesis submitted in partial fulfilment of the requirements for the degree of Doctor of
Philosophy in Engineering



Keio University

Graduate School of Science and Technology
School of Integrated Design Engineering

Nurul Ashikin Binti Daud

Abstract

Silicon (Si) photonics is considered a promising candidate as a key technology with which to develop optical interconnects due to the mature state of nanofabrication, together with the unique characteristics of Si, namely a high refractive index and a low absorption loss at telecom wavelengths, thus offering the advantage of confining light in a tiny device on a chip. Today, researchers are working towards accomplishing complementary metal-oxide-semiconductor (CMOS) compatible fabrication, which will allow Si photonic devices to be commercialized.

On the other hand, Si photonic crystal (PhC) has been attracting a lot of attention since it enables us to device high- Q nanocavities with small mode volume. This feature has facilitated various functional operations at a very low power. Hence, the integration of a Si PhC with Si photonics will allow us to expand the functionality of Si photonic systems. Although it is often claimed that existing Si PhC devices are compatible with CMOS and Si photonics, several challenges need to be met before integration is achieved.

This thesis discusses the fabrication of CMOS compatible high- Q Si PhC nanocavities and studies the functionality of these devices. CMOS compatible fabrication allows the device to be easily integrated with heaters and $p-i-n$ diode structures, and this enables us to demonstrate integrated optical modulator and receiver operation at a very low power.

[Chapter 1](#) describes the background and the motivation of this study. It reviews the current Si photonics and Si PhC technologies.

[Chapter 2](#) presents the theory. It describes the principle of photonic bandgap and the formation of nanocavity in a PhC. The design strategy for achieving a high- Q PhC nanocavity is described.

[Chapter 3](#) presents the fabrication process of the PhC device with the integration of a $p-i-n$ diode structure. A very high Q of 2.2×10^5 is achieved with a $p-i-n$ integrated Si PhC nanocavity that is fabricated photolithographically and have SiO_2 clad structure.

Chapter 4 reports the demonstration of a PhC nanocavity device as an electro-optic modulator by injecting a carrier into a *p-i-n* diode. Refractive index modulation is demonstrated via the carrier plasma dispersion effect, with modulation voltage of 1.0 V at a speed of 0.35 GHz.

Chapter 5 reports the demonstration of a PhC nanocavity device as a photoreceiver with the help of two-photon absorption. A small dark current of 38 pA with a minimum detectable power of 10 μ W is obtained.

Chapter 6 describes a transmittance experiment using a Si PhC nanocavity modulator and receiver. This demonstration shows that an all-silicon transmission link is achievable.

Chapter 7 summarizes the content of each chapter and concludes the thesis.

List of abbreviations

1D	One dimensional
2D	Two dimensional
3D	Three dimensional
AC	Accumulative current
Al	Aluminium
BPF	Band-pass filter
CMOS	Complementary metal-oxide-semiconductor
CW	Continuous wave
DC	Direct current
EB	Electron beam
EDFA	Erbium-doped fiber amplifiers
EO	Electro-optic
FDTD	Finite difference time domain
FWHM	Full width at half maximum
GaAs	Gallium arsenide
Ge	Germanium
InP	Indium phosphate
IR	Infra-red
MZI	Mach-Zehnder Interferometer
NRZ	Non-return zero
OE	Opto-electric
OSC	Oscilloscope
PBG	Photonic bandgap
PD	Photo detector
PhC	Photonic crystal
PM	Power meter
PPG	Pulse pattern generator

LIST OF ABBREVIATIONS

PRBS	Pseudo-random bit sequence
PW	Plane wave
RF	Radio frequency
Rx	Receiver
SEM	Scanning electron microscopic
Si	Silicon
SiO ₂	Silica
TE	Transverse electric
TEC	Thermoelectric temperature controller
TIA	Transimpedance amplifier
TIR	Total internal reflection
TLD	Tunable laser diode
TM	Transverse mode
TO	Thermo-optic
TPA	Two-photon absorption
Tx	Transmitter
VOA	Variable optical attenuator
Wg	Waveguide

Contents

Abstract	i
List of abbreviations	iii
Chapter 1 Introduction	1
1.1 Integrated Silicon Photonics and data centers	2
1.2 Photonic crystal	4
1.2.1 One-dimensional PhC	5
1.2.2 Two-dimensional PhC.....	6
1.2.3 Three-dimensional PhC.....	10
1.3 Optical signal processing	12
1.3.1 Electro-optic modulator.....	12
1.3.2 Photoreceiver.....	14
1.3.3 Optical transmission link.....	16
1.4 Purpose of Study	18
1.4.1 Motivation	18
1.4.2 Objective	19
Chapter 2 Theory of Photonic Crystal	21
2.1 Introduction	21
2.2 Photonic band structure	22
2.2.1 Maxwell's equation	22
2.2.2 Cavity formation	27
2.3 Fabry-Pérot Cavity	30
2.4 Method of analysis	32
2.4.1 Plane-wave (PW) method.....	32
2.4.2 Finite difference time domain (FDTD) method	37
2.5 PhC nanocavity design structure	40
2.6 Summary	43
Chapter 3 PhC nanocavity laterally embedded with <i>p-i-n</i> diode fabrication process	44
3.1 Introduction	44
3.2 Overview of PhC fabrication process.....	45
3.3 Photolithography fabrication procedure.....	46
3.3.1 Device fabrication process	46
3.3.2 Integration of <i>p-i-n</i> diode	50

3.4	Comparison with previous study's device.....	51
3.5	Summary	52
Chapter 4 Electro-optic modulator based on PhC nanocavity		53
4.1	Introduction	53
4.2	Motivation	54
4.3	Spectrum characteristics.....	55
4.3.1	DC voltage operation	56
4.3.2	Radio-frequency (RF) operation	59
4.4	Electro-optic (EO) modulations	61
4.5	Discussion	62
4.6	Summary	64
Chapter 5 PhC nanocavity photoreceiver		65
5.1	Introduction	65
5.2	Motivation	66
5.3	Photoreceiver properties.....	67
5.3.1	Dark current.....	67
5.3.2	Transmission spectrum and photocurrent.....	68
5.3.3	Responsivity	69
5.4	Photoreceiver operation.....	70
5.5	Discussion	72
5.6	Summary	74
Chapter 6 All-Si scheme PhC nanocavity transmission link		75
6.1	Introduction	75
6.2	Challenges and motivation	76
6.3	Electro-optic modulator performance	77
6.4	Opto-electric receiver performance.....	78
6.4.1	Basic design structure.....	78
6.4.2	Design characteristics.....	80
6.4.3	Demonstration of OE receiver.....	81
6.5	Temperature dependence operation.....	82
6.6	All-Si scheme PhC transmission link demonstration	84
6.7	Discussion	85
6.8	Summary	86
Chapter 7 Summary and outlook.....		87
7.1	Summary of each chapter	87

7.1.1	Theory of photonic crystal (Chapter 2)	87
7.1.2	PhC nanocavity laterally embedded with <i>p-i-n</i> diode fabrication process (Chapter 3).....	88
7.1.3	Electro-optic modulator based on PhC nanocavity (Chapter 4).....	88
7.1.4	PhC nanocavity photoreceiver (Chapter 5)	89
7.1.5	All-Si scheme PhC nanocavity transmission link (Chapter 6)	89
7.2	Conclusion and outlook of the thesis	89
References		92
Acknowledgments.....		106
List of publications		108
Appendix A Product values of optical equipment's		111
Appendix B Loss measurement of PhC device		112

Chapter 1

Introduction

The use of light for communication purposes has begins in early years of civilization. Reflection of light through mirrors, fire beacons or smoke signal are used to convey an information at some distance. For example, in 1084 B.C., Greeks civilization constructed a 500 km long line fire beacons to convey news of victory [1]. Through years, researchers are trying to manipulate light as medium of communication to carry information signals at distance due to its fast speed. Only in 1966, with the advancement of technology, low-losses optical fibers has been invented and become the best choice for optical communication. Since fibers are capable of guiding light in similar confinement of electrons inside copper wire, optical communication has become widely used in telecommunication technology.

Nowadays, telecommunications network has expanded the entire world. Transmitting an information signal no longer required a long time. Signal can be received within a minute although it was transmitted over a far distance. Therefore, previous decades have witnessed an explosive increasement in the volume of global network. In 2015, amount of annual global data center traffic already reached 1021 bytes and estimated to be triple by 2020 [2]. Data intensive applications such as streaming video, social network and cloud computing require data center to provide extremely high bandwidth communication. Transporting such increasing volume of data with existing technologies such as the conventional metallic interconnects, will not able to satisfy the exponentially increasing capacity demands. This is because the conventional interconnects are limited by the finite resistance and capacitance, soon will reached its limit [3]. Meanwhile, the scale expansion of data center will consume huge power. Therefore, efficient interconnection scheme with low cost, high energy efficiency and high bandwidth capacity is in a great need.

Currently, present work is concerned with monolithically integrated optics on a silicon platform, for example, silicon photonics. Fuelled by modern society's consumption of digital electronics, silicon manufacturing technology nowadays represent an extremely mature process that has had half a century of continuous, law-like [3], exponential improvements and breakthroughs.

Photonic crystal, on the other hand, is a material where the refractive index change periodically [4], may hold the key to continue the progress towards all-optical integrated circuits. Photonic crystal is characterized by the formation of band structures with respect to energy of photon. Thus, various type of engineering focusing on band gap, band edge and photons manipulation has been investigated to broad the application of photonic crystal to optical chip and functional devices.

In this chapter, the integration of silicon photonics with electronics will be discussed in detail. Next, the introduction about photonic crystal and their characteristics will also be explained in this chapter. Then, a few examples of optical signal processing will be introduced. Finally, the purpose of this study is described.

1.1 Integrated Silicon Photonics and data centers

Nowadays, data rates have becoming a great attention in order to achieve high transmission signals. According to Moore's Law, electronic transmission is facing a breaking point when the ability of copper wire has come to its limit. Fig. 1.1 illustrates the numbers of transistors on a chip as a function of year. The trend shows the number of transistors is increasing over year. Thus, more power is needed to carry data in high speed over a long distance. Therefore, scientist introduced the integrated photonics to transform communication industry expecting to downsizing the size, mitigate the fabrication cost and achieve better performance.

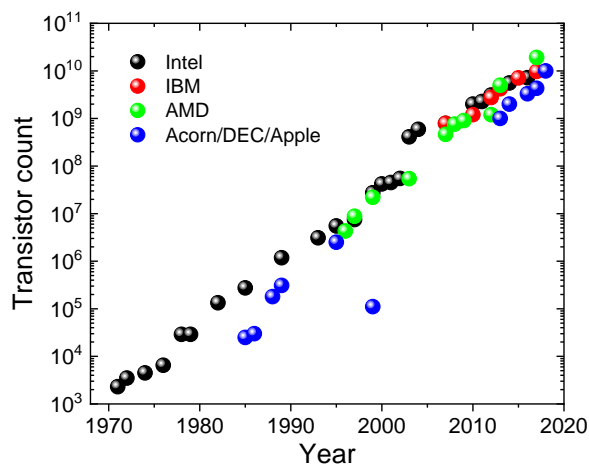


Fig. 1.1 Number of transistors as a function of time based on different processor's company. Black, red, green and blue refer to Intel, IBM, AMD and Acorn/DEC/Apple, respectively. [https://en.wikipedia.org/wiki/Transistor_count]

Instead of utilizing electrons, integrated photonics use light. It is possible to perform in wide variety application involving optical functions. The dimension of integrated photonics has been expanded due to the recent development in nanostructures and silicon technologies. This has led to the transformation in optical devices field technologies for many applications including optical networks, optical interconnects, lab on chip etc. Silicon photonic has been targeted at applications in intra-chip and inter-chip optical interconnects. It is expected to solve the bottlenecks of metal electrical interconnects at high data rates by delivering optical connectivity everywhere from the network level to chip-to-chip level.

Present work on silicon photonics focuses in data center networks. In a sense, data centers are at the core of the internet, with virtually all internet traffic ending up in data center server. With the massive popularization, within the last decade, of cloud computing, cloud storage, streaming media and mobile computing devices, data center traffic has growth rapidly. By 2015, the number of networked devices equal to two times of the global population. The number is expected to rise more with the increasing of years. Such massive growth will become a challenge for future scalability and lead to network congestion. Therefore, to help combat the rapid growth in the bandwidth demand of data center networks, all-optical networking technology is introduced, for rack-to-rack and board-to-board communications, to replace bandwidth-limiting electronic components.

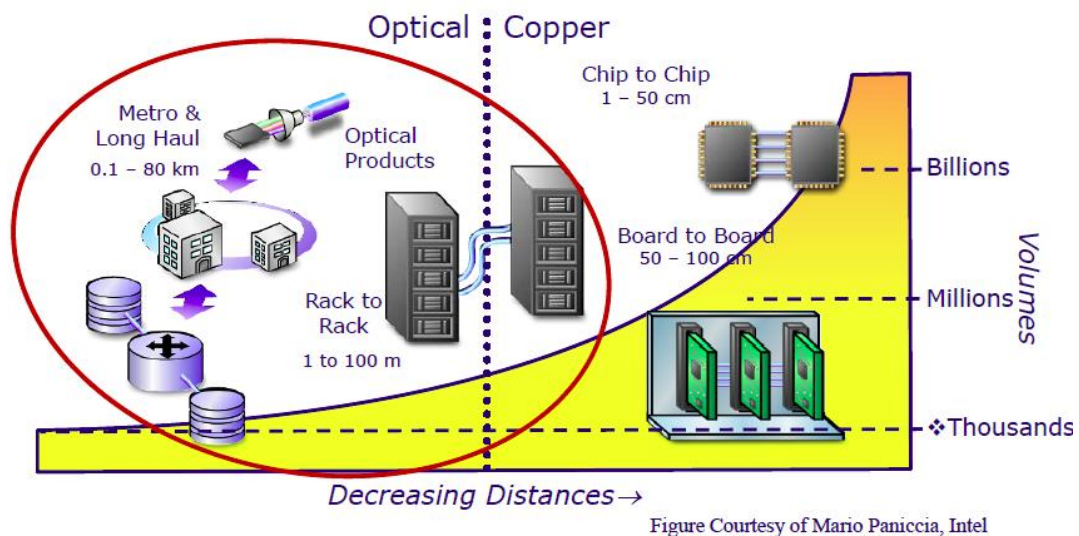


Fig. 1.2 Battle between optics and copper.

However, future data center networks are expected to scale to millions nodes [5], [6], which will require compact, energy efficient and easily manufacturable components. This poses a problem for conventional off-the-shelf optical components, which are bulky, consume many watts of power and relatively expensive to manufacture. Therefore, silicon photonics which relatively inexpensively in term of manufacture due to wafer-scale processing, becomes an obvious candidate for use in future data center networks.

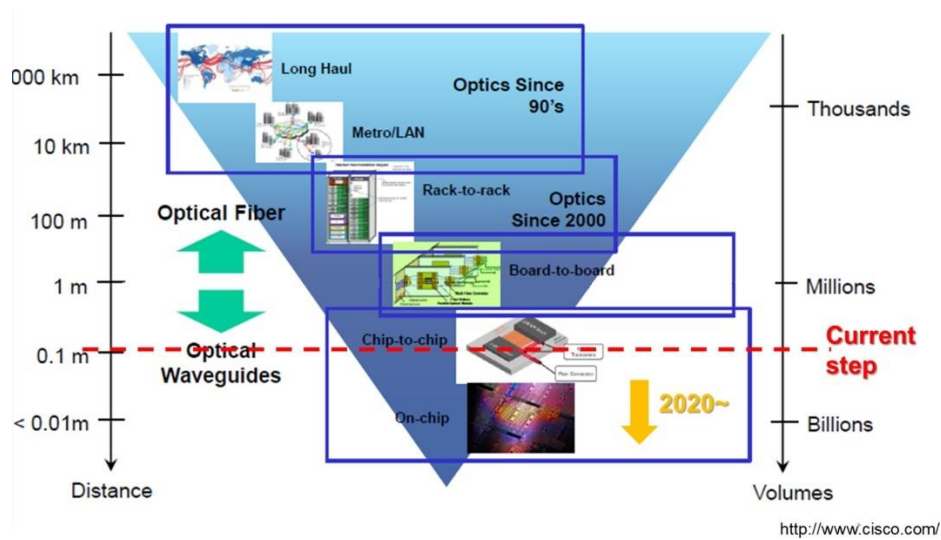


Fig. 1.3 Development of optics in data center since 90's.

1.2 Photonic crystal

Photonic crystal (PhC) is a periodic dielectric structure. PhC exist in nature, for example wings of butterfly and it also can be artificially fabricated. Although scientist from America, Yablonovitch, has become the pioneer in PhC when he claimed that spontaneous emission can be controlled through electromagnetic band gap of periodic dielectric structure [4], the study of the periodic structure has been started hundred year ago by Lord Rayleigh [7]. Rayleigh discover that band gap can be achieved in one-dimension periodic structure. However, in early year, this phenomenon was ignored by the photonics community. Then, S. John reported that Anderson localization of photon can be achieved by including certain amount of disorder in superlattice structure [8]. At that period, name of 'photonic crystal' has not been introduced yet until Yablonovitch and Sajeev met each other [9].

The advantage of PhC structure is not only lies on the ability to manipulate light or photon but also the miniaturization of the structure due to the small mode volume. Together with the developing fabrication technologies, it is possible to fabricate such compact PhC devices. The direction of application of PhC devices currently is towards communications filed since photons are excellent in transmitting information. Various devices of optical interconnect have been introduced and demonstrated by all PhC structures.

PhC structure can be formed in three different dimensions as shown in Fig. 1.4. Each dimension has different structure and application. The structure and application will be discussed in following section.

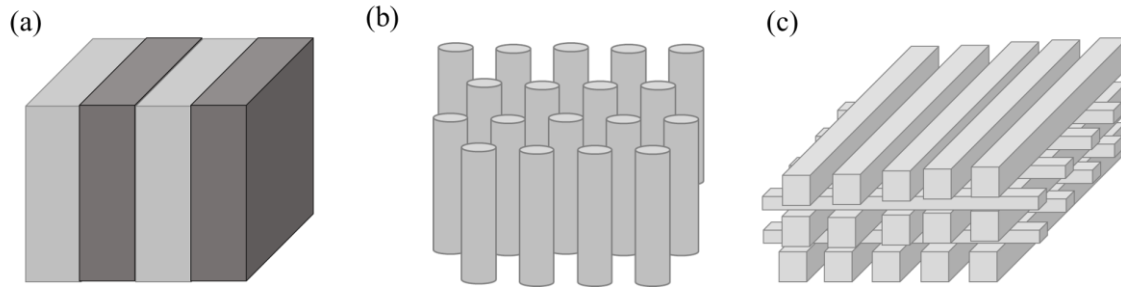


Fig. 1.4 Schematic illustration of PhC structures (a) one-dimensional (1D) (b) two-dimensional (2D) (c) three-dimensional (3D)

1.2.1 One-dimensional PhC

One-dimensional (1D) PhC nanocavity has a simplest structure in PhC as shown in Fig. 1.4 (a). The investigation of 1D PhC structure has been done by L. Rayleigh in 1887 [7]. Compared with 2D and 3D PhC, 1D PhC is easy to integrate with other existing photonic devices due to the simple structure without changing fabrication procedures. 1D PhC structure is mainly used in grating couplers. Grating couplers are a device that can diffract light from propagation in the waveguide to free space. By placing an optical fiber above the chip, part of the radiated light is collected. Usually, a grating coupler is used as an I/O device to couple light between fiber and sub-micrometer silicon waveguides. It can be placed anywhere on the surface of the chip to enable input and outputs. Fig. 1.5 shows an illustrated cross section view of a grating coupler. The thickness of the buried oxide layer is determined by the wafer type. The study of grating couplers was first proposed in 1970 [10]. In this paper, the method of coupling light into a thin-film optical waveguide using a grating coupler was first introduced. Then, study and application of grating couplers began to expand extensively [11]–[15].

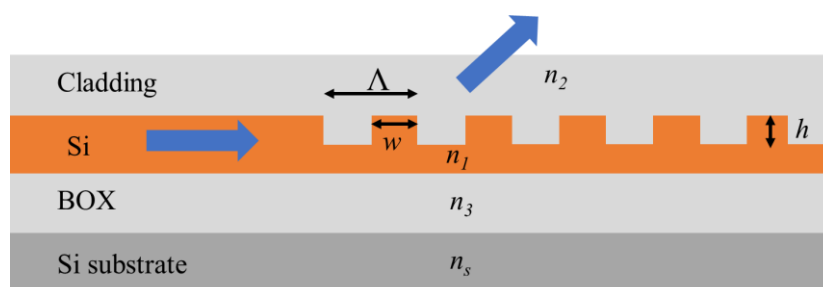


Fig. 1.5 Schematic illustration of cross section view grating coupler. The thickness, h is normally 150 – 300 nm. The cladding material is usually air ($n_2 = 1$), silicon dioxide or index-matching liquid ($n_2 \sim 1.45$)

Another usual application of 1D PhC structure is nanobeam structure. A feasible nanobeam structure operating at 1.55 μm wavelength was first fabricated in 1995 [16] and first reported experimental Q factor of this structure was 265 [17]. Q factor is a measured value to evaluate the ability of light confinement in a designed structure. The investigation of design,

fabrication and experimental characterization of PhC nanobeam then continue to improve the value of Q . In 2009, Q of 10^5 has been reported by Loncar's group [18] and later, the same group have reported with an optimized of nanobeam structure is possible to achieved a theoretical highest Q of $>10^9$ [19].

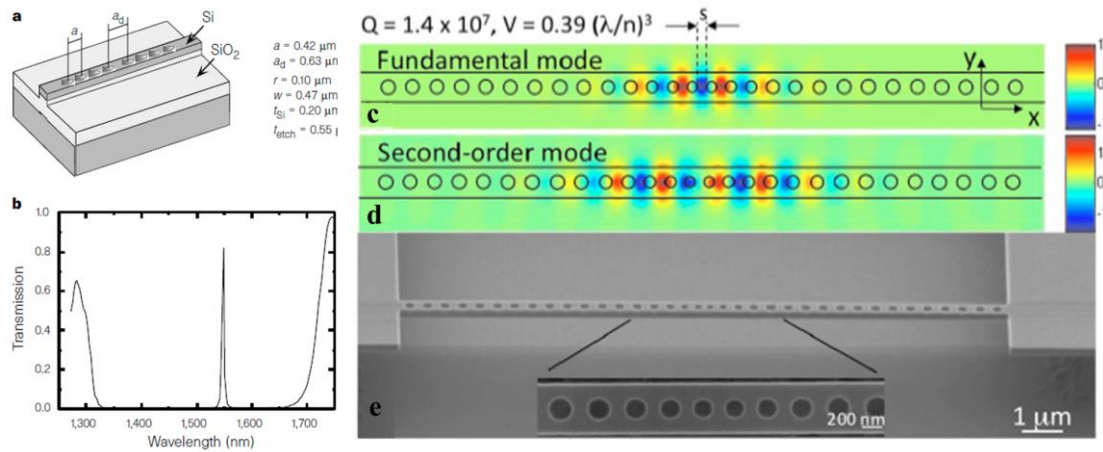


Fig. 1.6 (a) Schematic illustration of PhC waveguide microcavity with dimension for operation at $1.54 \mu\text{m}$. The parameter of hole period, a , defect length, a_d , hole radius, r , waveguide width, w , silicon thickness, t_{Si} , and total etch depth through both Si and SiO_2 are described. (b) Computation and transmission through the structure. Resonance appeared at 1547 nm with Q of 280. [Reprinted with permission J.S. Foresi *et al.*, Nature **390**, 1997] (c) and (d) Electric field (E_y) profiles of two cavity modes. Q and V are quoted for the optimal cavity length, s . (e) SEM image of fabricated PhC nanobeam cavity with 220 nm thickness and 500 nm width. The photonic mirror pitch $a = 430 \text{ nm}$ is linearly tapered over five hole section to $a = 330 \text{ nm}$ at the cavity center. The hole radius is $r = 0.28a$ and the band gap extends from $1200\text{-}1700 \text{ nm}$. [Reprinted with permission P. B. Deotare *et al.*, Appl. Phys. Lett. **94** (121106), 2009]

Although the development of 1D PhC structures later compared to two-dimensional PhC structure, due to the extraordinary ability where it allows refractive index distribution along one direction and localization of light in a small region area, makes this structure compact. Owing to the compactness, it has widely used for wide range of application with high performance [20]–[23].

1.2.2 Two-dimensional PhC

Two-dimensional (2D) PhC structure, has become more dominant in PhC structures due to the possesses periodicity of the permittivity along two-direction. Because of that, it is possible to have large variety of configuration. The study of 2D photonic band structures was first theoretically conducted by M. Plihal, who is investigating the electromagnetic waves of photonic band structure that consists of long, parallel and dielectric rods of periodic array constitute a square lattice [24] and on the same year, the same method was conducted to calculate for a

triangular lattice [25]. Later the demonstration of microwave transmission was performed to verify that light could not propagate in the 2D complete band gap structure at any polarization [26].

Since the application of 2D PhC structures are depending on the ability to control and confine light, several methods has been introduced to manipulate photons in the structure which is 1) band-gap nanocavity and 2) mode-gap nanocavity.

1) Band-gap nanocavity occurs when defect is introduced within a photonic band gap and light is confined with surrounding band-gap. This strategy has been introduced by Yablonovitch to form a high Q through donor and acceptor modes concept in 3D periodic dielectric structure [27]. Then, few years later, the donor and acceptor modes strategy has been utilized in 2D microfabricated hexagonal array PhC structure theoretically and experimentally [28], [29]. The light confinement occurs through the presence of defect by removing a single hole as shown in Fig. 1.7. Due to the total internal reflection, photons are localized vertically at the slab interface. 3D confined optical mode was achieved because of the combination of Bragg reflection from 2D PhC and total internal reflection from the low index cladding of air. The value of Q experimentally measured was 250, however, by tailoring the interhole spacing and radius holes, value of Q can be further improved to 1500. The structure has been demonstrated as microcavity laser and pulsed lasing action was observed at 1.5 μm wavelength.

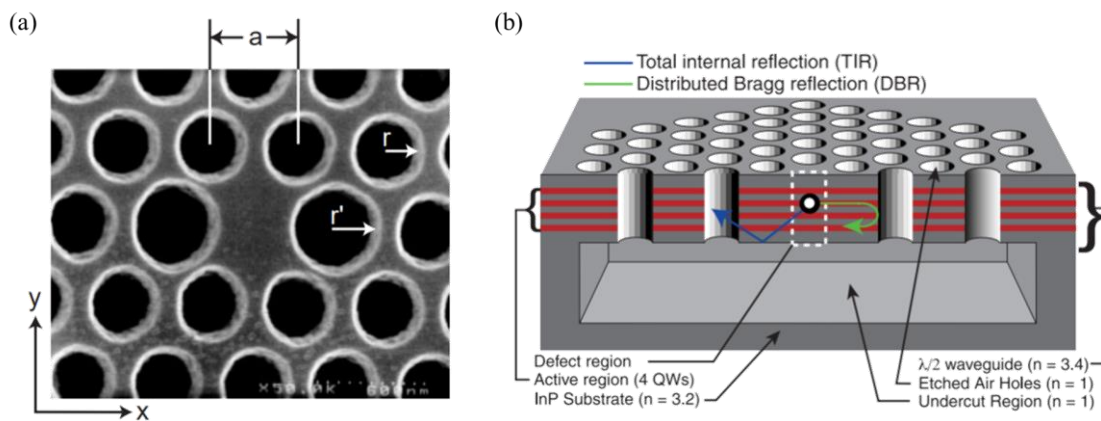


Fig. 1.7 (a) SEM image of top view of a microfabricated 2D hexagonal array of air holes in a thin membrane with a missing hole at the center. The interhole spacing, a is 515 nm and the radius holes, r is ~ 180 nm. The two enlarged holes which radius, r' of 240 nm, are used to split the dipole mode degeneracy. (b) Cross section through the middle of the PhC microcavity. A defect is formed by removing a single hole. [Reprinted with permission O. Painter *et al.*, Science **284**, 1999]

Then, the value of Q is further improved by the introduction of L3 nanocavity by Noda's group [30]. The structure consists of three missing air holes in a line at the center as shown in Fig. 1.8 (a) of the structure so that Bragg reflection at the in-plane direction occur and light can be confined. In order to obtain high Q , they have modified the Bragg reflection condition by shifting the air holes at both cavity edge $0.15a$ from original position. The theory is, by the shifting of air holes position, changed the phase of partial reflections at the air holes, and thus, the phase mismatch occur which will weaken the Bragg reflection. Light then will penetrate more inside the mirror

and will be reflected perfectly. Fig. 1.8 (b) shows the experiment results of various air holes distance shift and their corresponding spectrum. The highest value of Q was 45000 was obtained when the air holes were shifted by $0.15a$. Thereafter, the tuning was performed not only adjacently to the nanocavity but also for those two and three points away [31] where the Q was improved to 100000. With the high Q obtained, the application of such device was studied. All-optical switching devices [32]–[34] and semiconductor laser [35] has been demonstrated.

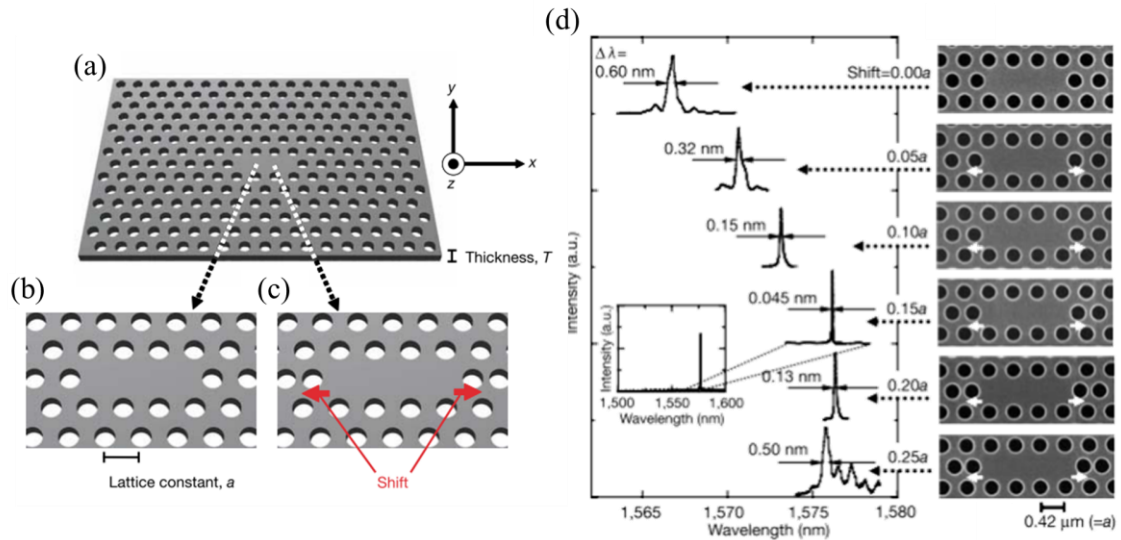


Fig. 1.8 (a) Schematic of cavity structure of triangular lattice air holes with lattice constant, a is $0.42 \mu\text{m}$, thickness, T of $0.25 \mu\text{m}$ and radius R of $0.12 \mu\text{m}$. (b) Cavity structure with three missing air holes in a line. (c) Method of enlarging the Q of a donor-type defect by displacing the air holes at both edges. (d) SEM image of a nanocavity with various shifting distance and corresponding resonance spectrum. [Reprinted with permission Y. Akahane *et al.*, Nature **425**, 2003]

2) Mode-gap nanocavity is formed with different lattice constant or width of waveguide in PhC structure. Noda's group has introduced a mode-gap nanocavity by triangular lattice double heterostructure nanocavity as shown in Fig. 1.9 [36]. The structure consists of missing row of air holes which formed a waveguide that allows propagation of photons and PhC with two different lattice constants, a_1 and a_2 are introduced to the structure (I and II) to differ the transmission and mode-gap regions. Therefore, only photons with specific energy can exist in the PhC waveguide II and with the short length of waveguide in PhC II will limit the frequency of photons exists in the region and nanocavity was formed. The difference of lattice constant between PhC I and II gives a mode-gap effect. Therefore, by changing the difference of lattice-constant between two crystals, can controlled the evanescent behaviour of electric field confined. The structures achieved high Q of 600000 through experiment and theoretically 20000000 with the optimization structure.

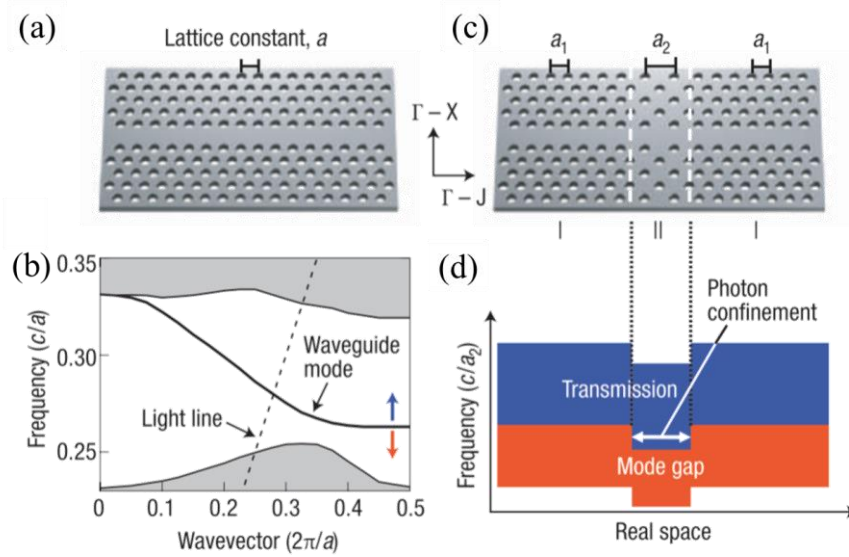


Fig. 1.9 (a) 2D PhC slab of triangular lattice structure with line-defect waveguide formed by a missing row of air holes. (b) The calculated band structure for (a). The blue arrow indicates the transmission region where the propagation of photons is allowed through the waveguide and the red arrow indicates the mode-gap region in which the propagation is inhibited. (c) Photonic double heterostructures, constructed by connecting the basic PhC structures I and II. PhC I have a triangular lattice structure with lattice constant of a_1 while PhC II has a deformed triangular lattice structure with a face-centered rectangular lattice of constant a_2 ($>a_1$) in the waveguide direction; it retains the same constant as PhC I in the orthogonal direction to satisfy the lattice-matching conditions. (d) Schematic of the band diagram along the waveguide direction. Photons of a specific energy can exist only in the waveguide of PhC II. [Reprinted with permission B.S Song *et al.*, Nat. Mater. **4**, 2005]

Another structure of mode-gap nanocavity which has been introduced is width modulated line-defect cavity [37]. The cavity structure was created by modulating the holes parameter of line-defect waveguide to create local confinement as shown in Fig. 1.10 (a). The mode-gap in this cavity is realized by the difference of waveguide width once the holes parameter is modulated. The band diagram of the structure as shown in Fig. 1.10 (b) shows that the difference in the cut-off frequency of TE mode, between W0.98 waveguide and the cavity allow light to be confine. This structure allows local light modulation with small number of shifting holes that gives a great advantage to the cross-packed integration of PhC slab device. The study able to achieve value of Q factor 10^5 .

This nanocavity structure has been demonstrated as an all-optical switching in which consumed low energy consumption and fast all-optical switching [38], [39]. With the unique properties of PhC structure and together with the advancement of the fabrication technologies nowadays, researchers are now move towards the integration of PhC devices with CMOS electrical circuits.

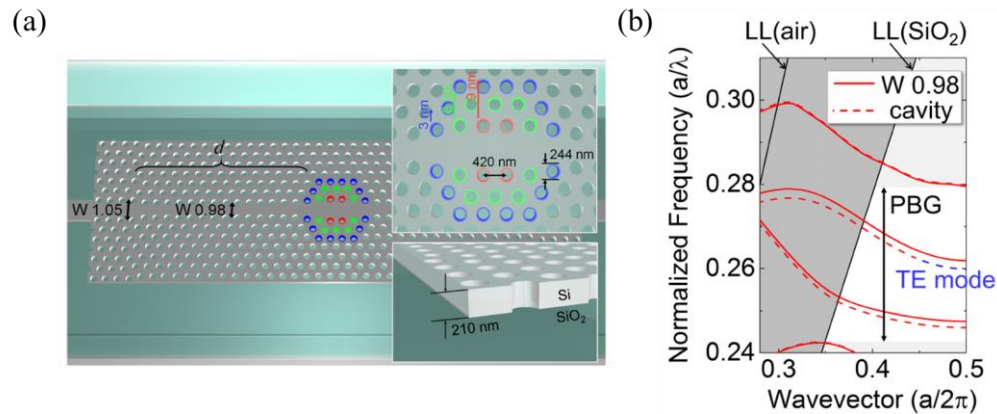


Fig. 1.10 (a) Schematic illustration of width-modulated line defect PhC nanocavity. The center airholes was shifted to some position from their original position. d is the number of barrier region that set the strength of coupling and confinement. (b) Band diagram dispersion of the line defect with SiO_2 cladding. The solid red line represents the dispersion of the barrier $W=0.98$ waveguides without cavity and the dashed line represents when the waveguide width is 18 nm wider with cavity hole shifts.

1.2.3 Three-dimensional PhC

In 3D structure, photonic band gap formed in all direction. Therefore, a complete photonic band gap is formed with 3D PhC structure. The schematic of 3D PhC structures shown in Fig. 1.4 (c). The photonic band structure of 3D PhC has first introduced by Yablonovitch [40]. He has proven that full 3D photonic band gap is achievable in some type of dielectric structure and the forbidden gap can be created in microstructures which agrees to practical microfabrication. Many works are donated to the design of new geometric configuration of 3D PhC, which open new possibilities of applications. Stone opal is one of the famous naturally formed of 3D PhC which has a unique optical property as shown in Fig. 1.11. Different colour will appear when the stone is turned around in which ancient people believe the stone opal have a magic power. It is consisting of a number of microspheres placed at nodes of face-centered cubic lattice where reflectance is depending on the radiation angle.

Similarly, with 1D and 2D PhC structure, 3D PhC structure also has an ability of light confinement. Recently, high Q factor was reported to achieve 93,000 [41] as shown in Fig. 1.12. The high Q factor is expected to achieve less threshold less lasing oscillation for 3D light confinement. Although 3D PhC structure is an ideal structure due to the complete photonic band gap characteristics, the fabrication of the structures is difficult compared to 2D and 1D PhC. So far, there is no reliable technology to fabricate this structure at optical telecommunication wavelength. Therefore, most of 3D PhC focus on fabrication method [42], [43].



Fig. 1.11 Image of stone opal which has unique optical property. The colour of the stone will change when the stone is turned around. [<https://www.gia.edu/opal>]

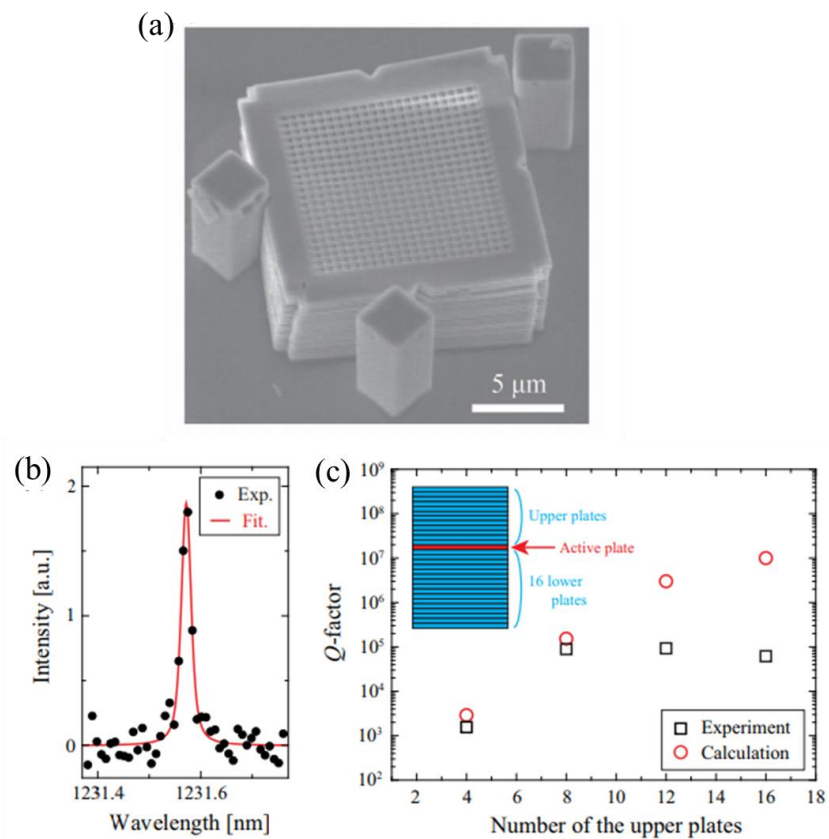


Fig. 1.12 (a) SEM image of stacked sample having 16 lower plates, single active plate and 16 upper plate. (b) Photoluminescence spectrum around 1231 nm for an input power of $4.35 \mu\text{W}$, which is below threshold power of $4.59 \mu\text{W}$. Red curved shows the fitting to evaluate the Q factor. (c) Experimentally and numerically obtained Q factor of upper plates. [Reprinted with permission S. Takahashi *et al.*, Electronics Letters **54** (5), 2018]

1.3 Optical signal processing

Optical signal is an optical communication that utilizing light to transmit the signal instead of electrical current and signal processing is a process to analysis, synthesis and conversion of signal. So, optical signal processing is a process that utilize light to analyse and make a modulation of signal before the signal is received to the receiver. Nonlinear devices, analog and digital signals and advanced data modulations are the examples of optical signal processing fields that has been extensively study among the researchers. In this section, some of the basic optical devices is discussed – namely, electro-optic modulator and photoreceiver – to bridge the electrical circuit with photonics through electro-optic and opto-electronic conversion. Next, the combination of the transmitter and receiver in a single housing is discussed.

1.3.1 Electro-optic modulator

Electro-optic modulator (EOM) is one of main material for optical interconnect. It modulates (makes the fundamental characteristics become vary) a light beam propagating either in free space or in an optical waveguide. An optical modulator can alter different beam parameters, allowing them to be categorized as either amplitude, phase or polarization modulators. There are two types of modulator namely, electro-absorptive modulator and electro-refractive modulator. Electro-refractive modulator works when electric field is applied to the material and changed its real part of refractive index. A change of refractive index in the imaginary part is known as electro-absorptive modulator. In semiconductor material, Pockels' effect and Kerr effect are mainly the electric field effects that usually caused electro-refractive or electro-absorptive. However, in pure silicon telecommunication wavelength, Pockels' and Kerr effect are weak [44]. Hence, other approach is necessary for the realization of silicon modulation.

In early years, lithium niobite (LiNbO_3) modulator has been proposed due to the fact that it possesses a large electro-optic coefficient [45], enabling optical modulation via Pockels' effect. In 1973, thin-film LiNbO_3 electro-optic light modulator with maximum bandwidth of 3.2 GHz has been proposed [46]. Then, the bandwidth performance has been improved and currently, LiNbO_3 modulator has become commercialized [47]–[50]. Although performance of LiNbO_3 has been improved, the device still suffers for a large foot-print thus, which led to high power consumption.

The dominance of Si as semiconductor, eventually led to the investigation of Si photonic circuits. This is because, Si material has potential attraction of integration with electronics in a cost-effective manner. In addition, since silicon modulation is possible to achieve by the changes of refractive index as experimentally proven by Soref [44], researchers are towards silicon-based material of modulator due to the unique properties of silicon. In 1987, Si has been proven for guided-wave modulator and switches applications because its ability to exhibits electro-refraction effects and free-carrier dispersion effect [51]. Since then, research regarding Si modulator become vigorously among researchers.

However, in early years, silicon waveguide based optical modulator was generally slow. However, early 2000s, performance of optical modulator has been optimized and reported possible to operate at high-speed operation of MHz and GHz [52]. In 2012, Mach-Zehnder Interferometer (MZI)-based modulator which operate via carrier depletion technique has obtained a highest bandwidth of 50 Gbit/s [53]. Carrier depletion technique manipulated free-carrier

densities in a modulator to avoid speed limitation posed by minority carrier lifetime. Device that employ this technique usually operates at reverse bias voltage. Another technique is carrier-accumulation which has been demonstrated using MZI-based modulator [54]. It has reported the operating bandwidth of the device is at 10 Gbit/s.

MZI-based silicon modulator has proven to achieve a high operating bandwidth. Although MZI-based modulator has shorter device length compared to LiNbO₃ modulator, but still much shorter devices are desired. Therefore, resonant-based modulator is introduced. The resonant-based modulator usually small and compact in size. Therefore, resonant-based structure modulator is expected possible to reduce power consumption of the device. Active high-speed ring resonators were first introduced by Xu *et al.* in 2005 [55]. A carrier injection scheme is employed and 1.5 Gbit/s initial data rate is achieved. Then, carrier-depletion technique is employed to further enhance the modulation [56].

Although significant foot-print can be reduced with resonant-based structure, this kind of modulator has a narrowband application due to the narrow modulation range of resonance wavelength. This, however, could limit their application.

Since PhC possible for large-scale integrated optics, and its ability to achieve slow group light velocity, PhC-based MZI modulator has been demonstrated [57]–[60]. On the other hand, PhC-based on resonant structure also has been demonstrated [61].

The performance of EOM device based on its modulation speed and depth, optical bandwidth, insertion loss, footprint and power consumption. However, those metrics of performance involve trade-off. For example, MZI-based modulator, is suffer from the large dimension although it shows a good performance at higher operation bandwidth. If we are towards reducing the dimension, it will be reducing the modulation depth. For ring resonator, in order to increase the optical bandwidth, cascading multiple ring is necessary, as a result it will increase the footprint and complexity in fabrication. Therefore, the performance of modulator is optimized based on its application. In case of sensing application, only moderate modulation speed is required. Fig. 1.13 shows the development of electro-optic modulator by comparing their performance.

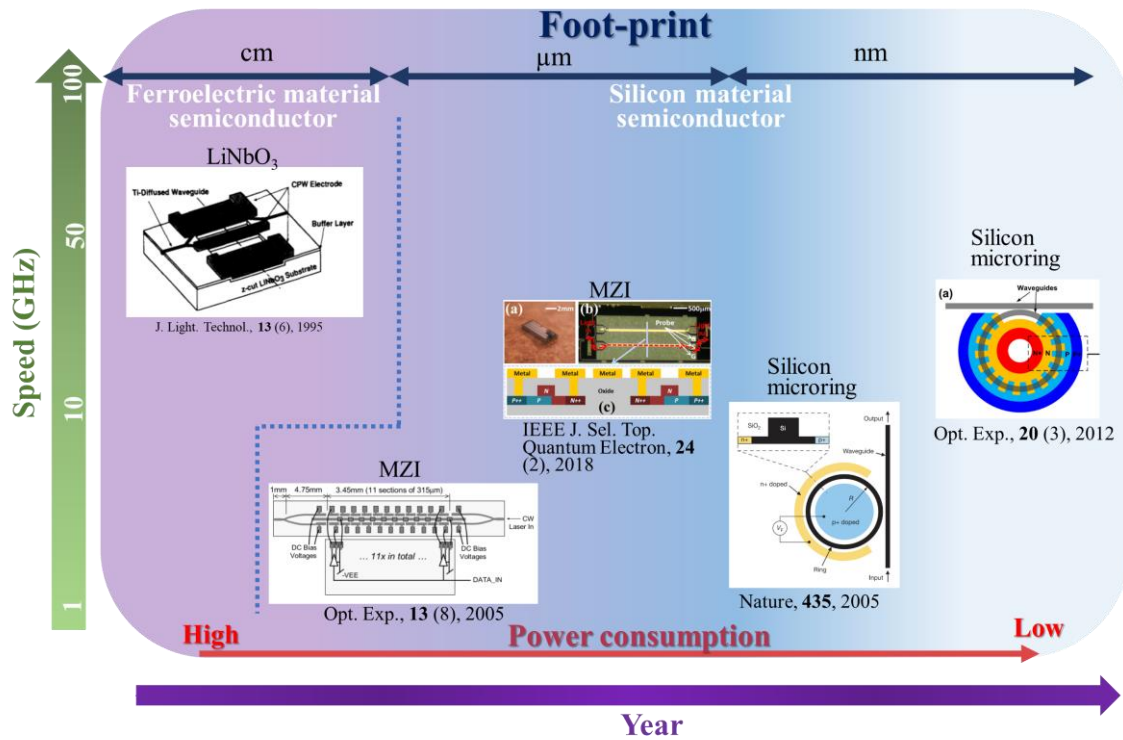


Fig. 1.13 Development of electro-optic modulator by comparing their performance between speed, size and power consumption.

1.3.2 Photoreceiver

Photoreceiver also known as photodetector or photosensor where it used to sense light or electromagnetic radiation and converts into electrical signal. The operation of light conversion is also known as opto-electronic (OE) operation. In early years, the optical detectors are evolved in III-IV semiconductor compound due to the wide detection ability of wavelength [62]. It also shows an ability for higher speed detection operation due to the high absorption coefficient characteristics.

With the invention of integrated circuit and CMOS technology, optical devices that has a higher degree of integration and compatible with CMOS process has become a trend. In particular, the realization of high-performance silicon-based photodetector becomes a great interest among researchers [63].

Silicon photodiodes are excellent detectors at visible wavelengths, but the development of Si photodetectors operating at wavelengths of interest for telecom and datacom is not straightforward, as Si is transparent at wavelengths larger than 1.1 μm . Conventional Si-based photodetectors at telecom wavelengths utilize integration with other material systems such as III-V compound semiconductors (InGaAs, InGaAsP, InGaAlAs, etc. [64]–[66]) and Ge. However, the 8.1% lattice mismatch between InGaAs and Si makes monolithic integration with CMOS circuit difficult, so a hybrid integration approach is required.

Ge on Si photodetectors, requires growth of Ge on a Si substrate. It can operate up until 10 Gbs^{-1} with high responsivity. However, the devices suffer for high leak current ($\sim 500 \text{ nA}$) [67], [68]. However, recently, J. Cui *et al.* has enhanced the performance of Ge on Si photodetector with optimized DBR location where the dark current can be far reduced as low as 7 nA at 1550 nm operation wavelength [69]. A limitation of Ge-based photodetector is both their incompatibility with an unmodified CMOS process flow and the requirement for a buffer layer that causes problems in both thermal budget and planarity [70].

Another method is defect mediated state photodetector. Defect is introduced into the photodetector to enhance the photon absorption. Defect can be introduced through various method. One of the method is by hyper doping implantation of chalcogens (S, Se, Te) to increase doping concentration of the photodiode [71], [72]. Another way to introduce defect is by implantation of ions [73], [74]. However, this method introduces shallow impurity levels within the Si band gap. Therefore, to overcome this matter, Si^+ ion-implantation is proposed. This method allows the device to all-Si without any integration of other impurities material [75]–[77]. However, similarly, with the Ge integration, ion-implantation method also requires complexity of fabrication. In addition, the presence of defect during the fabrication process will caused an increasement in leak current value. On the other hand, two-photon absorption (TPA) has been reported to achieve all-Si photoreceiver [78], [79] and reported to achieve a minimum leak current ($\sim \text{pA}$). TPA is a nonlinear optical process where in semiconductor, an electron can be moved into an excited state by the simultaneous absorption of two photons of identical wavelength. TPA allows carriers to be absorbed and allow the generation of photocurrents.

Nowadays, performance of photoreceiver is not only based on operating speed, responsivity and signal-to-noise-ratio, but most importantly based on foot-print, cost of fabrication and ease integration. This is because current silicon optical interconnect is now towards the integration of chip-to-chip or on chip level. Therefore, higher degree level of integration is required. As shown in Fig. 1.14, although integration with other material of photodetectors shows much higher of operating speed, however, all-Si photodetector shows higher degree of integration.

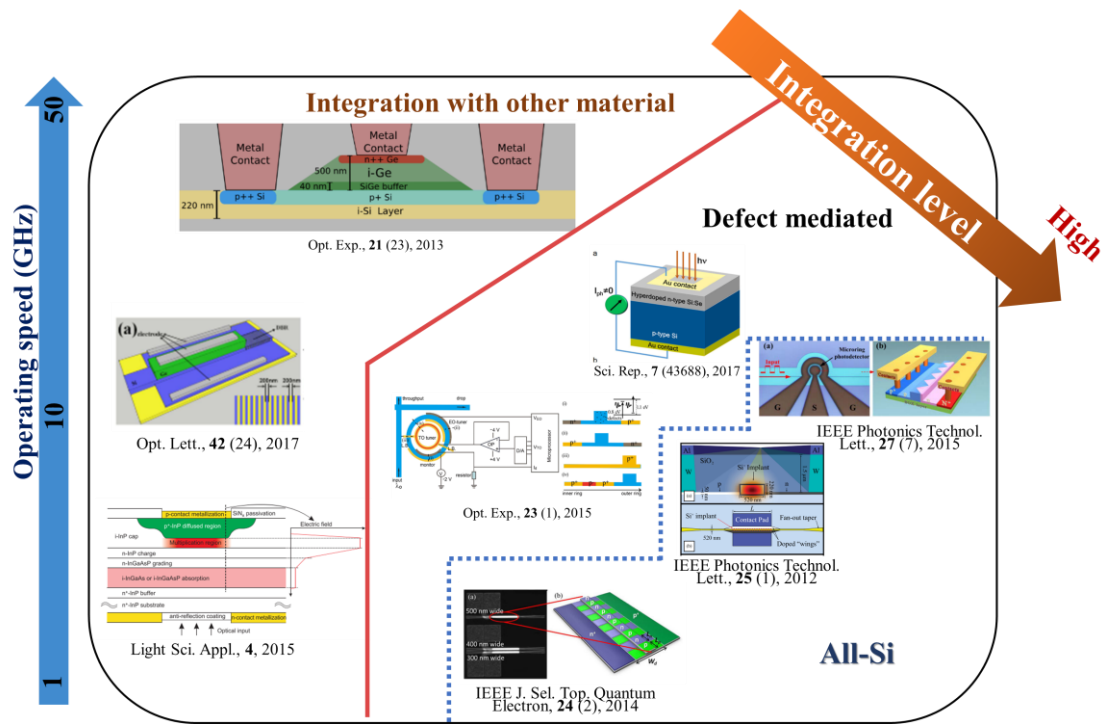


Fig. 1.14 Comparison of photodetector performance between integration with other material and defect mediated.

1.3.3 Optical transmission link

Transmission link system transmits data signal from transmitter to receiver. The system link requires transmitter and receiver to complete the whole signal transmission. The beginning of transceiver introduction was early 1920s where it has been implemented in radio to transmit the electrical wave signal. Then in 1970s, mobile phone has become a complete unit of signal transmission link system. Later, with the increasement of data rates for all interconnects, copper wire in electrical signal has come to its limitations. Researchers proposed that optical data transmission will become the best candidates to overcome this matter due to the ability to carry signal on a single fiber from a few gigabits per second to over one terabit per second.



Fig. 1.15 Intel silicon photonics optical transmitter. [Reprinted with permission from Intel brochure. [<https://www.intel.com/content/www/us/en/architecture-and-technology/silicon-photonics/optical-transceiver-100g-psm4-qsf28-brief.html>]]

First fully integrated optical transmission system in silicon has been demonstrated by Luxtera Inc. [80] and achieved 20 Gbs^{-1} optical transmission using combination of LiNbO_3 modulator and InGaAsP detector. However, besides large die dimension of the device, power consumption of the system is as large as 2.5 W . Next, the silicon optical transmission system has been commercialized by Intel Silicon Photonics groups. Research regarding Si optical transmission system has been further studied whose low power operation monolithically transceiver has been demonstrated using high-speed MZI modulators [81] by the same group. A year later, compact and even low power consumption monolithic link has been reported [82], [83]. Those devices are the combination of ring-resonator based modulator as transmitter and Ge detectors as receivers.

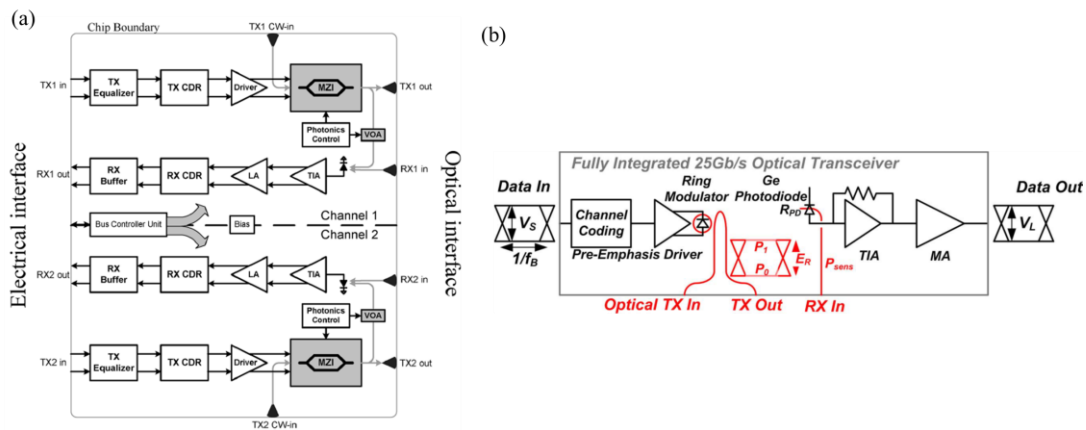


Fig. 1.16 Block diagram of optical transmission device. (a) Dual-channel 10 Gbs^{-1} transceiver MZI. [Reprinted with permission B. Analui, *et al.*, IEEE J. Solid-State Circuits **41** (12), 2006] (b) Fully integrated 25 Gbs^{-1} Si photonic interconnect. [Reprinted with permission J. F. Buckwalter, *et al.*, IEEE J. Solid-State Circuits **47** (6), 2012]

Due to plasma dispersion effect, silicon has become an excellent material for modulation. Due to that, researchers are utilizing Si-based optical modulator in optical transmission link system [82]–[84]. However, due to the transparency of Si at telecom wavelength, integration with other material of photoreceiver has been utilize in optical transmission link system. Most of the utilizing epitaxially grown Ge or heterogeneously bonded III-V photodetectors at the receiver. Although the combination of Si-based modulator and hybrid photodetector shows a significantly high operating bandwidth, it will become inadequately efficient in future optical transmission link device. This is because, those combination has a lower degree of integration which makes the device becomes difficult to integrate with other CMOS process device on a single chip. In addition, due to the high epitaxially required grown or integration of material for the photodetector, makes the fabrication cost becomes expensive. Therefore, a higher-level degree of integration and cost-effective has become attention among researchers.

Recently, Fujikura Ltd. has reported all-Si scheme optical transmission link was successfully achieved. They have proven that the scheme able to modulate and detect signal up until $10/20 \text{ km}$ transmission link [85], thus, shows that it is possible to realize silicon photonics chip-to-chip transmission link. However, future demands in information technology and internet

requires silicon photonic interconnect devices to be integrated on single chip. Although, monolithic (that is on a single chip) integration of photonic devices in close proximity to electronic circuits is crucial, recent studies has shown that it is possible to integrate photonics with silicon nanoelectronics systems on a chip [86]. The systems on chip device has successfully integrated wavelength division multiplexing (WDM) transmission link system monolithically. The study has shown that the next generation of photonic platform for computing, communications, imaging and sensing requires systems on chip.

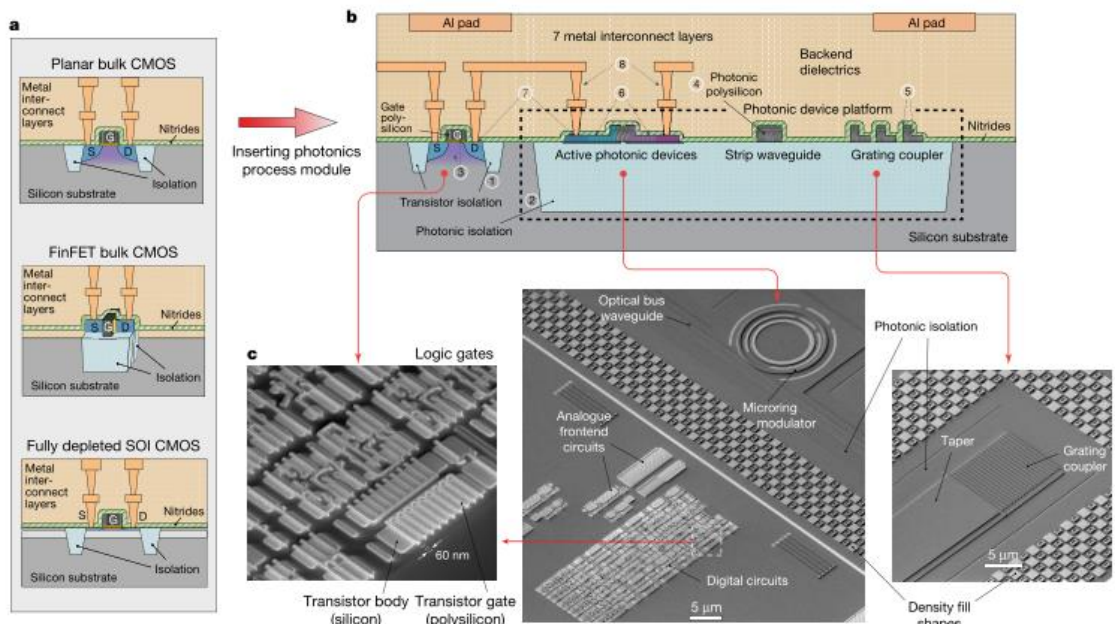


Fig. 1.17 Photonic integration with nanoscale transistors. [Reprinted with permission A. Atabaki, *et al.*, *Nat.*, **556** (7701), 2018]

1.4 Purpose of Study

1.4.1 Motivation

As describe in earlier section, optical signal processing has become an attraction. Due to the high refractive index and low absorption loss of silicon, it is expected to be an outstanding candidate for replacing electrical wire. Although various silicon photonic devices have been developed, demand for a smaller footprint, lower power consumption and higher functionality remains. In addition, current optical communication is towards shorter range in which chip-to-chip also required easy monolithically integration on chip and cost effectively. This are difficult to be achieved with existing Si photonic devices.

Two-dimensional PhC structure allows strong light confinement that leads to high- Q factor. Moreover, with the small mode volume, makes the demonstration of all-optical switching possible. Although those demonstrated devices claimed to be compatible with CMOS process, several challenges need to be overcome to integrate those devices with another Si photonic devices due to the different structure. As a result, the integration becomes more difficult.

On the other hand, PhC nanocavity requires high precision of fabrication to achieve high- Q factor. Therefore, most of the PhC nanocavity devices are fabricated by electro-beam lithography. The electro-beam lithography is an accurate fabrication process however, in term of time, the fabrication method is a time-consuming process. Hence, a stepper photolithography process, which is more commercial and widely used need to be employed. That is not all, due to the compatibility with CMOS process, this fabrication process will ease the integration of PhC device with other Si devices on the same chip.

Among various devices that has been demonstrated for optical devices, electro-optic (EO) and opto-electronic (OE) devices are the main components in order to link the electrical circuits with photonic circuits. Demonstration of EO operation is challenging because it requires low-power consumption and possible to transmit signal in fast speed. However, OE operation is more challenging because at telecom wavelength (1.55 μm), Si is transparent and photo carriers could not be generated. Therefore, complex fabrication method in which a hybrid-type photodetector such as integration of Germanium or Graphene and ion-implantation on Si has been introduced. However, it suffers for high dark current due to the presence of defect in the structure. This will lead to a disturbance of noise during data transmission.

In addition, based on Moore's Law, there are great demand to switch from electrical circuit to optical circuit. Currently, silicon photonic based-transceiver has been commercialized by several groups. However, this device will become insufficient in the future due to the dissatisfying of optical communication demand. Since in future, the optical chip circuit are expected to be compact in size, low fabrication cost and package simplicity to extreme, researchers are start to consider for all-silicon of OE and EO scheme.

1.4.2 Objective

Recently, due to the advancement of fabrication technology process, Si PhC nanocavity has achieved high- Q factor ($\sim 10^5$) fabricated by deep-UV photolithography fabrication process [87]. The high- Q is succeeded with the presence of SiO_2 clad on the surface makes the width-modulated line defect cavity device much stable and robust. The mode volume of the device is $\sim 1.7 (\lambda/n)^3$. The device was fabricated with standard CMOS process line which allowed the silicon PhC to be integrated with other devices, such as spot-size converter (SSC), heaters and $p-i-n$ diode. This has constituted that Si PhC possible to realize integration on silicon chip and open for new possibilities for silicon photonics technology.

In this study, the application to explored high- Q photolithographically PhC nanocavity device as an optical interconnect device, namely electro-optic modulator and photoreceiver are studied. The target of the applications is towards on chip integration device with have smaller foot-print. The $p-i-n$ diode has been embedded to the device to allow carriers injection for light modulation. Via the carrier plasma dispersion effect, the transmittance spectrum wavelength able to be modulated. Thanks to the high- Q factor, it has enabled the device to achieve large optical modulation even though the refractive index modulation is small. Thus, low power consumption is achievable. A sub-GHz modulation operation based on the carrier plasma dispersion reveals that the device has a large bandwidth modulation ability [88].

Next, the opto-electronic demonstration is demonstrated by the device. Although, it is challenging because Si is not the best candidate in term of light detection at telecom wavelength, with the high- Q factor and low leak current, it is proven that photodetection is able to be achieved.

Thus, a low-power photodetection become possible due to the all-Si device and with the help of two-photon absorption (TPA). Though similar demonstration has been done before, but with the air-clad surface, a complex fabrication process is needed specially to take care of the contact pads during the air-bridging process. Therefore, in this study, the PhC nanocavity device was cladded with silica which makes the device more stable and robust, so, the photo-detection operation demonstration becomes uncomplicated and most importantly is full CMOS compatibility [89].

Then, the combination of EO operation and OE operation as an optical transmission link is demonstrated. Since the device was made by all-Si, all-Si scheme transmission link is achievable with help of TPA effect. In addition, with the randomness structure as a detector, proved that the randomness in PhC structure possible for a practical device. The demonstration is done by detuning the resonance wavelength through temperature time dependence to match the resonance of transmitter and receiver. A sub-GHz operation was achieved. This demonstration has paved an alternative way for optical transmission as it offers small dimension and higher degree of integration with CMOS devices.

In this thesis, the contents are arranged as follows where the theory of PhC and design of the device structure will be described in Chapter 2. Next, the fabrication process of the device will be explained in Chapter 3. Then, the functionalities of the device in which as electro-optic modulator will be described in Chapter 4. The demonstration of the photoreceiver is then will be presented in Chapter 5. In Chapter 6, the demonstration of all-silicon transmission link of optical transceiver will be explained. Finally, in Chapter 7, the thesis will be summarized.

Chapter 2

Theory of Photonic Crystal

This chapter will explain the fundamental theory of PhC. The basic of PBG structure is explained which then led to the formation of cavity in the PhC. Then, the method of analysis contains of plane-wave and FDTD method which are commonly used for numerical calculation will be introduce. Later, the PhC design structure that is used in this study will be describe.

2.1 Introduction

The study of photonic crystal (PhC) had begun since 1887 by Lord Rayleigh issue of Philosophical Magazine[7]. However, no one used the term of '*photonic crystal*'. Until in 1987, American physicist who known as Eli Yablonovitch announced the name of '*photonic crystal*' and successfully discover creation of a photonic bandgap (PBG) [4]. Then, Sajeev John has published another milestone paper on the same field by discovering photon localization in high dielectric contrast disorder superlattice microstructure which is beneficial for mechanism of non-linear application devices[8]. In this chapter, theory of PBG and cavity formation method of PhC is explained. The common method for a numerical calculation also will be described.

2.2 Photonic band structure

The existence of photonic band gap were reported in early 1990s through the solution of Maxwell's equation [90], [91]. It has been a basis concept in understanding PhC. The utilization of PBG has been expanded by researchers. The introduction of defect in PBG structure can produce a cavity to PhC. In this section, Maxwell's equation and the formation of cavity will be described.

2.2.1 Maxwell's equation

The propagation of light in PhC governed by Maxwell's equations as follows,

$$\nabla \cdot \mathbf{B} = 0 \quad (2.1)$$

$$\nabla \times \mathbf{E} + \frac{\partial \mathbf{B}}{\partial t} = 0 \quad (2.2)$$

$$\nabla \cdot \mathbf{D} = \rho \quad (2.3)$$

$$\nabla \times \mathbf{H} - \frac{\partial \mathbf{D}}{\partial t} = \mathbf{J} \quad (2.4)$$

where \mathbf{E} , \mathbf{H} , \mathbf{D} , \mathbf{B} , ρ and \mathbf{J} are the electric field, magnetic field, electric flux density, magnetic flux density, free charge and current density, respectively. Eq. 2.1 expresses the fact that the magnetic lines of flux form a system of closed loops. Eq. 2.2 is differential form of Faraday's law of induction. Eq. 2.3 is differential form of Gauss's law and Eq. 2.4 is a generalization of Ampere's circuital law (also referred as the Biot-Savart) by the addition of $\frac{\partial \mathbf{D}}{\partial t}$, which is called the displacement current density.

\mathbf{D} and \mathbf{B} can be rewrite as follows,

$$\mathbf{D}(\mathbf{r}) = \epsilon_0 \epsilon(\mathbf{r}) \mathbf{E}(\mathbf{r}) \quad (2.5)$$

$$\mathbf{B}(\mathbf{r}) = \mu_0 \mu(\mathbf{r}) \mathbf{H}(\mathbf{r}) \quad (2.6)$$

where ϵ_0 and μ_0 denote the electric permittivity and magnetic permeability of vacuum respectively. However, for most dielectric material the relative magnetic permeability $\mu(\mathbf{r})$ is very close to unity, the Eq. 2.6 can be written as $\mathbf{B} = \mu_0 \mathbf{H}$.

The Maxwell's Eq. 2.1 to Eq. 2.4 become,

$$\nabla \cdot \mathbf{H}(\mathbf{r}, t) = 0 \quad (2.7)$$

$$\nabla \times \mathbf{E}(\mathbf{r}, t) + \mu_0 \frac{\partial \mathbf{H}(\mathbf{r}, t)}{\partial t} = 0 \quad (2.8)$$

$$\nabla \cdot [\varepsilon(\mathbf{r})\mathbf{E}(\mathbf{r}, t)] = 0 \quad (2.9)$$

$$\nabla \times \mathbf{H}(\mathbf{r}, t) - \varepsilon_0 \varepsilon(\mathbf{r}) \frac{\partial \mathbf{E}(\mathbf{r}, t)}{\partial t} = 0 \quad (2.10)$$

\mathbf{E} and \mathbf{H} are harmonic (oscillation) modes which can be express as,

$$\mathbf{H}(\mathbf{r}, t) = \mathbf{H}(\mathbf{r}) e^{-j\omega t} \quad (2.11)$$

$$\mathbf{E}(\mathbf{r}, t) = \mathbf{E}(\mathbf{r}) e^{-j\omega t} \quad (2.12)$$

Both Eq. 2.11 and Eq. 2.12 can be insert in the Eq. 2.7 and Eq. 2.9 which will describe the mode profile at the given frequency that have simple physical interpretation of there are no point sources of displacement and magnetic medium.

$$\nabla \cdot \mathbf{H}(\mathbf{r}) = 0 \quad (2.13)$$

$$\nabla \cdot [\varepsilon(\mathbf{r})\mathbf{E}(\mathbf{r})] = 0 \quad (2.14)$$

The field configurations are built up of electromagnetic waves that are transverse. Therefore, if a plane wave of $\mathbf{H}(\mathbf{r}) = \mathbf{a} \exp(j\mathbf{k} \cdot \mathbf{r})$, for some wave vector \mathbf{k} , Eq. 2.13 and Eq. 2.14 requires that $\mathbf{a} \cdot \mathbf{k} = 0$.

For Eq. 2.8 and Eq. 2.10, the two curl equations relate $\mathbf{E}(\mathbf{r})$ to $\mathbf{H}(\mathbf{r})$

$$\nabla \times \mathbf{E}(\mathbf{r}) - j\omega\mu_0\mathbf{H}(\mathbf{r}) = 0 \quad (2.15)$$

$$\nabla \times \mathbf{H}(\mathbf{r}) + j\omega\varepsilon_0\varepsilon(\mathbf{r})\mathbf{E}(\mathbf{r}) = 0 \quad (2.16)$$

From the above equations, can be divided by $\varepsilon(\mathbf{r})$ and then take the curl. The Eq. 2.15 can be used to eliminate $\mathbf{E}(\mathbf{r})$ and constants ε_0 and μ_0 can be combined to yield the vacuum speed of light, $c = \frac{1}{\sqrt{\varepsilon_0\mu_0}}$. Results is express as follow,

$$\nabla \times \left(\frac{1}{\varepsilon(\mathbf{r})} \nabla \times \mathbf{H}(\mathbf{r}) \right) = \left(\frac{\omega}{c} \right)^2 \mathbf{H}(\mathbf{r}) \quad (2.17)$$

From the Eq. 2.16, $\mathbf{E}(\mathbf{r})$ is obtained,

$$\mathbf{E}(\mathbf{r}) = \frac{j}{\omega \varepsilon_0 \varepsilon(\mathbf{r})} \nabla \times \mathbf{H}(\mathbf{r}) \quad (2.18)$$

and for value $\mathbf{H}(\mathbf{r})$,

$$\mathbf{H}(\mathbf{r}) = -\frac{j}{\omega \mu_0} \nabla \times \mathbf{E}(\mathbf{r}) \quad (2.19)$$

Next, the operator $\hat{\Theta}$ acting on $\mathbf{H}(\mathbf{r})$ is define,

$$\begin{aligned} \hat{\Theta} \mathbf{H}(\mathbf{r}) &\triangleq \nabla \times \left(\frac{1}{\varepsilon(\mathbf{r})} \nabla \times \mathbf{H}(\mathbf{r}) \right) \\ \hat{\Theta} \mathbf{H}(\mathbf{r}) &= \left(\frac{\omega}{c} \right)^2 \mathbf{H}(\mathbf{r}) \end{aligned} \quad (2.20)$$

In periodic structure, $\mathbf{H}(\mathbf{r})$ is assume as a periodic function. Based on Bloch-Floquet theorem, the periodic function has Bloch wavevector \mathbf{k} which can be describe as following equation,

$$\mathbf{H}(\mathbf{r}) = \mathbf{H}_{\mathbf{k}}(\mathbf{r}) = e^{j\mathbf{k}\cdot\mathbf{r}} \cdot \mathbf{H}_{n,\mathbf{k}}(\mathbf{r}) \quad (2.21)$$

$$\mathbf{H}_{n,\mathbf{k}}(\mathbf{r}) = \mathbf{H}_{n,\mathbf{k}}(\mathbf{r} + \mathbf{a}) \quad (2.22)$$

\mathbf{a} is a lattice constant value of the structure and n corresponds to the label number of primitive cells that is a part of the periodic structure. By inserting both Eq. 2.21 and Eq. 2.22 into Eq. 2.17, Eq. 2.23 can be obtained.

$$(\nabla + j\mathbf{k}) \times \frac{1}{\varepsilon(\mathbf{r})} (\nabla + j\mathbf{k}) \times \mathbf{H}_{n,\mathbf{k}}(\mathbf{r}) = \left(\frac{\omega_n(\mathbf{k})}{c} \right)^2 \mathbf{H}_{n,\mathbf{k}}(\mathbf{r}) \quad (2.23)$$

In Schrödinger equation, $\left(\frac{\omega_n(\mathbf{k})}{c} \right)^2$ is eigenvalue. $\omega_n(\mathbf{k})$ are in function ok \mathbf{k} where it expresses the system dispersion. $\mathbf{H}(\mathbf{r})$ in Eq. 2.22 described a Bloch function and satisfy condition below, where wavevector \mathbf{k}' if $\mathbf{k}' = \mathbf{k} + \frac{2\pi}{a}$

$$\mathbf{H}_{\mathbf{k}}(\mathbf{r}) = e^{j\left(\mathbf{k}' - \frac{2\pi}{a}\right) \cdot \mathbf{r}} \cdot \mathbf{H}_{n,\mathbf{k}}(\mathbf{r}) = e^{j\mathbf{k}' \cdot \mathbf{r}} \cdot \mathbf{H}_{n,\mathbf{k}}(\mathbf{r}) e^{-j\frac{2\pi}{a} \cdot \mathbf{r}} \quad (2.24)$$

Since,

$$\mathbf{H}_{n,\mathbf{k}}(\mathbf{r}) e^{-j\frac{2\pi}{a} \cdot \mathbf{r}} = \mathbf{H}_{n,\mathbf{k}}(\mathbf{r} + a) e^{-j\frac{2\pi}{a}(\mathbf{r}+a)}$$

Following equations can be obtained.

$$\mathbf{H}_{n,\mathbf{k}'}(\mathbf{r}) = \mathbf{H}_{n,\mathbf{k}}(\mathbf{r}) e^{-j\frac{2\pi}{a} \cdot \mathbf{r}} \quad (2.25)$$

$$\mathbf{H}_{\mathbf{k}}(\mathbf{r}) = e^{j\mathbf{k}' \cdot \mathbf{r}} \cdot \mathbf{H}_{n,\mathbf{k}'}(\mathbf{r}) = \mathbf{H}_{\mathbf{k}'}(\mathbf{r}) \quad (2.26)$$

Based on the Eq. 2.25, it is proven that $\mathbf{H}_{\mathbf{k}}(\mathbf{r})$ is $\frac{2\pi}{a}$ periodical function. Thus, the eigenvalue $\omega_n(\mathbf{k})$ also have same periodicity. So, in order to know the dispersion relation, it is sufficient to know between the range of $-\pi/a \leq \mathbf{k} \leq \pi/a$ which is known as a first Brillouin zone. In most cases where time-reversal symmetry is satisfied, only half of the range is considered which is $0 \leq \mathbf{k} \leq \pi/a$.

On the other hand, when a system is a one-dimensional structure, it has a uniform dielectric of $\varepsilon(\mathbf{r}) = 1$, the dispersion diagram of the structure is shown as Fig. 2.1 (a) where the eigenvalue of Eq. 2.23 is $\omega(\mathbf{k}) = c\mathbf{k}$.

However, if the system to be periodical perturbation of Δ in dielectric constant, $\varepsilon(\mathbf{r}) = 1 + \Delta \cdot \cos\left(\frac{2\pi\mathbf{r}}{a}\right)$ is assumed and two eigenvalues as follows at $\mathbf{k} = \pi/a$ proportional to $\cos\left(\frac{\pi\mathbf{r}}{a}\right)$ or $\sin\left(\frac{\pi\mathbf{r}}{a}\right)$ are obtained.

$$\omega_{+,k=\frac{\pi}{a}} \propto |\mathbf{H}_+|^2 \propto 4\cos^2 \frac{\pi\mathbf{r}}{a} \quad (2.27)$$

$$\omega_{-,k=\frac{\pi}{a}} \propto |\mathbf{H}_-|^2 \propto 4\sin^2 \frac{\pi\mathbf{r}}{a} \quad (2.28)$$

Eq. 2.27 and Eq. 2.28 is the origin of PBG as shows in Fig. 2.1 (b). PBG works as a forbidden band for photons in the PhC structure where light within the wavelength of PBG could not enter the medium.

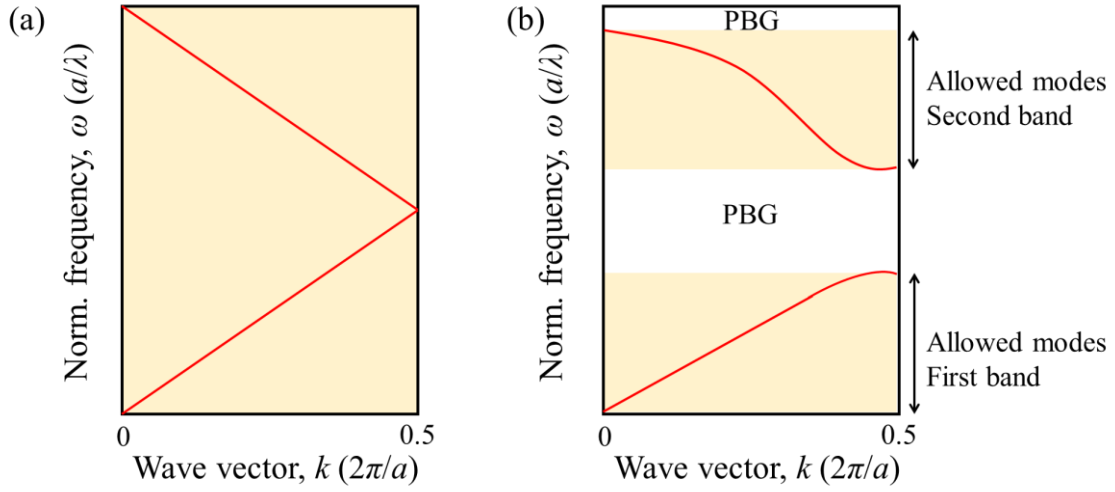


Fig. 2.1 Dispersion relation, ω vs. k for waves in one-dimensional PhC structure. (a) Dispersion diagram for a uniform dielectric material where $\epsilon(\mathbf{r}) = 1$. (b) Dispersion diagram for periodic dielectric structures where $\epsilon(\mathbf{r}) = 1 + \Delta \cdot \cos\left(\frac{2\pi\mathbf{r}}{a}\right)$.

This can be expanded into two- or three-dimensional periodic structure. But, in principle, there is no full PBG in two-dimensional PhC structure. In the case of three-dimensional periodic structure, there would be photonic bandgaps along x , y and z directions, and for different polarizations of the dielectric field. If the refractive index contrast and the periodicity in the three-dimensional structure are such that these photonic bandgaps overlap in all directions and for all polarizations of light, a full photonic bandgap occurs. As shown in Fig. 2.2 (a), the overlap frequency range $\Delta\omega$ becomes full PBG in all directions and for all polarizations of light which means no light can propagate through the structure. However, only certain three-dimensional structures allow full PBG to develop. One of the allowed structures is 'wood pile' periodic structure as shown in Fig. 2.2 (b). In 'wood pile' structure, the rods are parallel in each layer and the layers are perpendicular to each other.

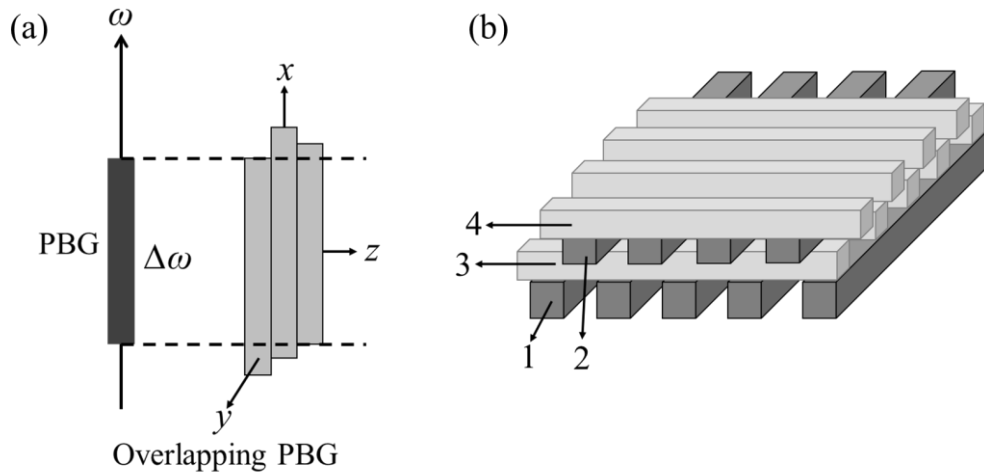


Fig. 2.2 (a) Full PBG in three-dimensional PhC structure. The PBG along x , y and z are overlapping for all polarizations of field. (b) The 'wood pile' unit cell of PhC. The 1-4 labelled referring to the 4 layers that is parallel to each other.

2.2.2 Cavity formation

Point and line defects that occur in normal crystal, also occur in PhC structure. Fig. 2.3 illustrated the example of defects. Defects are introduced to PhC to enhance certain optical properties. Definition of defects is a discontinuity in the periodic structure. There are two kinds of defects which is point defect and line defect as shown in Figs. 2.3 (a) and (b), respectively. Point defect or so-called optical cavity, can be created by removing or altering a unit cell in the periodicity. This will lead to the trapping of light radiation within the cavity as illustrated in Fig. 2.3 (d).

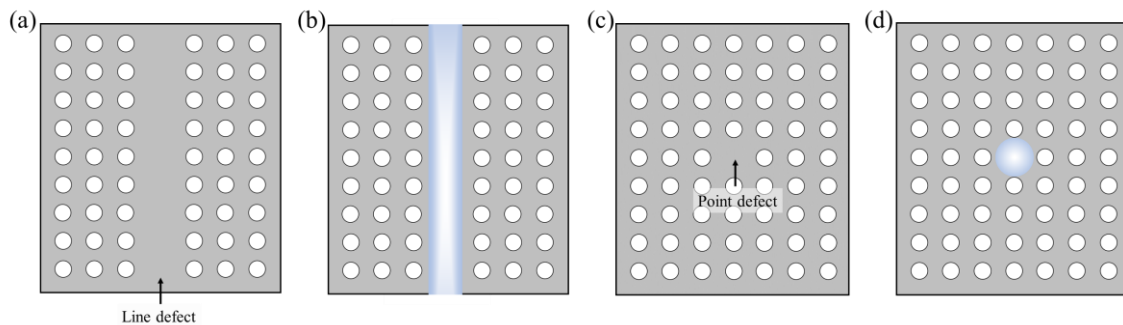


Fig. 2.3 Illustration of defects in PhC structure. (a) Line defect is introduced in PhC structure. (b) An ultrasmall waveguide formed and permits light propagation only along the line defect. (c) Point defect that acts as an optical cavity to trap the light. (d) Light that has been trap (confined) inside the cavity.

Line defect

Line defects are formed when a certain row of unit cell is removed. The light is prevented from dispersing into the crystal with the presence of PBG. The guided propagating light in the PhC structure is called waveguide as shown in Fig. 2.3 (b).

The dispersion diagram of the line defect is shown in the Fig. 2.4 and Fig. 2.5. The grey area represents the light cone where light is dissipated out of PhC slab due to the dissatisfied of total internal reflection. The orange area represents PhC modes Lattice constant, a and hole diameter is 420 nm and 253 nm, respectively. Line defect is introduced in the structure which W0.98 (0.98% of the original width). The inset shows the corresponding structure where the black area represents silicon material ($n = 3.47$) while the white area for Fig. 2.4 represents air ($n = 1.00$) and Fig. 2.5 represents silica ($n = 1.44$). Fig. 2.4 (a) and Fig. 2.5 (a) shows a perfect periodic PhC structure while Fig. 2.4 (b) and Fig. 2.5 (b) a line defect is introduced. It shows clearly, that two modes appear in the PBG area when line defect is introduced which represent the waveguide modes.

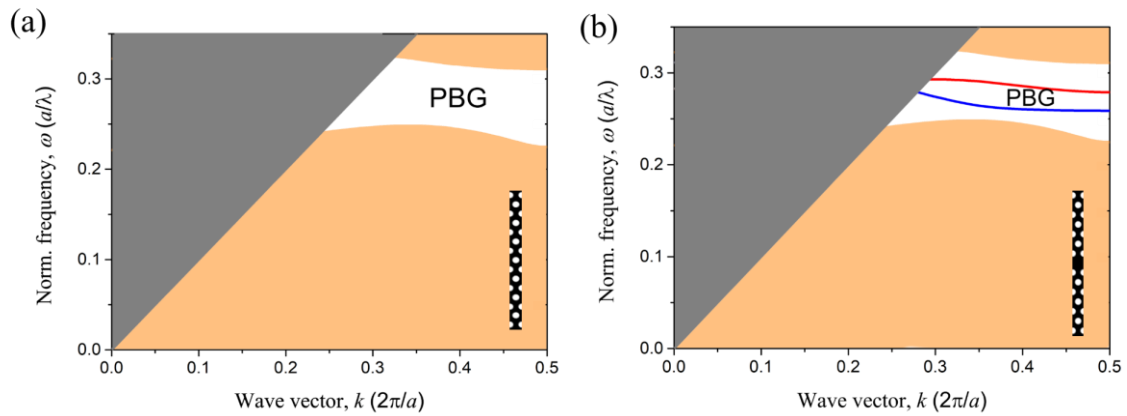


Fig. 2.4 Dispersion diagram of 2D PhC structure. (a) PhC structure without defect. (b) PhC structure with defect which is W0.98. The inset in (a) and (b) shows the corresponding structure. The blue line shows the even symmetry modes and the red line shows the odd symmetry modes. Insets shows the corresponding structure which represents silicon as the black area with refractive index, n of 3.47 and air as the white area with refractive index, n of 1.00.

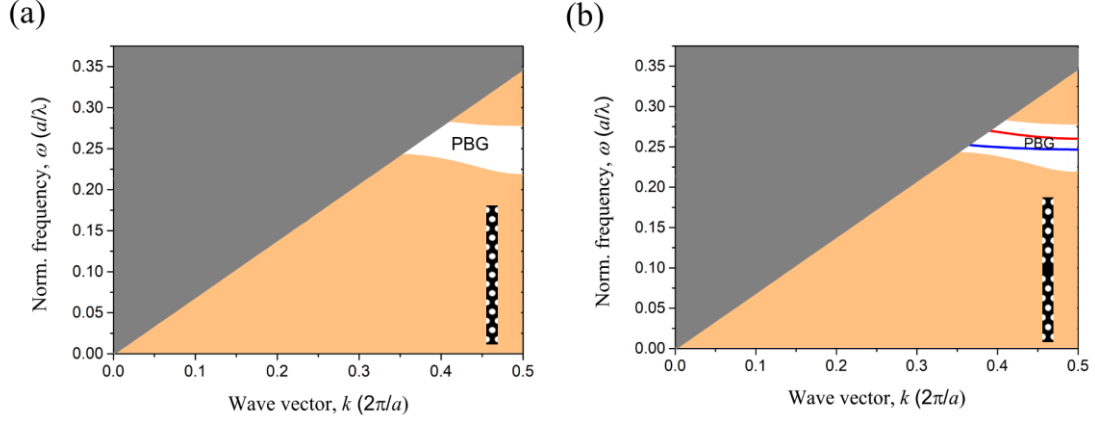


Fig. 2.5 Similar as Fig. 2.4. Insets shows the corresponding structure which represents silicon as the black area with refractive index, n of 3.47 and silica as the white area with refractive index, n of 1.44.

Due to the difference of refractive index between air and silica, the frequency range of PBG is narrower in Fig. 2.5 since the ambience of silicon is silica which is known as silica-clad. Therefore, light is propagating in narrower frequency range in silica-clad PhC waveguides.

Point defect

In two-dimensional PhC slab waveguide, distributed Bragg reflection (DBR) of the surrounding PhC lattice influenced the in-plane defect mode confinement. With the condition that the wave vector of light at vertical is k_{\perp} and at parallel is k_{\parallel} to the PhC slab, wave vector of light k is

$$k^2 = k_{\parallel}^2 + k_{\perp}^2 = \left(\frac{n_{cav} \omega}{c} \right)^2 \quad (2.29)$$

In total internal reflection, the light wave vector, k will satisfy the Snell's law as follows,

$$\left| \frac{k_{\parallel}}{k} \right| > \frac{n_{amb}}{n_{cav}} \quad (2.30)$$

The dissipation of light in defect from the slab can be calculated from the [Eq. 2.29](#) and [Eq. 2.30](#).

The vertical confinement works as standard waveguiding by total internal reflection. If the magnitude of the in-plane momentum component, k_{\perp} , is insufficient to support guiding, vertical radiation loss will occur. Therefore, in order to achieve high- Q factor, the vertical radiation loss have to be reduced. For an air clad PhC waveguide, due to the refractive index, n is 1, therefore $k_{\perp}^2 = (\omega/c)^2$, where ω is angular frequency and c is the speed of light. Modes that radiate vertically will have small in-plane momentum components lie within the light cone cladding.

Fig. 2.6 illustrates the light cone in two-dimensional structure. If the frequency of wavevector of light is ω_0 , light will not exist in the slab and dissipate to the surrounding.

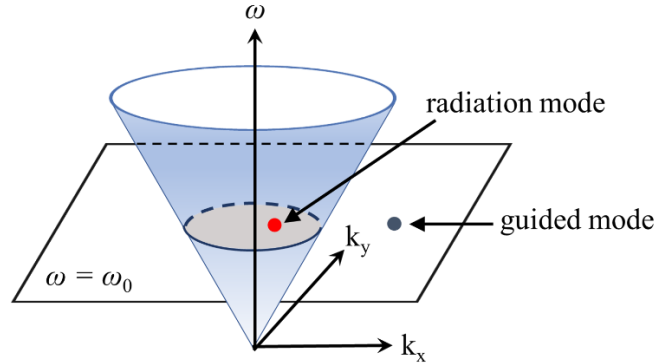


Fig. 2.6 Light cone in k_x , k_y and ω space where $k = \omega \cdot (n_{\text{amb}}/c)$. Blue cone represents to the light cone where in light will be dissipate from the slab in this area.

2.3 Fabry-Pérot Cavity

In order to understand the transmission spectrum of a nanocavity, Fabry-Pérot cavity is used as an example. It consists of two flat mirrors opposing each other as illustrated in Fig. 2.7 (a). When this mirror perfectly aligned to each other as parallel with free space between them, light wave reflection occurs between the two mirror M_1 and M_2 . The light reflections wave between the mirrors of M_1 and M_2 will lead to construct and destruct the interference within the cavity. During the constructive phenomenon, it is called resonance. The series of travelled reflected waves will produce a standing light wave in the cavity as in Fig. 2.7 (b). At the resonance phenomenon, Eq. 2.31 should be satisfied;

$$m\lambda_m = 2nL; m = 1, 2, 3, \dots \quad (2.31)$$

where m is an integer of mode number, λ_m is resonance wavelength, n is medium refractive index and L is the cavity length. Fig. 2.7 (c) illustrates the intensity of the allowed modes as a function of frequency. If the mirrors are perfectly aligned, light beam will be reflecting within the mirrors and there will be no loses from the cavity, thus, sharp line peaks occur at frequencies, ν_m . The frequencies at ν_m can be defined as Eq. 2.32.

$$\nu_m = \left(\frac{c}{2nL} \right) m \quad (2.32)$$

However, in some cases there is possibility that some light radiation will escape from the cavity caused by the imperfectly mirror reflecting, hence, the mode peaks will appear less sharp and finite.

Refer to Fig. 2.7 (a), light wave will be travelled as wave Y after wave X completing a round trip. In the imperfection of reflections cases, wave Y has different phase and magnitude compared to wave X. If the value of reflection coefficient of mirror M_1 and M_2 are same as

magnitude r , then one round trip of wave Y has phase different of $k(2L)$ and magnitude of r^2 with respect to wave X. Therefore, the interference of both waves can be expressed as;

$$X + Y = X + Xr^2 \exp(-j2kL) \quad (2.33)$$

The interference can occur in series and the sum field E_{cavity} can be evaluated as

$$E_{cavity} = \frac{X}{1 - r^2 \exp(-j2kL)} \quad (2.34)$$

Based on above equation, the intensity of the cavity can be calculated as

$$I_{cavity} = \frac{I_0}{(1 - R)^2 + 4R \sin^2(kL)} \quad (2.35)$$

where $R = r^2$ is reflectance. From the Eq. 2.35, the maximum of cavity intensity can be derived as;

$$I_{max} = \frac{I_0}{(1 - R)^2} \quad (2.36)$$

From Eq. 2.36, can be understood the maximum intensity occurs if the $\sin^2(kL)$ becomes zero. If the value of R is smaller, the broader the peaks will be due to the radiation loss from the cavity.

The quality factor, Q of the resonant cavity can be defined as;

$$Quality\ factor, Q = \frac{\nu_m}{\delta\nu_m} \quad (2.37)$$

where $\delta\nu_m$ is spectral width. The spectral width is defined as full width at half maximum (FWHM) of an individual mode intensity. It can be calculated by;

$$\delta\nu_m = \frac{\nu_f}{F}; F = \frac{\pi R^{1/2}}{1 - R} \quad (2.38)$$

where F is the finesse of the cavity. Less loss of the cavity will increase the finesse of the cavity that will be sharpen the mode peaks.

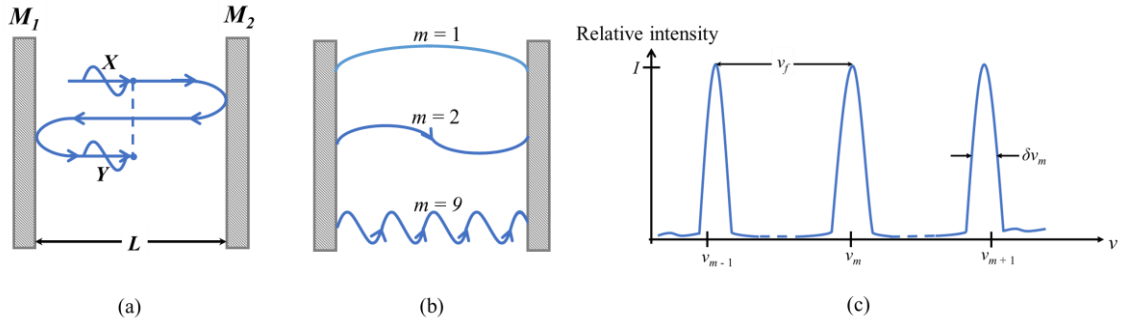


Fig. 2.7 Illustration of Fabry-Pérot cavity. (a) Interference of reflected waves on two flat mirrors. (b) Standing EM waves and modes at certain wavelengths that are allowed to be in the cavity. (c) Intensity vs. frequency for various modes.

2.4 Method of analysis

2.4.1 Plane-wave (PW) method

The plane-wave (PW) method is the reference method for the calculation of band gaps in PhC. Calculation with PW method usually done with a hundred to a few hundred PWs, depending on the strength of the dielectric constant. The band structure is obtained by diagonalizing matrices on the order of two hundred to a few hundred in size. The method is very versatile and can be applied to handle all forms of dielectric modulations. In this study, the method is used with a free software package of MPB which has been developed by Joannopoulos's group.

Let's assume that the photonic band structure for electromagnetic waves propagating in a plane perpendicular to the dielectric rods is calculated. The position-independent dielectric constant together with the PW method is used. Two electromagnetic waves are considered which is \mathbf{H} polarization and \mathbf{E} polarization.

\mathbf{H} polarization

Based on the Eq. 2.11 and Eq. 2.12, can be rewrite as:

$$\mathbf{H}(\mathbf{r}, t) = (0, 0, \mathbf{H}_z(\mathbf{r}, \omega)) \exp(-j\omega t)$$

$$\mathbf{E}(\mathbf{r}, t) = (\mathbf{E}_x(\mathbf{r}, \omega), \mathbf{E}_y(\mathbf{r}, \omega), 0) \exp(-j\omega t) \quad (2.39)$$

The Maxwell's curl equation for the three non-zero field components are:

$$\frac{\partial \mathbf{E}_y}{\partial x} - \frac{\partial \mathbf{E}_x}{\partial y} = i\omega\mu_0 \mathbf{H}_z$$

$$\frac{\partial \mathbf{H}_z}{\partial x} = i\omega \varepsilon_0(\mathbf{r}) \mathbf{E}_y$$

$$\frac{\partial \mathbf{H}_z}{\partial y} = i\omega \varepsilon_0 \varepsilon_r(\mathbf{r}) \mathbf{E}_z \quad (2.40)$$

when eliminate \mathbf{E}_x and \mathbf{E}_y from these equations. The Eq. 2.40 that satisfied by \mathbf{H}_z can be obtained, which can be written as the following form,

$$\frac{\partial}{\partial x} \left(\frac{1}{\varepsilon_r(\mathbf{r})} \frac{\partial \mathbf{H}_z}{\partial x} \right) + \frac{\partial}{\partial y} \left(\frac{1}{\varepsilon_r(\mathbf{r})} \frac{\partial \mathbf{H}_z}{\partial y} \right) + \frac{\omega^2}{c^2} \mathbf{H}_z = 0 \quad (2.41)$$

$\varepsilon_r^{-1}(\mathbf{r})$ and $\mathbf{H}_z(\mathbf{r}|\omega)$ is expand to solve this equation according to

$$\frac{1}{\varepsilon_r(\mathbf{r})} = \sum_{\mathbf{G}'} \hat{k}(\mathbf{G}') \exp(i\mathbf{G}' \cdot \mathbf{r})$$

$$\mathbf{H}_z(\mathbf{r}, \omega) = \sum_{\mathbf{G}} A(\mathbf{K}, \mathbf{G}) \exp[i(\mathbf{K} + \mathbf{G}) \cdot \mathbf{r}] \quad (2.42)$$

where \mathbf{K} is two-dimensional wave vector of the wave in the Brillouin zone of the lattice and \mathbf{G} is a vector of the reciprocal lattice.

Substituting Eq. 2.42 in Eq. 2.43,

$$\begin{aligned} & \frac{\partial}{\partial x} \left(\sum_{\mathbf{G}'} \hat{k}(\mathbf{G}') \exp(i\mathbf{G}' \cdot \mathbf{r}) \frac{\partial \sum_{\mathbf{G}} A(\mathbf{K}, \mathbf{G}) \exp[i(\mathbf{K} + \mathbf{G}) \cdot \mathbf{r}]}{\partial x} \right) \\ & + \frac{\partial}{\partial y} \left(\sum_{\mathbf{G}'} \hat{k}(\mathbf{G}') \exp(i\mathbf{G}' \cdot \mathbf{r}) \frac{\partial \sum_{\mathbf{G}} A(\mathbf{K}, \mathbf{G}) \exp[i(\mathbf{K} + \mathbf{G}) \cdot \mathbf{r}]}{\partial y} \right) \\ & + \frac{\omega^2}{c^2} \sum_{\mathbf{G}} A(\mathbf{K}, \mathbf{G}) \exp[i(\mathbf{K} + \mathbf{G}) \cdot \mathbf{r}] = 0 \end{aligned}$$

$$\begin{aligned} & \frac{\partial}{\partial x} \left(\sum_{\mathbf{G}'} \hat{k}(\mathbf{G}') \exp(i\mathbf{G}' \cdot \mathbf{r}) \sum_{\mathbf{G}} i(kx + Gx) A(\mathbf{K}, \mathbf{G}) \exp[i(\mathbf{K} + \mathbf{G}) \cdot \mathbf{r}] \right) \\ & + \frac{\partial}{\partial x} \left(\sum_{\mathbf{G}'} \hat{k}(\mathbf{G}') \exp(i\mathbf{G}' \cdot \mathbf{r}) \sum_{\mathbf{G}} i(ky + Gy) A(\mathbf{K}, \mathbf{G}) \exp[i(\mathbf{K} + \mathbf{G}) \cdot \mathbf{r}] \right) \\ & + \frac{\omega^2}{c^2} \sum_{\mathbf{G}} A(\mathbf{K}, \mathbf{G}) \exp[i(\mathbf{K} + \mathbf{G}) \cdot \mathbf{r}] = 0 \end{aligned}$$

$$\begin{aligned}
 & \frac{\partial}{\partial x} \left(\sum_{\mathbf{G}, \mathbf{G}'} \hat{k}(\mathbf{G}') i(kx + Gx) A(\mathbf{K}, \mathbf{G}) \exp[i(\mathbf{K} + \mathbf{G} + \mathbf{G}') \cdot \mathbf{r}] \right) \\
 & + \frac{\partial}{\partial y} \left(\sum_{\mathbf{G}, \mathbf{G}'} \hat{k}(\mathbf{G}') i(ky + Gy) A(\mathbf{K}, \mathbf{G}) \exp[i(\mathbf{K} + \mathbf{G} + \mathbf{G}') \cdot \mathbf{r}] \right) \\
 & + \frac{\omega^2}{c^2} \sum_{\mathbf{G}} A(\mathbf{K}, \mathbf{G}) \exp[i(\mathbf{K} + \mathbf{G}) \cdot \mathbf{r}] = 0 \\
 & \left(\sum_{\mathbf{G}, \mathbf{G}'} \hat{k}(\mathbf{G}') (kx + Gx)(kx + Gx + G'x) A(\mathbf{K}, \mathbf{G}) \exp[i(\mathbf{K} + \mathbf{G} + \mathbf{G}') \cdot \mathbf{r}] \right) \\
 & + \left(\sum_{\mathbf{G}, \mathbf{G}'} \hat{k}(\mathbf{G}') (ky + Gy)(ky + Gy + G'y) A(\mathbf{K}, \mathbf{G}) \exp[i(\mathbf{K} + \mathbf{G} + \mathbf{G}') \cdot \mathbf{r}] \right) \\
 & + \frac{\omega^2}{c^2} \sum_{\mathbf{G}} A(\mathbf{K}, \mathbf{G}) \exp[i(\mathbf{K} + \mathbf{G}) \cdot \mathbf{r}] = 0 \\
 & \left(\sum_{\mathbf{G}, \mathbf{G}'} \hat{k}(\mathbf{G}') \{ (kx + Gx)(kx + Gx + G'x) \right. \\
 & \quad \left. + (ky + Gy)(ky + Gy + G'y) \} A(\mathbf{K}, \mathbf{G}) \exp[i(\mathbf{K} + \mathbf{G} + \mathbf{G}') \cdot \mathbf{r}] \right) \\
 & + \frac{\omega^2}{c^2} \sum_{\mathbf{G}} A(\mathbf{K}, \mathbf{G}) \exp[i(\mathbf{K} + \mathbf{G}) \cdot \mathbf{r}] = 0
 \end{aligned} \tag{2.43}$$

The above Eq. 2.43 can be simplified as follows,

$$\begin{aligned}
 & (Kx + Gx)(Kx + Gx + G'x) + (Ky + Gy)(Ky + Gy + G'y) = (KxKx + 2KxGx + \\
 & KxG'x + GxGx + GxG'x) + (KyKy + 2KyGy + KyG'y + GyGy + GyG'y) = \mathbf{K} \cdot \mathbf{K} + \\
 & \mathbf{2K} \cdot \mathbf{G} + \mathbf{K} \cdot \mathbf{G}' + \mathbf{G} \cdot \mathbf{G} + \mathbf{G} \cdot \mathbf{G}' = \mathbf{K} \cdot (\mathbf{K} + \mathbf{G}) + \mathbf{G}' \cdot (\mathbf{K} + \mathbf{G}) + \mathbf{G} \cdot (\mathbf{K} + \mathbf{G}) \\
 & = (\mathbf{K} + \mathbf{G}' + \mathbf{G}) \cdot (\mathbf{K} + \mathbf{G})
 \end{aligned} \tag{2.44}$$

then,

$$\begin{aligned}
 & \left(\sum_{\mathbf{G}, \mathbf{G}'-\mathbf{G}} \hat{k}(\mathbf{G}' - \mathbf{G}) (\mathbf{K} + \mathbf{G}) \cdot (\mathbf{K} + \mathbf{G}) A(\mathbf{K}, \mathbf{G}) \exp[i(\mathbf{K} + \mathbf{G}'') \cdot \mathbf{r}] \right) \\
 & + \frac{\omega^2}{c^2} \sum_{\mathbf{G}} A(\mathbf{K}, \mathbf{G}) \exp[i(\mathbf{K} + \mathbf{G}) \cdot \mathbf{r}] = 0
 \end{aligned} \tag{2.45}$$

because of the symmetrical nature of the matrix can be write $\mathbf{G}'' = \mathbf{G} + \mathbf{G}'$, the above equation becomes,

$$\begin{aligned}
 & \left(\sum_{\mathbf{G}, \mathbf{G}''-\mathbf{G}} \hat{k}(\mathbf{G}'' - \mathbf{G}) (\mathbf{K} + \mathbf{G}'') \cdot (\mathbf{K} + \mathbf{G}) A(\mathbf{K}, \mathbf{G}) \exp[i(\mathbf{K} + \mathbf{G}'') \cdot \mathbf{r}] \right) \\
 & + \frac{\omega^2}{c^2} \sum_{\mathbf{G}} A(\mathbf{K}, \mathbf{G}) \exp[i(\mathbf{K} + \mathbf{G}) \cdot \mathbf{r}] = 0
 \end{aligned} \tag{2.46}$$

If the wave period $\exp [i(\mathbf{K} + \mathbf{G}'')]$ and take out only \mathbf{G}'' fulfilling this condition of $\mathbf{G}'' = \mathbf{G} \equiv \mathbf{G}'$, below equations can be obtained:

$$\sum_{\mathbf{G}} \hat{k} (\mathbf{G}''' - \mathbf{G})(\mathbf{K} + \mathbf{G}''') \cdot (\mathbf{K} + \mathbf{G}) A(\mathbf{K}, \mathbf{G}) \exp[i(\mathbf{K} + \mathbf{G}''') \cdot \mathbf{r}] + A(\mathbf{K}, \mathbf{G}''') \exp[i(\mathbf{K} + \mathbf{G}''') \cdot \mathbf{r}] = 0 \quad (2.47)$$

$$\sum_{\mathbf{G}} \hat{k} (\mathbf{G}''' - \mathbf{G})(\mathbf{K} + \mathbf{G}''') \cdot (\mathbf{K} + \mathbf{G}) A(\mathbf{K}, \mathbf{G}) + A(\mathbf{K}, \mathbf{G}''') = 0 \quad (2.48)$$

At last, if consider that

$$\mathbf{G} \rightarrow \mathbf{G}'$$

$$\mathbf{G}''' \rightarrow \mathbf{G}$$

following equation can be obtained

$$\sum_{\mathbf{G}} \hat{k} (\mathbf{G} - \mathbf{G}')(\mathbf{K} + \mathbf{G}) \cdot (\mathbf{K} + \mathbf{G}') A(\mathbf{K}, \mathbf{G}') + \frac{\omega^2}{c^2} A(\mathbf{K}, \mathbf{G}) = 0 \quad (2.49)$$

which has the form of a standard eigenvalue problem for a symmetric matrix.

E polarization

Same as H polarization, based on the [Eq. 2.11](#) and [Eq. 2.12](#), can be rewrite as:

$$\mathbf{H}(\mathbf{r}, t) = (\mathbf{H}_x(\mathbf{r}, \omega), \mathbf{H}_y(\mathbf{r}, \omega), 0) \exp(-j\omega t)$$

$$\mathbf{E}(\mathbf{r}, t) = (0, 0, \mathbf{E}_z(\mathbf{r}, \omega)) \exp(-j\omega t) \quad (2.50)$$

The Maxwell's curl equations in this case are:

$$\frac{\partial \mathbf{H}_y}{\partial x} - \frac{\partial \mathbf{H}_x}{\partial y} = -i\omega \varepsilon_0 \varepsilon_r(\mathbf{r}) \mathbf{E}_z$$

$$\frac{\partial \mathbf{E}_z}{\partial x} = -i\omega \varepsilon_0 \varepsilon_r(\mathbf{r}) \mathbf{H}_y$$

$$\frac{\partial \mathbf{E}_z}{\partial y} = i\omega \varepsilon_0 \varepsilon_r(\mathbf{r}) \mathbf{H}_z \quad (2.51)$$

Equation for \mathbf{E}_z can be obtain by eliminating \mathbf{H}_x and \mathbf{H}_y ,

$$\frac{1}{\varepsilon_r} \left[\frac{\partial^2}{\partial x^2} + \frac{\partial^2}{\partial y^2} \right] \mathbf{E}_z - \frac{\omega^2}{c^2} \mathbf{E}_z = 0 \quad (2.52)$$

To solve the equation above, the expansion of Eq. 2.51 is used and the equation is written in the form of $\mathbf{E}_z(\mathbf{r}, \omega)$ as follow,

$$\mathbf{E}_z(\mathbf{r}, \omega) = \sum_{\mathbf{G}} A(\mathbf{K}, \mathbf{G}) \exp[i(\mathbf{K} + \mathbf{G}) \cdot \mathbf{r}] \quad (2.53)$$

by substituting the above equation with Eq. 2.52, following equation can be obtain,

$$\sum_{\mathbf{G}} \hat{k}(\mathbf{G} - \mathbf{G}') (\mathbf{K} + \mathbf{G})(\mathbf{K} + \mathbf{G}') A(\mathbf{K}, \mathbf{G}') - \frac{\omega^2}{c^2} A(\mathbf{K}, \mathbf{G}) = 0 \quad (2.54)$$

Knowing that in the determination of photonic band structures, Fourier coefficients $\hat{k}(\mathbf{G} - \mathbf{G}')$ of $\varepsilon_r^{-1}(\mathbf{r})$ plays a main role for both polarizations. So, to determine them, following equation is written in the form of $\varepsilon_r^{-1}(\mathbf{r})$

$$\frac{1}{\varepsilon_r(\mathbf{r})} = \frac{1}{\varepsilon_b} + \left[\frac{1}{\varepsilon_a} - \frac{1}{\varepsilon_b} \right] \sum_1 S(\mathbf{r} - \mathbf{r}(1)) \quad (2.55)$$

where ε_a is the dielectric constant of the rods, ε_b is the dielectric constant of the material with,

$$S(\mathbf{r}) = \begin{cases} 1 & \dots \mathbf{r} \in \mathbf{R} \\ 0 & \dots \mathbf{r} \in \mathbf{R} \end{cases} \quad (2.56)$$

where \mathbf{R} is the region of the xy -plane. The Fourier coefficient is given by

$$\begin{aligned} \hat{k}(\mathbf{G}) &= \frac{1}{a_c} \int_{a_c} d^2 r \exp(-i\mathbf{G} \cdot \mathbf{r}) \frac{1}{\varepsilon(\mathbf{r})} \\ &= \frac{1}{\varepsilon_b} \delta_{\mathbf{G},0} + \left[\frac{1}{\varepsilon_a} - \frac{1}{\varepsilon_b} \right] \frac{1}{a_c} \int d^2 r \exp(-i\mathbf{G} \cdot \mathbf{r}) S(r) \end{aligned} \quad (2.57)$$

where the integration in the second line of this equation is over the entire xy -plane.

2.4.2 Finite difference time domain (FDTD) method

The finite difference time domain (FDTD) has become the method of choice to calculate the light propagation in dielectric materials due to the simple discretization process. The FDTD method calculate the electric and magnetic field distribution by employing a lattice that contain tiny cell called the Yee cell where the electric and magnetic fields are at different positions with a spatial difference of half of lattice constant.

FDTD method is commonly used for computing the numerical calculations because easy to understand and directly follows the differential form of Maxwell's equation.

From the Eq. 2.8, can be written as:

$$\begin{aligned}\frac{\partial \mathbf{H}_x}{\partial t} &= -\frac{1}{\mu} \frac{\partial \mathbf{E}_z}{\partial y} \\ \frac{\partial \mathbf{H}_y}{\partial t} &= \frac{1}{\mu} \frac{\partial \mathbf{E}_z}{\partial x} \\ \frac{\partial \mathbf{H}_z}{\partial t} &= \frac{1}{\mu} \left(\frac{\partial \mathbf{E}_x}{\partial y} - \frac{\partial \mathbf{E}_y}{\partial x} \right)\end{aligned}\quad (2.58)$$

From the Eq. 2.10, can be written as:

$$\begin{aligned}\frac{\partial \mathbf{E}_x}{\partial t} &= \frac{1}{\varepsilon} \frac{\partial \mathbf{H}_z}{\partial y} \\ \frac{\partial \mathbf{E}_y}{\partial t} &= -\frac{1}{\varepsilon} \frac{\partial \mathbf{H}_z}{\partial x} \\ \frac{\partial \mathbf{E}_z}{\partial t} &= \frac{1}{\varepsilon} \left(\frac{\partial \mathbf{H}_y}{\partial x} - \frac{\partial \mathbf{H}_x}{\partial y} \right)\end{aligned}\quad (2.59)$$

Both Eq. 2.58 and Eq. 2.59 can be grouped according to the field vector components. One set involving only \mathbf{E}_x , \mathbf{E}_y and \mathbf{H}_z and another set involving \mathbf{H}_x , \mathbf{H}_y and \mathbf{E}_z which referred to respectively as the transverse electric (TE) and transverse magnetic (TM) modes.

The sets of equations are given as:

$$\begin{aligned}\text{TM mode} \quad \frac{\partial \mathbf{H}_x}{\partial t} &= -\frac{1}{\mu} \frac{\partial \mathbf{E}_z}{\partial y} \\ \frac{\partial \mathbf{H}_y}{\partial t} &= \frac{1}{\mu} \frac{\partial \mathbf{E}_z}{\partial x} \\ \frac{\partial \mathbf{E}_z}{\partial t} &= \frac{1}{\varepsilon} \left(\frac{\partial \mathbf{H}_y}{\partial x} - \frac{\partial \mathbf{H}_x}{\partial y} \right)\end{aligned}\quad (2.60)$$

and

$$\begin{aligned}
 \frac{\partial \mathbf{E}_x}{\partial t} &= \frac{1}{\varepsilon} \frac{\partial \mathbf{H}_z}{\partial y} \\
 \frac{\partial \mathbf{E}_y}{\partial t} &= -\frac{1}{\varepsilon} \frac{\partial \mathbf{H}_z}{\partial x} \\
 \frac{\partial \mathbf{H}_z}{\partial t} &= \frac{1}{\mu} \left(\frac{\partial \mathbf{E}_x}{\partial y} - \frac{\partial \mathbf{E}_y}{\partial x} \right)
 \end{aligned}
 \tag{2.61}$$

Two-dimensional structure is set in x - y plane and the electromagnetic wave has electric field in the x - y plane while the magnetic field is in z direction. Therefore, the electromagnetic wave is TE wave.

A portion of Yee cell constituting a unit cell for the TE wave is depicted in Fig. 2.8. The \mathbf{E}_x component is located at half x and integer y grid points, i.e., $(i + 1/2, j)$, while the \mathbf{E}_y component is located at integer x and half y grid points, i.e., $(i, j + 1/2)$. The magnetic field component \mathbf{H}_z is located at half x and half y grid points, i.e., $(i + 1/2, j + 1/2)$. These grid points are chosen to accommodate the interleaved leapfrog algorithm that makes up FDTD method.

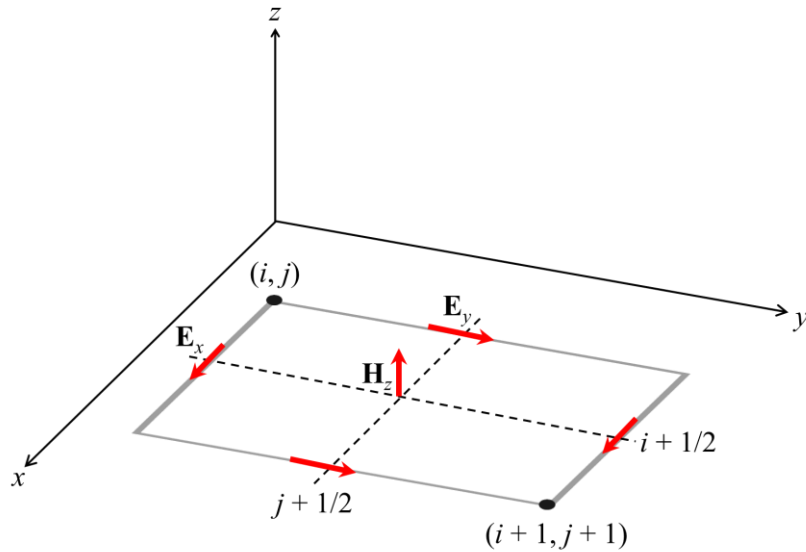


Fig. 2.8 A FDTD unit cell for TE waves. The small vectors with thick arrows are placed at the point in the mesh at which they are defined and stored. For example, \mathbf{E}_y is defined at mesh point $(i, j + 1/2)$, while \mathbf{H}_z is defined at mesh points $(i + 1/2, j + 1/2)$.

The spatially discretized versions of the component Maxwell's Eq. 2.61 are:

$$\begin{aligned} \frac{\partial \mathbf{E}_x}{\partial t} \Big|_{i+\frac{1}{2},j} &= \frac{1}{\varepsilon} \left[\frac{\mathbf{H}_z \Big|_{i+\frac{1}{2},j+\frac{1}{2}} - \mathbf{H}_z \Big|_{i+\frac{1}{2},j-\frac{1}{2}}}{\Delta y} \right] \\ \frac{\partial \mathbf{E}_y}{\partial t} \Big|_{i,j+\frac{1}{2}} &= -\frac{1}{\varepsilon} \left[\frac{\mathbf{H}_z \Big|_{i+\frac{1}{2},j+\frac{1}{2}} - \mathbf{H}_z \Big|_{i-\frac{1}{2},j+\frac{1}{2}}}{\Delta x} \right] \\ \frac{\partial \mathbf{H}_z}{\partial t} \Big|_{i+\frac{1}{2},j+\frac{1}{2}} &= \frac{1}{\mu} \left[\frac{\mathbf{E}_x \Big|_{i+\frac{1}{2},j+1} - \mathbf{E}_x \Big|_{i+\frac{1}{2},j}}{\Delta y} - \frac{\mathbf{E}_y \Big|_{i+1,j+\frac{1}{2}} - \mathbf{E}_y \Big|_{i,j+\frac{1}{2}}}{\Delta x} \right] \end{aligned} \quad (2.62)$$

For the time derivatives, at the FDTD algorithm for TE waves:

$$\begin{aligned} \mathbf{H}_z \Big|_{i+\frac{1}{2},j+\frac{1}{2}}^{n+\frac{1}{2}} &= \mathbf{H}_z \Big|_{i+\frac{1}{2},j+\frac{1}{2}}^{n-\frac{1}{2}} + \frac{\Delta t}{\mu_{i+\frac{1}{2},j+\frac{1}{2}}} \times \left[\frac{\mathbf{E}_x \Big|_{i+\frac{1}{2},j+1}^n - \mathbf{E}_x \Big|_{i+\frac{1}{2},j}^n}{\Delta y} - \frac{\mathbf{E}_y \Big|_{i+1,j+\frac{1}{2}}^n - \mathbf{E}_y \Big|_{i,j+\frac{1}{2}}^n}{\Delta x} \right] \\ \mathbf{E}_x \Big|_{i+\frac{1}{2},j}^{n+1} &= \mathbf{E}_x \Big|_{i+\frac{1}{2},j}^n + \frac{\Delta t}{\varepsilon_{i+\frac{1}{2},j} \Delta y} \left[\mathbf{H}_z \Big|_{i+\frac{1}{2},j+\frac{1}{2}}^{n+\frac{1}{2}} - \mathbf{H}_z \Big|_{i+\frac{1}{2},j-\frac{1}{2}}^{n+\frac{1}{2}} \right] \\ \mathbf{E}_y \Big|_{i,j+\frac{1}{2}}^{n+1} &= \mathbf{E}_y \Big|_{i,j+\frac{1}{2}}^n - \frac{\Delta t}{\varepsilon_{i,j+\frac{1}{2}} \Delta x} \left[\mathbf{H}_z \Big|_{i+\frac{1}{2},j+\frac{1}{2}}^{n+\frac{1}{2}} - \mathbf{H}_z \Big|_{i-\frac{1}{2},j+\frac{1}{2}}^{n+\frac{1}{2}} \right] \end{aligned} \quad (2.63)$$

2.5 PhC nanocavity design structure

Fig. 2.9 shows the schematic illustration of designed PhC nanocavity structure that used in this study. It is called a width-modulated line defect cavity who's the width of the line-defect structure is locally modulated. The confinement in the direction of a line defect is results from the existence of a mode gap in the waveguide. The confinement in the mode gap was created by changing the location geometrical parameter such as width of the line defect [92]. This kind of structure has reported to achieve a high- Q factor by an air-hole triangular lattice with an air-clad [37]. They have reported before that by width modulation, a poor- Q cavity factor achieved due to the unoptimized structure and SiO₂-clad [93].

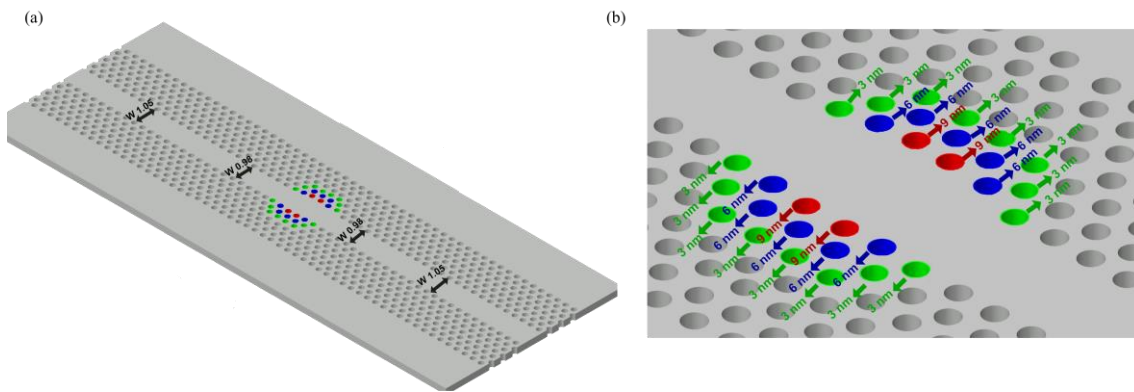


Fig. 2.9 (a) Schematic illustration of PhC nanocavity structure design used in this study. Cavity is created at the center of the structure. (b) Cavity is created by shifting holes position to 9 nm (red), 6 nm (blue) and 3 nm (green) towards outside.

The band diagram of the line defect is shown in the Fig. 2.10 (a). The mode gap was shifted to a lower frequency due to the increased of the line defect width. Therefore, frequency component that is close to the mode gap, such as wave vector component that close to the Brillouin edge will localize when a certain position shift of hole is created in the waveguide. Hence, the center part of the holes are shifted from the waveguide by some distances. Fig. 2.9 (b) shows an enlarge image at center of the waveguide PhC nanocavity structures which represents the distance of holes shifting.

However, design of a high- Q cavity in PhC nanocavity becomes challenging when the cladding material (such as SiO₂) of the refractive index is high (1.44) because cavity mode should have small wave vector in the light cone [94]. However, based on the band diagram shown in the Fig. 2.10 (a), the localized mode for width modulated line defect wave vector of SiO₂-clad is below the light line. Therefore, small vertical radiation loss is achieved. In order to achieve a high- Q factor, the vertical radiation loss need to be reduced [30], [95]

The FDTD calculation for the PhC nanocavity with SiO₂ clad has been performed [87] with the center of the holes shifted to 2, 4 and 6 nm and high- Q of $\sim 7.1 \times 10^6$ is obtained at the mode volume of $\sim 2.4 (\lambda/n)^3$. The results are shown in Figs. 2.10 (b) and (c) shows the spatially Fourier transformed k -space where small component appear in the light cone of the SiO₂. This indicate that the radiation loss of the SiO₂ is low.

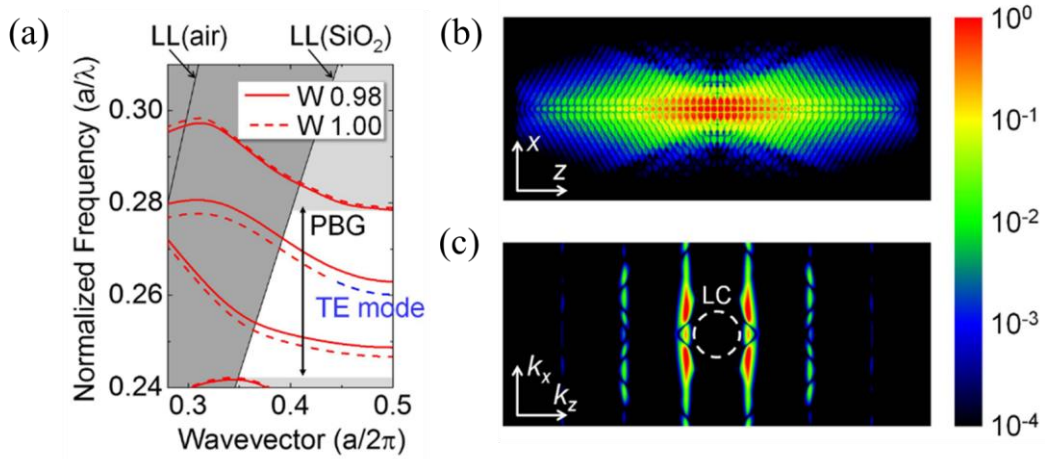


Fig. 2.10 PhC nanocavity structure with SiO₂-clad where the holes shifted to 2, 4 and 6 nm. The slab thickness, t is 204 nm, lattice constant, a is 420 nm and air hole diameter is 216 nm. (a) Dispersion band diagram with SiO₂ clad. The light line (LL) for both air and SiO₂ clad are shown in the graph. (b) The 3D FDTD calculation of H_z cavity mode profile of width-modulated line defect. (c) The white dashed line is light cone (LC) of the SiO₂ clad. [Reprinted with permission from Y. Ooka, *et al.*, *Sci. Rep.*, **5** (11312), 2015]

In the experiment, the holes shifted to 3, 6 and 9 nm away from the waveguide with the slab thickness, t is 210 nm, lattice constant, a is 420 nm and the air-hole diameter is 246 nm. The FDTD calculation and the spatially Fourier transformed k -space results is shown in Fig. 2.11. The obtained value of the Q factor is 8.1×10^5 with a mode volume of $\sim 1.7 (\lambda/n)^3$. The SEM image of the structure is shown in Fig. 2.12 (a). Figs. 2.12 (b) and (c) shows the experimental result of the optical transmission spectrum when continuous-wave (CW) laser is input into the waveguide. It shows a peak which is the cavity resonance at 1619.20 nm where the loaded Q value is 2.2×10^5 . The sharp edge at the transmission spectrum is due to the mode-gap barrier of W 0.98 PhC waveguide. When CW laser light is input at the cavity resonance, light scattering from the cavity is clearly can be observed which shows that the light is localized in the cavity at the cavity resonance wavelength.

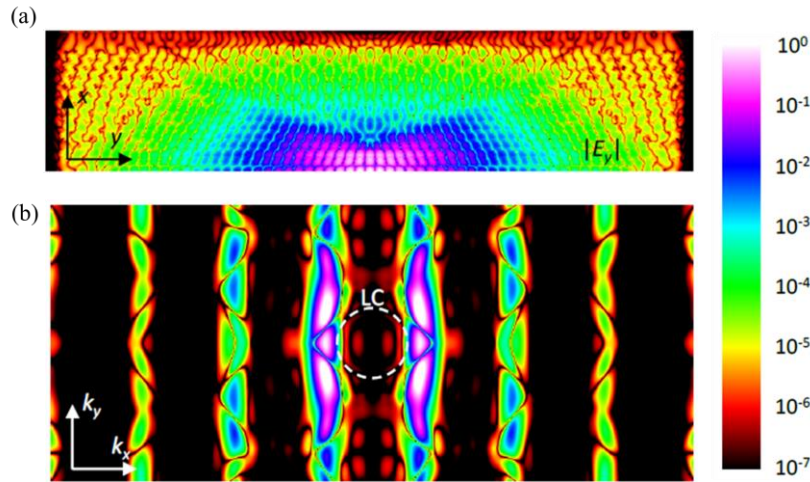


Fig. 2.11 PhC nanocavity structure used in this study with SiO₂-clad where the holes shifted to 3, 6 and 9 nm. The slab thickness, t is 210 nm, lattice constant, a is 420 nm and air hole diameter is 246 nm. (a) $|E_y|$ profile at resonance. (b) The k -space of the cavity mode in (b). The white dashed circle represents the light cone (LC) of the SiO₂-clad.

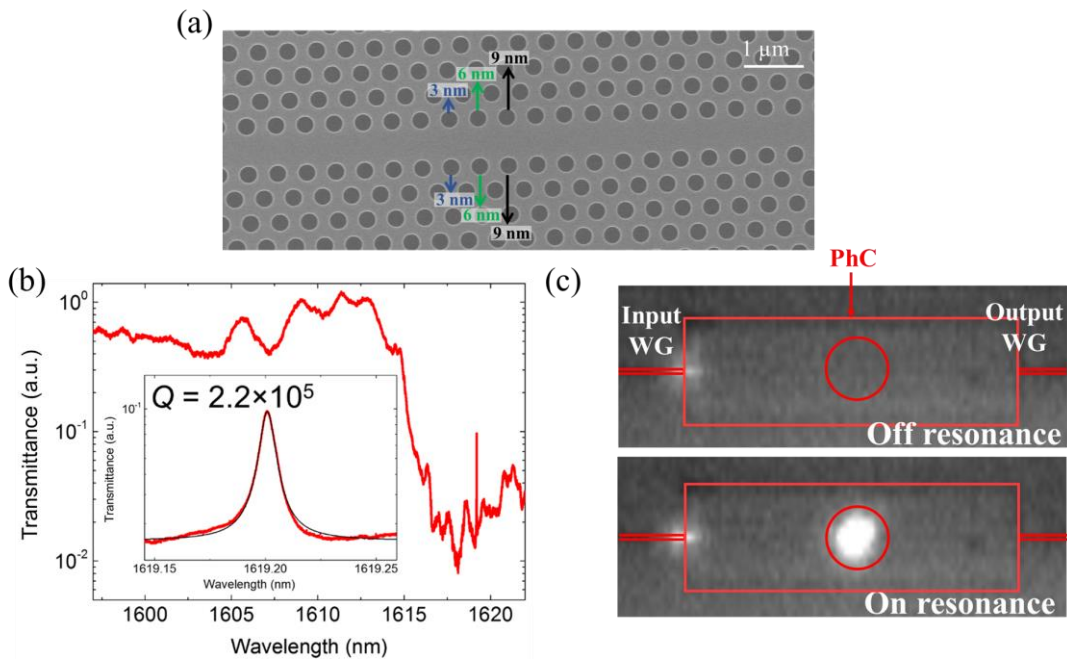


Fig. 2.12 (a) SEM image of the PhC nanocavity. (b) Transmission spectrum of the structure. The inset is the enlarge of the peak transmission. It shows that cavity resonance occurred at 1619.20 nm wavelength of Q is 2.2×10^5 . (c) Image from the IR camera of on and off resonance. On resonance, light is localized at the cavity.

2.6 Summary

As a summary, this chapter explains the basic theory of PhC structure which is the main material components in this study. The Maxwell's equations have been introduced to understand the electromagnetic propagation in dielectric material. The dispersion diagram shows clearly, the existence of PBG in the periodic structure which makes the creation of cavity in the structure becomes possible. The theories of numerical methods also are explained. Finally, the design of the PhC nanocavity structure which has be the main device in this study is introduced. The mode-gap confinement with the width modulated line defect structure exhibits high- Q factor with low mode volume.

Chapter 3

PhC nanocavity laterally embedded with *p-i-n* diode fabrication process

This chapter will describe the fabrication process of two-dimensional PhC nanocavity. First, common fabrication process to fabricate the PhC structure is reviewed. Then, method of fabrication process to fabricate the PhC nanocavity and the integration of *p-i-n* diode that used in this study will be explained. Finally, the advantages of current fabrication process are described in this chapter.

3.1 Introduction

PhC has promise to revolutionize the ability to manipulate light. Theory of PhC has been introduced in the early of 1980s, however the initial attempts of during that period, relied on their scaling properties. Therefore, when Yablonovitch's reported that complete PBG can be occurred in 3D PhC [4], the lattice constant of the crystal was in millimetres (mm) order. This showed that on that period, he was not constrained to difficult and expensive micro- or nano-fabrication techniques. Thus, he has fabricated his design whose named as Yablonovite by simply drilling a series of holes in a block of material which was lauded as the first successful creation of PhC

exhibiting three-dimension PBG. However, this bandgap only existed across ambiguous spectrum of microwave frequencies. Nevertheless, Yablonovitch's experiment primarily work as a proof of concept. Even though the fabrication of the PhC structure has become a major challenge in this study.

Today's, the methods of PhC fabrication has been expand rapidly, thanks to the advancement of technology. With the sufficient precision of fabrication technique nowadays, the scattering losses lead to blurring the crystal properties, is possible to be prevent. Moreover, some of the processes allows the PhC structure to become robustly mass produced.

3.2 Overview of PhC fabrication process

The major challenge in order to fabricate PhC structure are precision to avoid scattering loss that will blurring the crystal properties and process that can robustly mass-produce crystals. Therefore, the main promising method for PhC fabrication that has been commercially available in fiber communication field is by photonic-crystal fiber. There are many categories of photonic-crystal fiber such as photonic-bandgap fiber, holey fiber, hole-assisted fiber and Bragg fiber [96]–[98].

Another promising method is called photonic crystal slab which using two-dimensional PhC structure. This kind of method can be fabricate using the techniques from semiconductor industry. The PhC slab normally consists of silicon material and has an advantage in order to integrate photonic processing circuits with electronic processing circuit on a single chip. Several methods of fabrication techniques from the semiconductor industry is possible to fabricate the PhC slab structure. Perhaps, among these, the most popular fabrication technique which has exploits enormous amount of research is layer-by-layer lithography technique which has been used in 1994.

The main idea of this technique is to etch a cross section of the PhC pattern onto a substrate, the etched holes can be created from air of backfill with SiO_2 and finally deposit another layer of substrate. Since this technique is so-called layer-by-layer, each process is repeated for each desired cross section of the PhC pattern. The etching process in this technique can be performed in several ways, such as electron-beam lithography, interference lithography and photolithography.

The electron-beam lithography or often called as e-beam (EB) lithography. EB lithography uses a focused beam of electrons to draw or 'drill' custom shape (normally holes) on a surface that covered with an electron-sensitive film called a resist [99]. During the resist process, the EB causes a chemical change at the expose area. This technique is capable of very high resolution and flexible to work with various types of material. Therefore, this technique is preferable for creating extremely fine patterns due to the precision. Hence, many research groups, has extensively used this technique for making photonic integrated circuits [78], [100]–[102]. Nonetheless, this technique is slow which is a few orders of magnitude slower than optical lithography. Plus, due to the precision and high resolution, this technique is expensive and requires complicated process [103]. Therefore, EB lithography is not preferable for mass production.

On the other hand, interference lithography offers an alternative technique. This technique is also known as holographic lithography. The basic principle of the technique is the

interference pattern which is created by numbers of high-frequency beams in order to imprint the custom pattern onto a photosensitive resin [104]–[106]. Different number of beams frequency will generate different arrays. Such as, 3-beams interference will generate arrays with hexagonal symmetry, while 4-beams, rectangular symmetry or three-dimensional PhC arrays can be generated. After a particular layer is completed, the resin is exposed to UV light and the process repeated by depositing the next layer.

The interference lithography is much cheaper in terms of cost compared to EB and fast in speed as the whole pattern possible to be imprinted simultaneously. Due to the small wavelength, this technique able to have high resolution and have been used to widely in submicron structures [107]–[110]. However, this technique faces a difficulty in calculating appropriate beam parameters to generate correct interface pattern. Furthermore, due to the uniformity of the interference pattern, makes the creation of defect becomes difficult.

Another alternative technique is photolithography which is also termed as optical lithography or UV lithography. The fundamental principle of this technique is similar to photography where the pattern in the etching resist is created by exposing it to light either directly or using an optical mask. This technique basically consists of coating the planar substrate with photoresist, light source exposure, wet or dry etching and photoresist removal [111], [112]. The photolithography process is comparable with high precision method and ability to fabricate ultra-small pattern (few nanometres size). Moreover, as it allows patterns to be created over an entire surface, this technique promises cost-effectively. Hence, it has been widely used in many research groups [113]–[117]. Even though the precision of photolithography is comparable with other high precision method, it is still not enough in PhC field as it requires a precision un nanoscale order. Thus, this technique may lack of accuracy.

3.3 Photolithography fabrication procedure

Photolithography has been extensively used in silicon photonics devices due to its cost-effective and most importantly, compatible with CMOS devices [118]–[120]. So, it allows the silicon photonics circuits to be integrated on the same chip with electronic circuits. Therefore, device that used in this study, was fabricated using photolithography fabrication process.

3.3.1 Device fabrication process

The basic procedure process of the photolithography consists of resist coating, development, etching and removal. The illustration in Fig. 3.1 shows the summary of fabrication process.

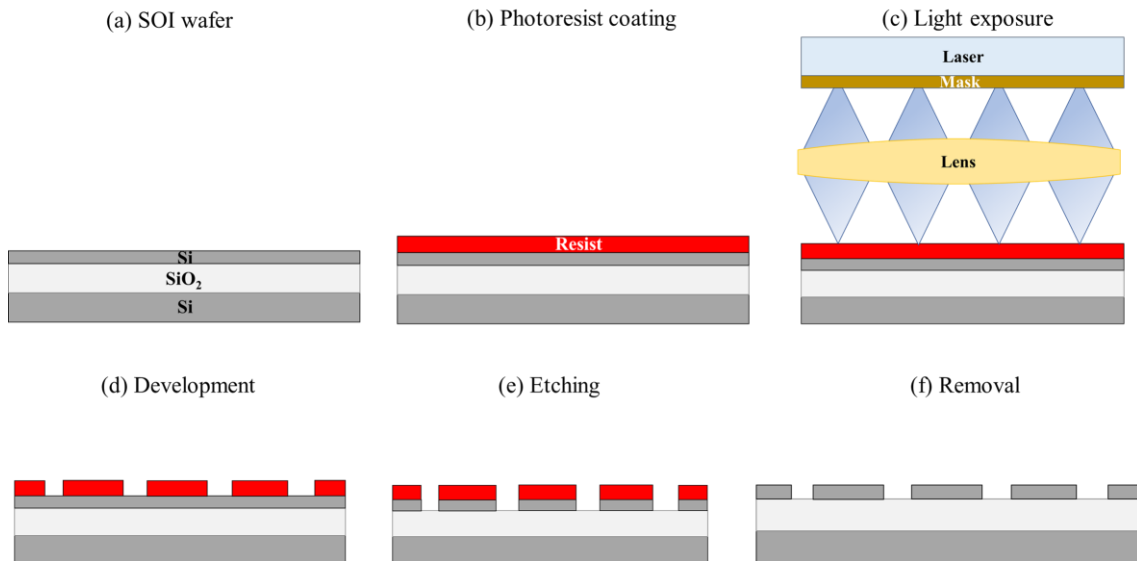


Fig. 3.1 The photolithography procedure. (a) Substrate of SOI wafer. (b) The top layer undergoes a photoresist coating. (c) Light exposure where laser is radiated through the mask and focused on the resist layer by a lens. (d) Development of the photoresist. (e) Silicon layer etching. (f) The resist is removed and the desired patterns are fabricated on the silicon layer

First of all, substrate of silicon-on-insulator (SOI) wafer is prepared. It contains of Si at the bottom and top layer while SiO₂ is at the middle of the layer. Then small amount of photoresist is applied to the SOI substrate. Photoresist is a liquid chemical and can be applied to the SOI substrate in several ways, but commonly spin coated is used. A spin coater is an enclosed turntable that will spin at around 3000 rpm. It holds the wafer on its platter with a vacuum. The photoresist dries by solvent loss as it thins out via spinning. As a result, a thin uniformed layer is produced.

Next, the substrate will be exposed to the light. Contact and proximity lithography are the simplest methods of exposing a photoresist where the photomask is placed on the photoresist-coated wafer, and intense light is applied. However, contact lithography in practical has a possibility to damage the mask and resulting low yield that make the process unstable, while for proximity lithography, possible to reduce mask damage due to the distance of mask, but this will increase the resolution limit to greater number. Hence, projection lithography which employ scanning and step-and-repeat systems. Reflective optics is used to project a slit of light from mask onto the substrate as the mask and substrate will move simultaneously by the slit. The light exposure dose is determined by the intensity of light, the slit width and the speed the substrate is scanned. Stepper is the step-and-repeat camera used to expose the substrate and will make sure the it moves precisely as step.

The exposure to the light source requires short wavelength, high intensity and precision optics to focus light. There are two source of light that are generally used – high-pressure mercury lamp and excimer laser. In the fabrication process of PhC nanocavity, excimer laser is used. An excimer laser is a form of ultraviolet (UV) laser that commonly used in the production of semiconductor based integrated circuits. Excimer molecules is the source of laser action. The molecule consists of noble gasses such as argon, krypton and xenon and halogens. Those noble

gases together with halogens will form a bound molecule and formed only in excited state. They did not have ordinal ground state but repulsive ground state. Hence, high power laser is irradiated through spontaneous or stimulated emission. In photolithography light sources, XeF, XeCl, KrF and ArF are generally used. The wavelength of the excimer laser and mercury lamp is shown in Table 3.1.

Table 3.1 Photolithography light source with corresponding wavelength

Light source	Name	Wavelength (nm)
Mercury Lamp	G-line	436
	H-line	405
	I-line	365
Excimer Laser	XeF	351
	XeCl	308
	KrF	248
	ArF	193

Next, once exposed, the photoresist needs to be developed. The development is undoubtedly one of the most critical steps in photoresist process. The characteristics of the resist developer interactions determine to a large extent the shape of the photoresist. The method of applying developer to the photoresist is important in controlling the development uniformity. Then, after the small patterns have been lithographically printed in the photoresist, the patterns must be transferred in the substrate. There are three basic pattern approaches that are, subtractive transfer (etching), additive transfer (selective deposition) and impurity doping (ion implantation). In this device, subtractive transfer (etching) has been used. Etching is performed using wet chemicals such as acids or in a dry plasma environment. After the etching is complete, the resist is removed to leave the desired pattern etched in the deposited layer.

In this study, after completing the design structure as described in Ch. 2 Sec. 2.4, then, the designed was sent to Institute of Microelectronics (IME) located in Singapore to fabricate. It is an open silicon photonics foundry with a standard CMOS process line. The PhC nanocavity device is fabricated with KrF stepper lithography at the wavelength of 248 nm.

Table 3.2 Layers number and corresponding structures

Layer #	Structure	Layer #	Structure
1	Si	13	Contact hole (p, n)
2	Rib	14	Si n implant
3	PhC	15	Si p implant
4	Silica trench at SSC	16	Si n^+ implant
5	Clad window at PhC	17	Si p^+ implant
6	Clad window at Si wire	18	Ge n implant
7	Facet deep trench	19	Si p implant for PD
8	Heater isolation trench	20	Ge window
9	Al wire	21	Probing/bonding pad
10	Contact hole (heater)	22	Si_3N_4
11	Heater (upper layer)	23	Grating
12	Heater (lower layer)		

Table 3.2 show the layers number which refers to the type of the structure which has been provided by the IME. Some of the layers are fabricated with high definition mask (HDM) and some with low definition mask (LDM). Layers number 1, 3, 14 & 15 and 23 are fabricated with HDM with the value of resolution is 1 nm. Layers number 2, 4 to 13 and 16 to 22 are fabricated with LDM and the resolution is 5 nm. Layer number 3 has been fabricated using stepper lithography which means that the step machine moves very precisely to fabricate the PhC structure. Fig. 3.2 shows the SEM image of the fabricated PhC structure.

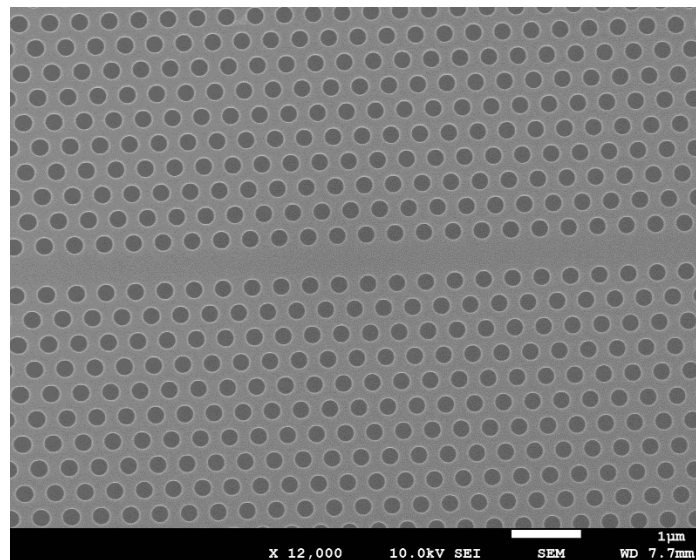


Fig. 3.2 SEM image of PhC nanocavity fabricated by photolithography process.

3.3.2 Integration of *p-i-n* diode

After describing the fabrication process for the PhC structure, the integration of *p-i-n* diode on the device will be explained in this section. The *p-i-n* diode was laterally integrated on the device as shown in Fig. 3.3. The integration of the *p-i-n* diode is done by the same IME services as they provided the *p-n* doping. Fig. 3.4 shows the cross-section of the device.

In order to achieve a high- Q cavity factor, the *p-n* structure need to be positioned laterally instead of vertically. This is because, at the vertical positioned, large absorption at the *p* diode and *n* diode layers overlaps the optical mode, so low Q factor is achieved. Therefore, a lateral *p-i-n* diode structure is required to overcome the overlap between the optical mode and the *p* and *n* region. Lateral *p-i-n* diode structure has been fabricated with PhC waveguides on SiO₂ [121] but reportedly achieved low Q factor due to the SiO₂ cladding [94], [122].

In this device, the cavity area in the structure basically works as *i* region because it contains no dopant. The distance, w_i of the *i* region is 2.9 μm and was implanted at the center of a W 0.98 waveguide which also the center of the device.

The *p* diode is positioned exactly above the *i* region with the width, w_w is 1.68 μm . The *p* diode doping concentration is $2.4 \times 10^{17} \text{ cm}^{-3}$. The *n* diode is positioned at the bottom of the *i* region with the same width, w_w as *p* diode. The doping concentration for this diode is $1.4 \times 10^{17} \text{ cm}^{-3}$. Boron and phosphorous ions are implanted at a dose of 10^{12} cm^{-2} . The implantation activation is done at 1030 $^\circ\text{C}$, 5 s after the implantations.

As shown in the Fig. 3.3, the *p* and *n* diodes are connected to the aluminium (Al) pads which work as a conductive part to allow the flow of currents when voltage is applied to the structure. The size of the contact pads is $45 \times 45 \mu\text{m}$ which is enough for the probe tip's pitch to contact with the pads. The contact pads were positioned 2.0 μm above the Si layer surface and the thickness is approximately 0.75 μm . The surface of the contact pads is covered with a thin SiO₂ layer as well. The contact pads could not be seen via SEM image as it has been removed together with the SiO₂ layer.

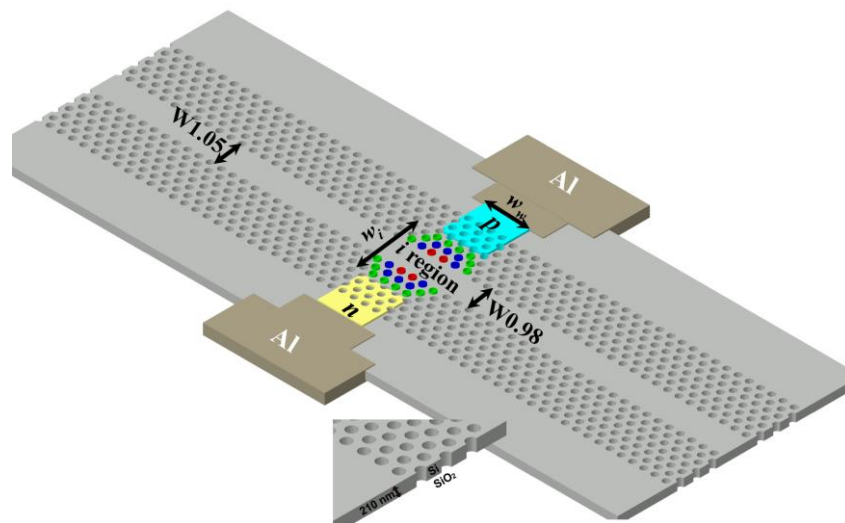


Fig. 3.3 Schematic illustration of the laterally integrated *p-i-n* diode with the Al contact pads.

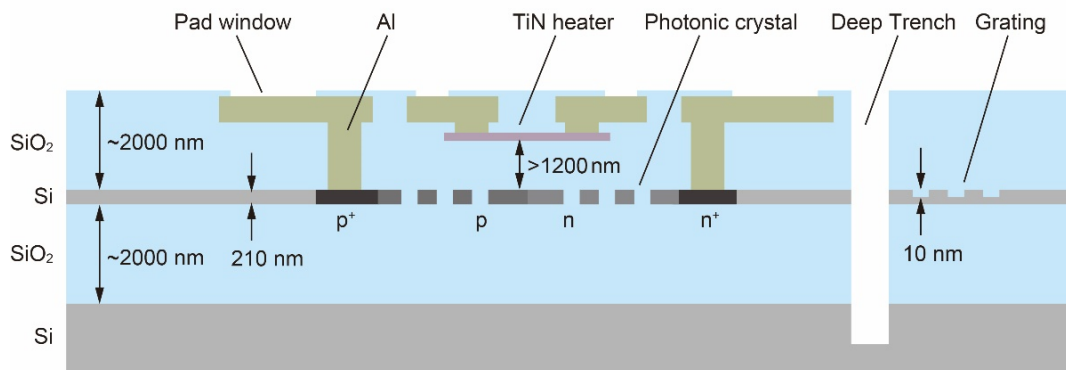


Fig. 3.4 Cross-section of the fabricated device.

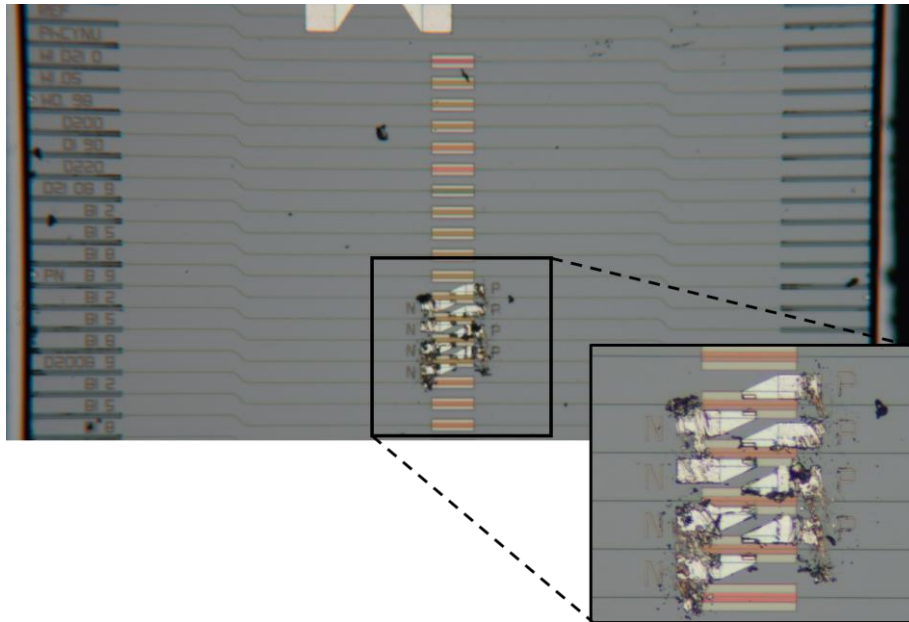


Fig. 3.5 IR image of the fabricated *p-i-n* diode and Al contact pads. The inset shows the enlarge image. The scratch on the contact pads is caused by the probe's tip.

3.4 Comparison with previous study's device

Similar device has been reported several years ago by NTT Laboratories [61] as shown in Fig. 3.6. However, the device has been fabricated by EB lithography and dry etching fabrication process. This device requires an air-bridge structure in order to achieve a high- Q cavity factor. It exhibits a high loaded Q of about 5.4×10^5 . However, the creation of the air-bridge structure requires the removal of a sacrificial silica (SiO₂) layer by isotropic etching. The creation of an air-bridge structure is frangible and unstable. Hence, it will be difficult to integrate the device with other silicon photonics devices that is generally cladded with SiO₂ on a single chip.

The existence of the air-bridged PhC structure makes the fabrication of the *p-i-n* diode becomes complex. The EB resist is used to selectively implant the ions and annealing is required

to activate the implanted ions. The annealing process is challenging where it needs to heat the SOI wafer to a temperature of 1000 °C for 30 minutes and then cooling it down at a very slow and controlled rate.

That is not all, the contact Al pads need to be protected particularly during the air-bridging process. During the process, the Al contact pads were protected with a resist. Finally, the SiO₂ layer is removed through wet etching process to leave only the Al contact pads on the SOI wafer.

On the other hand, the device that is fabricated using KrF photolithography process, which is used in this study does not require extra fabrication process to achieved high- Q factor. it has been reported that the device exhibits high- Q of 2.2×10^5 . Plus, since it is cladded with SiO₂-clad, it is possible to integrate with other silicon photonic devices on a single chip.

The CMOS compatible fabrication process that has been used to fabricate the device in this study, is expected to reproducibly high stability compared to the EB lithography fabrication device.

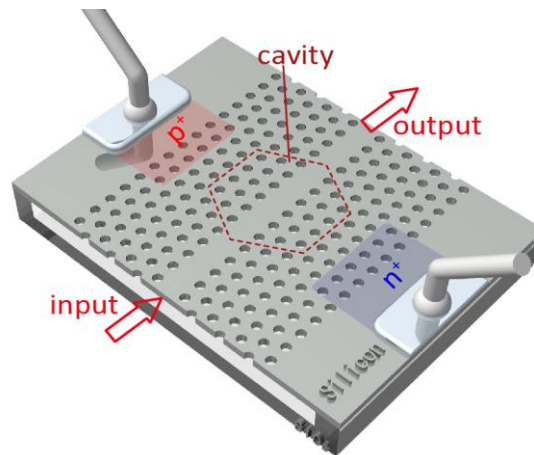


Fig. 3.6 Schematic illustration of the PhC nanocavity fabricated by EB lithography. [Reprinted with permission from T. Tanabe, *et al.*, *Applied Phys Lett.* **96** (101103), 2010]

3.5 Summary

In summary, this chapter described the basic fabrication process that has been used to fabricate PhC structure. Detailed about the PhC nanocavity device used in this study fabrication process also has been explained. Finally, the comparison between previously reported device and this study's device is made to describe the merit.

Chapter 4

Electro-optic modulator based on PhC nanocavity

This chapter will describe the demonstration of PhC nanocavity that is integrated with *p-i-n* diode as an electro-optic modulator based on carrier injection. The high- Q PhC nanocavity device shows 2.76 μW of power consumption is achievable due to the small capacitance value of the device which is importance element to perform a signal modulation. This is due to the compactness of the device footprint in which 50 μm^2 . Refractive index modulation is demonstrated via the carrier plasma dispersion effect, with modulation voltage of 1.0 V at 0.5 GHz repetition frequency. The cut-off frequency of the device is 0.35 GHz.

4.1 Introduction

Optical technology is the best candidate to overcomes the limitation of copper as an interconnect due to its cost effectiveness. Therefore, optical interconnect with silicon photonics is one of the best candidates because of its low fabrication costs, great performance resulting from electronic to photonic integration and most importantly compatibility with the CMOS devices which has been the main technology in world in producing electronics components. That is not all, optical interconnect with silicon photonics also is expected to reduce the power consumption of signal

processing by replacing electrical wire with photonic waveguides [82], [123]–[126]. This has made the silicon photonics as a leading candidate in optical interconnect.

The main target of optical interconnect is to increase the performance of data centers since optical technology is broaden at very short distance range. The main components in optical interconnect are the optical modulation part which is known as an optical modulator. The light propagating signal will be modulated either in free space or in an optical waveguide. The development of optical modulator has been vigorously fast nowadays. Various mechanism has been proposed in order to achieve better modulation in silicon which is either by hybrid combination with other devices such as germanium [127]–[131], graphene, polymers [132]–[136] and group III-V materials [137]–[139] or monolithic form from silicon (all-Si optical modulator) [55], [140]–[146].

Generally, monolithic modulators have attracted more attention due to the compatibility with CMOS devices and simplicity fabrication. Most of them are operating using plasma dispersion effect. On the other hand, hybrid modulator required a complexity of fabrication and incompatible with CMOS processes. However, hybrid modulator offers an advantage in terms of optical source. For example, by introducing III-V material onto silicon waveguide, most efficient light source in silicon is achieved although the requirement of light source integration on chip is being argued.

4.2 Motivation

Since monolithic modulators is more attractive, many studies have been conducted to achieve most high performance of optical modulator. In early years, lithium niobite (LiNbO_3) modulator has shown a good performance in terms of high-speed modulator in which 75 GHz operation speed [47]. Due to the good performance, LiNbO_3 modulator has become commercialized in industry. However, LiNbO_3 modulator suffer a high operating voltage of 7 V and large footprint. Therefore, researchers are trying to pursue a high operating speed, low operating voltage and small footprint of electro-optic modulator. Since then, performance metrics such as modulation bandwidth, power consumption and footprint of device become a competition among researchers. Various structure and modulation principle are introduced to increase the performance of modulator but on the same time remain in small footprint. For example, Mach-Zehnder interferometer (MZI) modulator structure has been demonstrated by different modulation principle such as horizontally depleted p - n junction [147] and forward-biased diode [124].

Although MZI-based modulator always reported to achieve high modulation bandwidth and has been used as a practically component in optical interconnect [148]–[150], it still suffer from a large footprint. This is because, MZI-based modulator requires a long interaction length (\sim mm order) for a complete optical transmission. Due to the large footprint, MZI-based modulator suffers a high-power consumption.

On the other hand, resonance-based devices offer a smaller footprint such as silicon ring resonator [55], [145], [151]–[153]. The smaller footprint of silicon ring resonator modulator, offers a low power consumption. However, for resonance-based modulator is limited with the narrow bandwidth of the device compared to MZI-based modulator. Therefore, it is limited in terms of their application. Since resonance-based modulator normally uses ring resonator devices, there is another shortcoming that need to be carefully consider. The requirement of high sensitivity during the device fabrication process is essential for ring resonator because this can

affect the device operation performance. For example, the resonant frequency shifts in ring resonator, is achieved by every nanometres increased average width of the ring waveguide [154]. A high precision and sensitiveness of fabrication tolerance is required to achieve the right resonant wavelength. Therefore, this might be challenging to fabricate the device using CMOS processes.

PhC structures which is able to confine light stronger on the small mode volume, V , Si PhC nanocavity is another attractive candidate to demonstrate all-optical switching at low power [38], [155], [156]. Owing to the nano-fabrication process, PhC with the lowest loss has been demonstrated using two-dimensional silicon slab. Previously, Si PhC nanocavity with a $p-i-n$ diode has been reported to demonstrate an electro-optic (EO) modulation at a low operating power. Even though the device is all-Si type of modulator, it is unsuitable in terms of mass-production device. This is because, the device was fabricated using EB lithography and required an air-bridge structure to achieve a high- Q cavity. The essential of air-bridge structure in the device, is mechanically unstable and most importantly, the SiO₂-clad layer which ensure the stability and robustness of the device need to be sacrificed, and instead the device was cladded with an air-clad.

Hence, it is better to use the SiO₂-clad as it alternatively robust and fully compatible with monolithic integration [157]. So far, modulator that fabricated by photolithography fabrication process has been demonstrated by slow-light PhC waveguide [158], [159]. Cavity-based device which has a possibility to reduce the power consumption, have not been reported due to the difficulty to achieve high- Q factor with a SiO₂-clad structure [93].

Nevertheless, in 2015, PhC nanocavity has been reported able to exhibit high- Q factor ($\sim 10^5$) with a photolithography fabrication process with a SiO₂-clad [87] by employing a proper design of PhC structure. Since the device was fabricated with a basic Si photonic process, it allows an easy integration with $p-i-n$ diode.

Therefore, the motivation of this study is to demonstrate the electro-optic modulator using a PhC nanocavity integrated with $p-i-n$ diode fabricated by photolithography process and cladded with SiO₂-clad [160]. Since there is an existence of SiO₂-clad on the surface of the device and fabricated with photolithography process, the device is expected to have high stability and high degree of integration with other CMOS devices. In addition, due to the miniaturization of the device, lower power consumption is expected due to the high- Q and small V .

4.3 Spectrum characteristics

The spectrum characteristics of the device structure is measured. DC voltage and RF operation are conducted to evaluate the PhC nanocavity device as a modulator. The measurement setup is shown in Fig. 4.1 (a). The value of the Q factor of PhC structure that used in this measurement is 1.4×10^5 where the resonance wavelength occurred at 1587.27 nm. The measured of transmittance spectrum shows in the Fig. 4.1 (b).

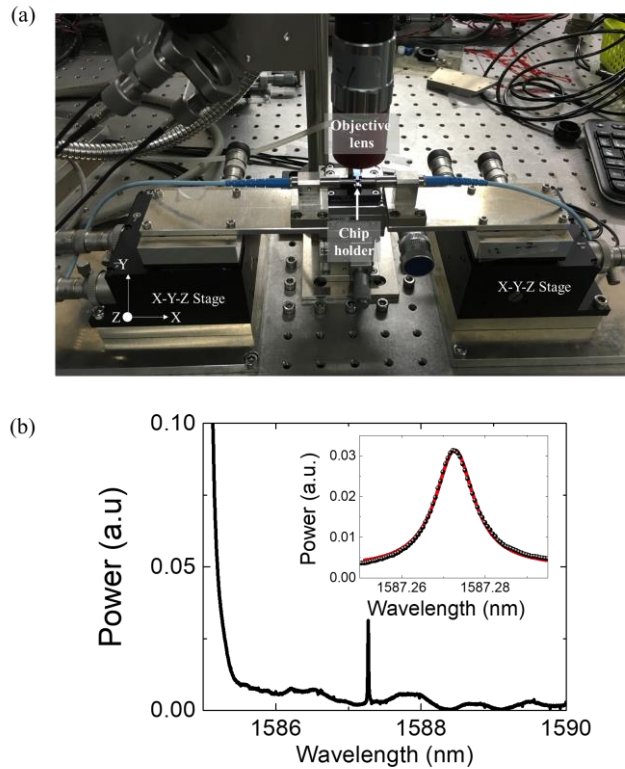


Fig. 4.1 (a) Measurement setup to measure the transmission spectrum. (b) The transmission spectrum of the PhC nanocavity. The inset shows the peak of the resonance cavity at 1587.27 nm wavelength and the loaded Q value is 1.4×10^5 .

4.3.1 DC voltage operation

The PhC nanocavity structure was embedded with the $p-i-n$ diode at the center of the. The $p-i-n$ diode was formed to allow an electrically control the injection of electrons and holes in the propagating light path. The p and n regions are connected with Al contact pads as a conductive part when voltage is applied. Hence, it is necessary to investigate the electrical conductivity between the diodes and the contact pads by measuring (direct-current) DC voltage operation. The operation is conducted by measuring the current-voltage (IV) of the $p-i-n$ structure. The reverse- and forward-biased of DC is applied to the Al pads. Results is shown in Fig. 4.2 (a) where it shows a good electrical conductivity between the Al contact pads and the $p-n$ regions structure.

Then, the CW laser is input into the structure while applying the RF signal in forward direction through the Al contact pad. This allowed carriers to be injected to the $p-i-n$ diode regions. The presence of the injection carriers will distort the crystal structure and resulting changes in optical properties of the device. Fig. 4.2 (b) shows resonance wavelength when different forward bias voltage is applied. The value of currents at different value of voltage are shown in the graph. The graph shows by injection of carriers to the structure, it changes the modulation of refractive index. As a result, wavelength of the resonance peak shifts when higher carrier's injection is injected to the structure.

From Fig. 4.2 (b), when the voltage is 1 V, the resonance wavelength starts to decrease significantly. This shows that clear resonance peak shift can be observed at 1 V where the value of current is 1.52 μA . This signifies that modulation of the resonance starts to appear at 1 V where it requires 1.52 μW of power consumption. At 1.2 V of voltage in which value of current is 2.76 μA , the resonance shift becomes greater than full-width at half maximum (FWHM) of the transmittance, large modulation of resonance peak can be observed. With the equation of $P = IV$, where P is power consumption value, I is value of current and V is applied voltage, power consumption during large modulation of the resonance peak can be calculated. The calculation value of power consumption of the device is 3.3 μW . This constitutes that PhC nanocavity device achieved a low power consumption. This is possible due to the good conductivity between Al contact pads and the $p-i-n$ regions. The size of the footprint too gives an advantage to the device to consume low power consumption. Compared to resonance-based modulator, this device shows smaller power consumption than silicon microring resonator [161].

Next, the graph in Fig. 4.2 (b) shows that with the increasing of carrier's injection, the intensity of transmitted light is reduced. This is because input light is being absorbed with high injection of carriers due to presence of free carrier absorption in the device. The wavelength of the resonance peak also shows a blue shift. This is due to the reduction of refractive index when more carriers are injected into the device. Normally, at higher injection of carriers, the device will generate significant heat resulting from the extraction of the carriers which is known as thermo-optic (TO) effect. At the $p-i-n$ regions, when forward bias current is applied, carriers which are pairs of electron and holes are injected to the i region. Since the junction is forward bias, the positive potential applied to p -region repels the holes, while negative potential applied to n -region repels the electrons. The change in potential between p -region and n -region decreases or switches sign. Increase of forward bias voltage, increases the motion energy of the carriers to move. This will lead to the increase of TO effect. TO effect then will shift the resonance wavelength to red shift.

However, graph in Fig. 4.2 (b) shows contradict. The resonance wavelength shift to blue shift where it indicates that there is no TO effect occur in the device. The reason of absence of TO effect is because the carrier plasma dispersion effect is more dominant and overcomes the TO effect. Based on Sorel and Bennett [44], the carrier-plasma dispersion effect decreases the TO effect. Therefore, the refractive index of the device's material is reduced and shifts the resonance peak wavelength to blue detuned. This proves that with carrier-dispersion effect it is possible to modulate the refractive index shift [55]. Plus, since the modulation occurs by carrier's injection, it is much faster compared to modulation by temperature dependence since heating a substrate is a time-consuming process. Thus, fast electro-optic modulation can be expected by carrier-dispersion effect.

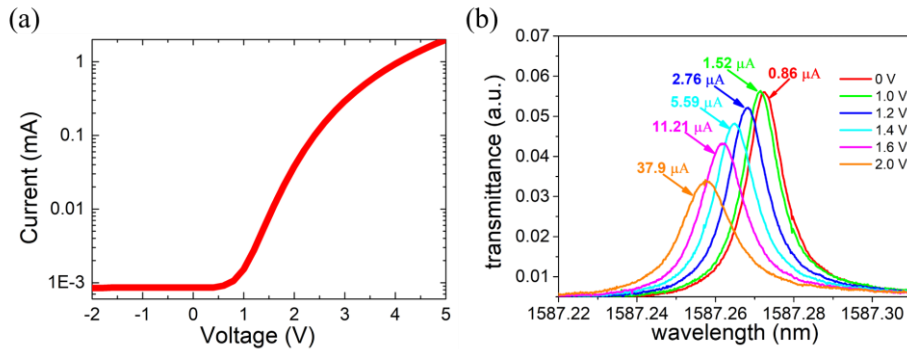


Fig. 4.2 (a) The relation of current-voltage when voltage range from -2 V to 5.0 V is applied. (b) Resonance wavelength when different forward bias voltage is applied.

The effect when more carrier's injection is injected into the device is observed by applying reverse- and forward-biased. Applied voltage in function of resonance wavelength is plotted as shown in Fig. 4.3. The figure can be divided into 3 different regions. Region I shows a reverse-biased voltage ($< 0\text{V}$), Region II is when a forward-biased voltage ranged from ($0 \leq V \leq 2$) is applied, Region III is when higher forward-biased voltage ($2\text{ V} >$) is applied to the device. Graph in Fig. 4.3 shows a very slight decrease which is almost insignificant in Region I because the applied voltage is reverse-biased voltage. The I-V graph of Fig. 4.2 (a) clearly shows a very small current in which almost no current flow during the reverse-biased voltage. Hence, negligible shift in resonance wavelength can be seen in Region I. Similarly, when forward-biased voltage lower than 1 V is applied, almost insignificant difference in resonant wavelength can be observed. Modulation of the resonance starts to appear clearly at the ranged of $1\text{V} \leq V \leq 2\text{ V}$ voltage is applied, where the resonance peak wavelength shifts to the shorter wavelength.

But, when the voltage is $2\text{ V} >$, the graph in Region III shows a dramatically change where the resonance wavelength begins to shift to the longer wavelength. This is because, when the applied voltage exceeds more than 2 V , not only more carriers is injected to the diode, but also the amount of heat increases and become more dominant, hence, the resonance wavelength shifted to the longer wavelength. So, it is obvious that the carrier-dispersion effect becomes ineffective and thermo-optic effect becomes superior. Thus, this shows that the range of operating voltage of the device for resonance modulation is from $0\text{V} \leq V \leq 2\text{ V}$.

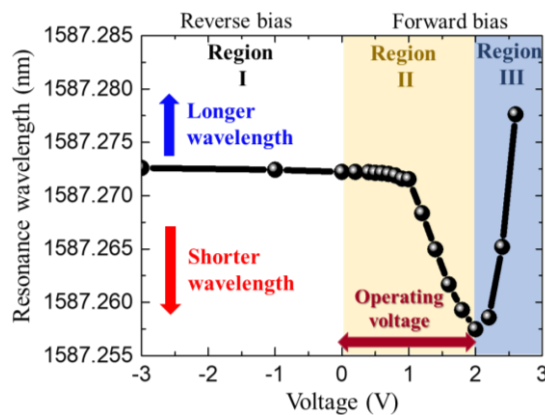


Fig. 4.3 Reverse- and forward-bias voltage is applied to the device

The capacitance value of the PhC nanocavity device is estimated by $C = \epsilon_{si} S/d$ where S is the area of the device which can be determined by $S = t \times w_w$. $d = w_i$ and ϵ_{si} is refer to the dielectric constant of Si. The estimated capacitance value is 5.88×10^{-18} F (5.88 aF). The capacitance value is relatively small due to the small size of the device structure which is impossible to achieve by MOS capacitor [162]. Therefore, if an AC power is used in the measurement, the power consumption should not be far from DC consumption. This makes the PhC nanocavity structure becomes an attractive device as a low-power operation is possible.

4.3.2 Radio-frequency (RF) operation

In order to observe the intrinsic carrier's extraction and recombination in the device, RF operation has been conducted by applying a square shaped of electrical signal pulse train voltage in time domain and measuring the transmittance spectrum. The setup of the operation is shown as Fig. 4.4 (a). 10 ns pulse width square shaped of electrical signal pulse train are generated by pulse pattern generator with an AC voltage. The voltage is set to $V \pm v$, where V is an offset voltage and v is an amplitude of modulation. The top and bottom of the square pulse is set at $\pm v$ to allow injections and extractions of carriers by time in the p - i - n diode. The laser sweep speed is 20 nm/s and sweep from the shorter wavelength to the longer wavelength.

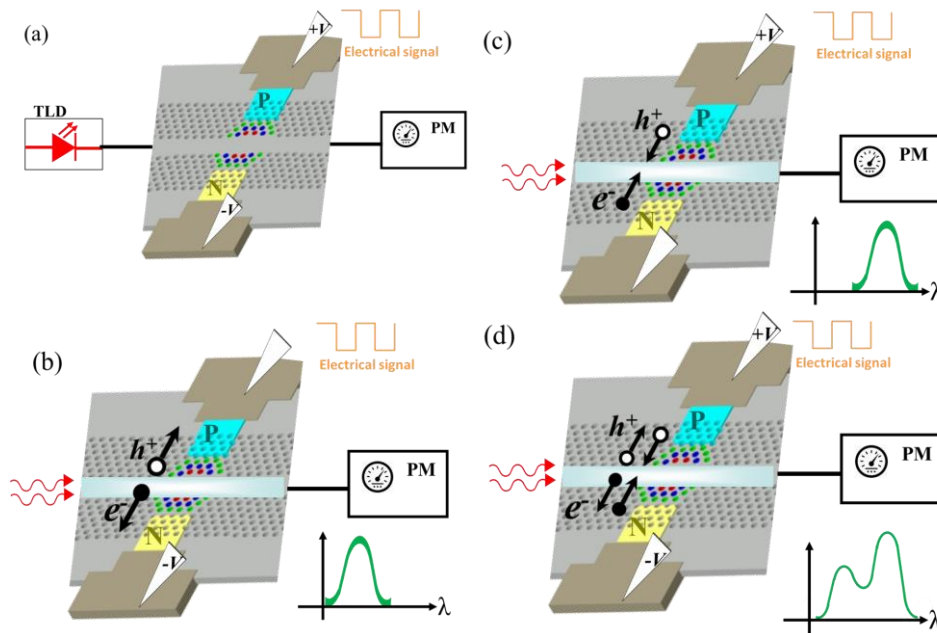


Fig. 4.4 (a) Measurement setup of RF operation. 10 ns square pulse of electrical signal is generated by PPG and applied to the device using RF probe. The top and bottom of square pulse is set at $\pm v$. (b) When $-v$ the junction becomes reversed bias. The holes and electrons are extracted towards opposite way and makes no changes to the resonance peak wavelength. (c) When $+v$ the junction becomes forward bias. The holes and electrons are recombined around the intrinsic region and their movements caused a significant heat. As a result, shift the resonance peak wavelength to longer wavelength. (d) Illustration when 10 ns of carriers' time is injected to the device. Half of the time, the junction becomes reverse-bias and carriers are extracted towards opposite. Another half of the time, the junction becomes forward-bias and carriers are recombined at the intrinsic region. The

resonance peak shows a split is due to the fast transition from the carriers' extraction to recombination.

Figs. 4.4 (b)-(c) describe the RF operation. Since the applied electrical signal is set to $\pm v$, the $p-i-n$ junction will become forward- and reverse- bias in time. Fig. 4.4 (b) illustrates the carriers' motion in reverse-bias junction. The holes and electrons are towards opposite direction and Fig. 4.4 (c) when the junction becomes forward-bias. Under forward-bias condition, a diffusion current flows of holes from p -region into n -region and electrons in the opposite way. The injected carriers, are reduced in number as they travel into the p - and n - regions by recombination mechanism. RF operation injected an electrical signal at $\pm v$ for 10 ns of time. Therefore, half of the time (5 ns), the carriers are injected to the intrinsic region and recombined at the intrinsic region, and the other half of the time, the carriers are extracted and towards opposite direction. The transition between carrier's extraction and recombination are fast as a result, caused the extraction of carriers through the electrode is inefficient and recombined around the intrinsic region. Therefore, transmittance of the resonance shows as Fig. 4.4 (d).

Fig. 4.5 shows the result of RF operation. The offset voltage is set to 0 V, 0.4 V, 0.6 V, 0.8 V and 0.9 V while the modulation amplitude is constantly 1.0 V and the carriers injection time is 10 ns. The result shows that the transmittance spectrum shifted to a longer wavelength as the voltage increased which might due to the dominant of the thermo-optic effect than carrier-dispersion effect. This can be explained by the carrier injection and extraction motion to the $p-i-n$ regions. The behaviour of the carriers is described as Fig. 4.4 (d). The recombination and extraction of carriers in a fast transition of time however, generate some amount of heat. Therefore, the thermo-optic effect becomes dominant and shifted the spectrum to the longer wavelength.

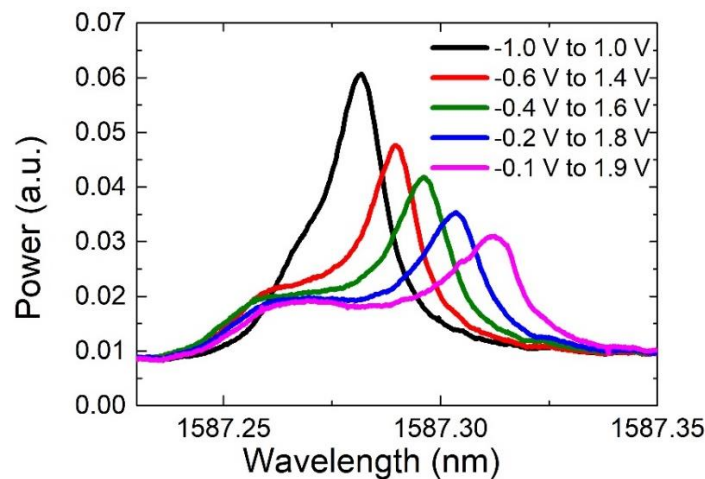


Fig. 4.5 Transmission spectrum when 10 ns of square pulse repetition rate is applied to the structure.

In addition, the transmittance spectrum shows a split near the resonance wavelength. This is due to the carriers' motion of to-and-fro caused by the carriers' injection and extraction at the $p-i-n$ region due to the $\pm v$ modulation amplitude as described in Fig. 4.4 (d). It should be noted

that the transmittance spectrum is measured by CW laser scan which is much slower compared to the carrier's injection time, thus, normally the transmittance spectrum becomes blurred. However, the resonance peak still can be observed which indicate that the device possible to operate in high speed operation.

4.4 Electro-optic (EO) modulations

Next, the EO modulation of the device is demonstrated. Fig. 4.6 shows the experimental setup. The optical signal is amplified using the EDFA and the noise is eliminated by the BPF. The output of the optical signal is observed by the oscilloscope. The modulation frequency is set from 100 MHz to 1.0 GHz. The square shaped pulses with an amplitude of 1.0 V and offset of 0.5 V were applied to the measurement.

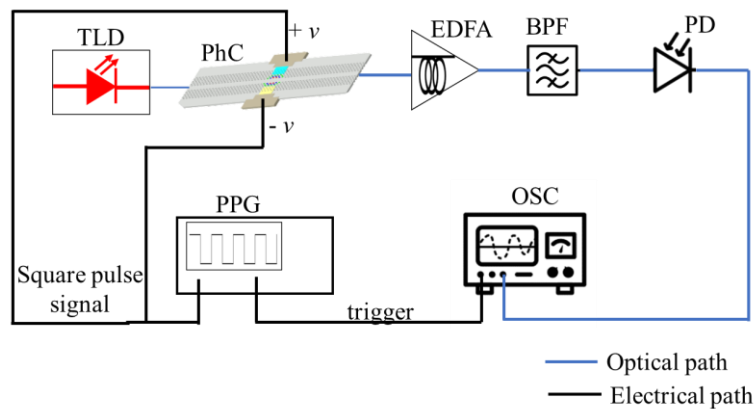


Fig. 4.6 Block diagram of the experimental setup. A square pulse wave is generated by PPG device.

The input laser wavelength is set at the resonance wavelength and off-resonance by detuning the wavelength to the shorter wavelength. Fig. 4.7 (a) shows a clear contrast of ON and OFF signal modulation at 0.5 GHz frequency. In order to calculate the modulation depth of the device, the input wavelength is detuned to achieve a maximum and minimum intensity of modulation signal for each modulation frequency. The calculation results are plotted in bode plot graph as shows in Fig. 4.7 (b) which represent the frequency response of the device. The modulation depth in the graph has been normalized from the maximum extinction ratio of 6.37 dB. It shows that the -3-dB cut-off frequency of the device is 0.35 GHz. The sudden drop of the modulation might due to the relatively large resistance of the device where the resistance value at 0.9 V is 0.85 M Ω .

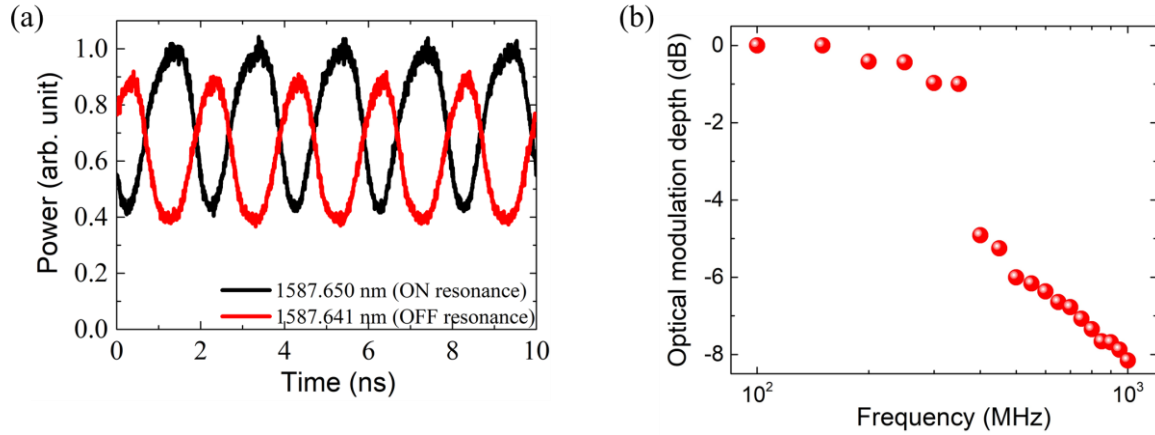


Fig. 4.7 (a) Modulated optical signal when 0.5 GHz modulation frequency is applied. The black and red line represent ON and OFF modulation when the input wavelength is set at the resonance and detune -0.01 nm away from the resonance, respectively. (b) Extinction ratio from 0.1 GHz to 1 GHz frequency.

4.5 Discussion

A resonant-structure-based modulator usually has a narrow wavelength band in which depending on the resonance modulation wavelength. This makes them tending to function over a relatively narrow wavelength range compared to MZI-based modulator and has a limited application. However, the narrow wavelength range mostly would be applicable for selective range modulation field which is commonly used in sensing application.

Unlike LiNbO₃ guided-wave-modulators, direct modulation of laser diode could not be designed for zero-chirp or adjustable-chirp operation. Zero-chirp and negative-chirp modulators usually will help guided-wave-modulators to minimize system degradation associated with fiber dispersion at a very high speed. However, since the PhC nanocavity modulator is resonant-based modulator and directly modulate the optical signal, zero-chirp operation could not be achieved.

The application of PhC nanocavity structure as an electro-optic device shown value of -3 dB cut-off frequency is 0.35 GHz. This indicate the device operates at a lower speed. The low speed performance seems to give the device a narrow application especially in high-speed requirement systems. Therefore, in order to understand the limiting factor of device operating speed, the carriers' transit-time and RC frequency response are examined theoretically.

The operating speed of device normally depend on the carrier diffusion behavior at intrinsic region [163]. Therefore, it is important to understand the carrier diffusion pattern at the intrinsic region. So, carriers' transit-time, t_{tr} is calculated. Based on equation of $v_s \times t_{tr} = d/2$, where v_s is electron velocity, t_{tr} is carriers' transit-time and d is intrinsic layer thicknesses. Note that, only electron transit-time is taken into account by assuming the holes transit-time is almost same as electron transit-time. In this calculation, the light phase velocity is ignored as it traverses the intrinsic layer and therefore a saturated velocity is assumed. The value of v_s is 7×10^6 cm/s [164]. Fig. 4.8 (a) illustrates movements of carriers in *p-i-n* junction during forward bias condition. Intrinsic layer, d is equal to width of the cavity, w_i which is 2.9 μm . The calculation value gives

$t_{is} = 20$ ps which is $f_{is} = 50$ GHz. Although in theory electron transit-time is fast, but, in reality, since the electron's travel towards n -side need to pass through triangular lattice array of air-holes in which is not directly straight-forward, as shown in Fig. 4.8 (b), this may reduce the transit-time value. However, the delay is assumed not so long since the device is small. Therefore, based on the calculation, carrier transit-time is not the limiting factor of the operation speed.

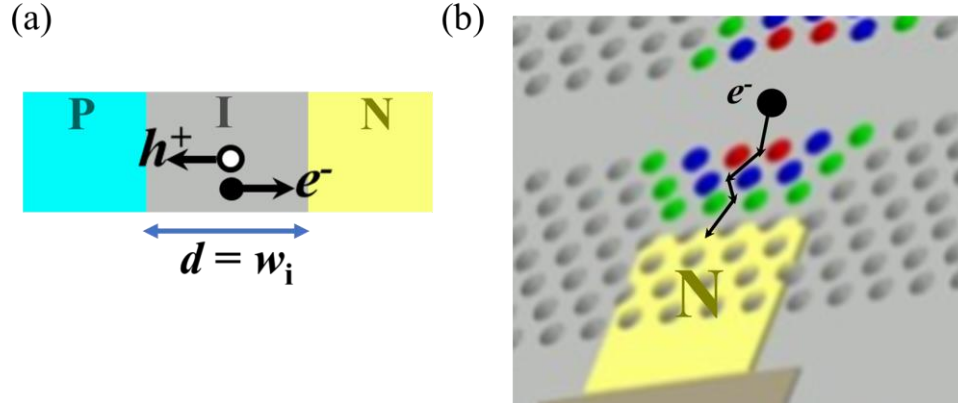


Fig. 4.8 (a) Movements of holes and electrons in the intrinsic layer. d is equal to intrinsic layer width. (b) Movements of electron to reach n -side.

Next, RC frequency response, f_{RC} of the device is calculated. Based on the capacitance, C value calculated on 4.3.1, which is $C = 5.88 \times 10^{-18}$ F (5.88 aF), frequency response, f_{RC} , $f_{RC} = 1 / (2\pi RC)$ is calculated. R is value of resistance measured from I-V curved measurement which value of 0.66 M Ω at 1.0 V. Based on estimation capacitance, C , value of $f_{RC} = 32$ GHz. Therefore, theoretically frequency response, f_{RC} also not the limiting factor. However, based on the -3dB cut-off frequency, bandwidth is 0.35 GHz in which estimation capacitance value is approximately 1.0 fF. Since parasitic capacitance is usually occurred in electronics circuit, there is high possibility that parasitic capacitance exists in this device. Due to the lack of instrument in our lab, the actual capacitance value of the device could not be measured.

However, if we could estimate the capacitance value based on the Al contact pad size, we obtained the value is approximately 8.0 fF which is comparable with estimation capacitance from -3 dB cut-off frequency. Therefore, to overcome this, the size of the Al contact pad should be smaller to reduce the parasitic capacitance.

Another factor that become the limitation of operating speed is high resistance value of the device. There are many possibilities that could contribute to the high resistance value of the device. However, the main reason is from the Al contact pads. Faith *et. al*, has investigated the effects of variations condition of contact deposition and alloying processes on contact between Al-Si-alloy metallization and n^+ and p^+ [165]. Clean deposition condition can reduce the resistance value of the contact. Therefore, one solution to reduce the high resistance value is through clean condition of contact deposition. Another solution to achieve low resistance is by employing a particular doping profile. Y. Terada *et. al*, has investigated that by optimizing the doping concentrations while maintaining the width of the p - and n -regions to avoid the absorption loss, the resistance of the device can be further reduced [166]. Thus, this will increase the bandwidth performance of the modulator 1.2 times. The optimization, is believed to further improve the electro-optic bandwidth up to GHz frequency [55], [153].

Even though the performance of metric in terms of bandwidth of this device is incomparable with MZI-based modulator, but in terms of foot print, PhC nanocavity device is superior than MZI-based modulator in which $50 \mu\text{m}^2$. Hence, the power consumption is much lower in which is at greater modulation of resonance at 1.2 V the power consumption is $2.76 \mu\text{W}$.

Although a previous study has reported a similar electro-optic modulator demonstration [61], the EB lithography fabrication process and with the presence of air-bridge structure makes the device in this study is more preferable for a future optical interconnect that has higher degree of integration which allows on-chip fabrication with CMOS electrical devices. Hence, high reproducible stability can be expected.

Table 1 shows the comparisons of performance between this device and other existing electro-optic devices.

Table 1. Comparisons of performance of modulators.

Structure	Device footprint	Speed achieved	Modulation voltage	Pwr. consumption	Fabrication & Integration
MZI [152]	Long	25 Gbit s⁻¹	1.75 V	High	Medium
Ring cavity [130]	Small	>12.5 Gbit s ⁻¹	3.5 V	Low	Difficult
PhC nanocavity (AB) [59]	Small	1 Gbit s ⁻¹	1 V	Low	Difficult
This work PhC nanocavity (SiO ₂) [146]	Small	1 Gbit s ⁻¹	1 V	Low	Ease

Although in terms of operating speed performance, this device slower compared to other silicon modulator which limiting the application of the device, however, this can be increased by reducing the resistance and parasitic capacitance value through clean deposition of contact pads and optimizing the doping concentration. By this, the device operating speed performance is believed possible to be further increased nearly to 5 ~ 10 GHz. The value would not be as high as MZI modulator; however, it is enough for an application of a silicon modulator. In addition, due to the compact size of the device, the fabrication cost can be far reduced. Furthermore, since it is fabricated with mature silicon foundry that compatible with CMOS process, make the device becomes easy in fabrication. Thus, the device is applicable for a compact signal sensing application device.

4.6 Summary

In this study, an electro-optic modulator is demonstrated using high- Q PhC nanocavity device. A forward-bias current is applied to the electrodes to modulate the refractive index by controlling the injection carriers' amount. This constitute an advance in PhC nanocavity technology. A sub-GHz modulation operation based on carrier plasma dispersion effect is successfully demonstrated. Thanks to the high- Q , enable a large optical modulation is achievable even though the refractive index modulation is small. The limiting factor of the operating band-width has been studied theoretically.

Chapter 5

PhC nanocavity photoreceiver

This chapter will describe utilization of high- Q PhC nanocavity structure as monolithically all-Si channel selective photoreceiver operation. The value of dark current of this device is achieved to be smaller (pA) due to the all-Si structure of the device. A minimum detectable optical power is also lower while the footprint is only $50 \mu\text{m}^2$. This allows the device to be applied as a compact monitoring device for optical network.

5.1 Introduction

Si photonics has become an attraction [167]–[169] due to the low operating power consumption [39], [124], [126], [170], [171] and its ability to integrate with other existing CMOS devices [172]–[174]. This is because Si has high refractive index and low-absorption loss make it as a potential for optical devices. Therefore, it constitutes an outstanding candidate to develop compact components for optical interconnect and ease combination with CMOS technology electronics. Among various devices of optical interconnect, electro-optic (EO) and optoelectronic (OE) devices are the key elements in optical interconnect when linking electrical circuits with photonics circuits.

Si devices used for EO operation works by introduction of plasma dispersion effect and had proven that it is an excellent material for optical modulation. Different with EO, OE operation

is more challenging due to the transparency of Si at telecom wavelength. As a result, photo carriers could not be generated and light could not be detected. Therefore, in terms of photodetection, researchers proposed that Si requires an integration with other optically absorbing materials to perform hybrid Si photoreceiver to enhance the performance of light detection. Several materials have been introduced to integrate with Si, such as, germanium (Ge), III-V layer bonded and graphene layer.

There are several figures of merit that are used to characterize a performance of photoreceiver, including its detection bandwidth, responsivity, bias operating voltage, dark current and footprint. Therefore, Ge on Si always received a lot of attention by large number of research groups due to the high-performance photodetectors which has high responsivity and high operating bandwidth [64], [175], [176].

However, the growth of high-quality Ge on Si has become the main challenge. A lattice mismatch between Si and Ge will cause surface roughness which led to the slowdown of Ge devices integrated with CMOS Si electronics devices. The other challenge is high density of threading dislocations in Ge epitaxial layer which will affect the performance of Ge devices.

The other proposed material to overcome the weakness of Si as detector in telecom wavelength is layered by two-dimensional materials such as graphene. The material is deposited on the SOI waveguide [177], [178]. Though the graphene layer shows significant interaction with CMOS compatible silicon waveguide and can be conducted in room temperature, it produces large dark (leak) current that will lead to high of applied bias required because of lack of a bandgap in graphene.

In addition, those introduced hybrid methods will not be adequate in future for fast-developing optical chip-level integration which pursue for miniaturization in size, low fabrication cost and simplicity in package [179], [180]. Therefore, for the development of integrated photonics in long term, researches are currently start to considering all-Si photodetection devices [181]–[183].

5.2 Motivation

All-Si photodetection devices has been conducted by several ways such as ion-implantation technique, utilization of silicon ring resonator, MZI-based photoreceiver and two-photon absorption based photoreceiver. Ion-implantation has been expanded widely after Fan reported that optical absorption can be obtained when Si is damaged by the radiation and photocurrent is achieved [184]. These than has open a path that all-Si photoreceiver is possible through ion-implantation technique. Many study has been conducted regarding the technique to improve the detection performance [181], [185]–[187]. However, the complexity of the fabrication makes the techniques becomes challenging to integrate with other CMOS devices. Plus, with the presence of defects, increase the dark current values.

Since two-dimension of PhC devices allowed strong light confinement, and has allowed researchers to devise small wavelength multiplexing devices [188]–[190], all-optical switches [34], [191] and ultra-small electro-optic devices [61], [152]. Those are based on high- Q PhC nanocavity [30], [36]. Although researchers usually claimed that PhC devices are compatible with CMOS technology, several challenges should be overcome if the integration of Si photonic devices with other devices to be reality. Generally, PhC devices requires high-precision of

fabrication process which is different from current Si photonics fabrication devices that allows integration of CMOS. That is not all, to fabricate high- Q nanocavity, an air-bridge structures are required which is different with from others normal Si photonic devices that are cladded with SiO₂-clad. Therefore, PhC devices mostly are irreconcilable with Si photonic devices due to the fabrication technique and structure.

Thanks to the employment of two-photon absorption (TPA), the photodetection responsivity can be obtained with PhC device structure. Previously, OE operation have been demonstrated with general air-bridge structure [78]. Although it is reported to achieve low dark current and significantly high quantum efficiency, it is not a CMOS compatible device. Plus, the air-bridge structure not only makes the fabrication complex, but also suffered the SiO₂-clad make the device is fragile and unstable.

To overcome these problems, recently by employing a proper design structure, a high- Q SiO₂-clad PhC nanocavity fabricated by photolithography technology has been reported which exhibits an ultrahigh- Q of higher than $\sim 10^5$ [87]. Since the device that used in this study has same fabrication process as reported in [87], which is the basic Si photonics process, it allows the easy integration of heaters [117] and $p-i-n$ diodes [120], [160] and this offers the possibility of adding various functionalities to the device. Hence, all-Si photoreceiver with a SiO₂-clad structure is possible to demonstrate a full CMOS compatibility device.

5.3 Photoreceiver properties

5.3.1 Dark current

Dark current also known as a leakage current which is generated when no radiation is radiated to the detector at the diode's reverse voltage. This is due to the random generation of electrons and holes that exists within the depletion region of the device. Large number of dark current will produce large noise to the device, thus, it is kept to be as minimum as possible. That is not all, the low number of dark current will allow low bias voltage of the device.

A photoreceiver usually works with a reverse-biased voltage, therefore, the generation of dark current is common. To measure the dark current of the PhC nanocavity device, a reverse-biased voltage is applied from 0 to -5 V, at room temperature. To make sure there is no radiation of light source, the measurement is done in a dark room. Commonly, the value of dark current is too small, hence, a transimpedance amplifier is used to amplify the dark current value. Two different samples with different barrier length, d parameter is measured.

Result is shown in Fig. 5.1. The dark current values range of -3 V is measured to be 38 pA and 59 pA for sample A and sample B, respectively. This shows that the dark current for the device is much lower than those reported of germanium [192]–[195] and ion-implanted [196], [197] photoreceiver, which is usually of μ A to nA order. The smaller dark current value is possible to obtain with the PhC nanocavity device because the device did not rely on a regrowth or implantation process, which may cause a defect in the structure.

The low number of dark current (\sim pA order) indicates that the noise in the detector is less and the bias voltage is low of the PhC nanocavity device. This constitutes as the main advantage of the device.

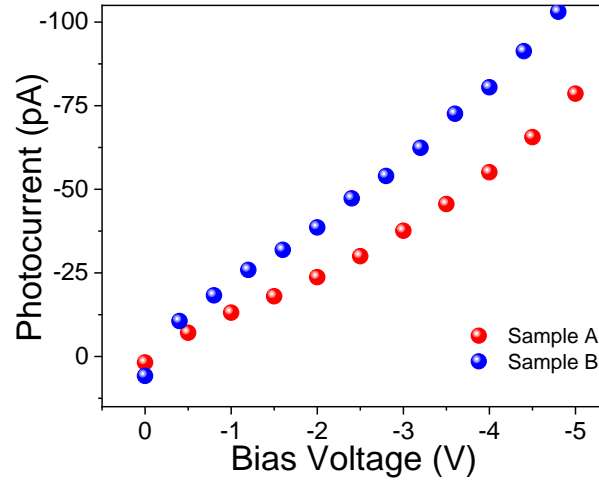


Fig. 5.1 Dark current at room temperature for sample A (red dots) and sample B (blue dots) when the bias voltage ranged from 0 V to -5 V. The barrier length, d for sample A and B are 18 and 9, respectively. The small current difference is due to the different parameters between the devices.

5.3.2 Transmission spectrum and photocurrent

In order to understand relation between transmittance spectrum and photocurrent at telecom wavelength range of the device, wavelength in relation to transmission-photocurrent is measured. The measurement is conducted by injecting CW laser light and -3 V reverse-biased voltage is applied to the device. The transmittance spectrum and the generated photocurrent is measured simultaneously. Note that the value of input power, P_{in} is the value of the light intensity before coupled to the cavity.

The transmittance spectrum and photocurrent as a function of wavelength at input $P_{in} = 10 \mu\text{W}$, which is close to the detection limit, is shown in Fig. 5.2 (a). Photocurrent is generated at its maximum value at the peak of the cavity resonance is observed. This shows directly that the cavity resonance of the device structure enhances the generation of the photocurrent.

Fig. 5.2 (b) and (c) show the transmitted optical spectrum and photocurrent at different P_{in} values. The value of the generated photocurrent and transmittance spectrum are recorded simultaneously. The nonlinear modulation is clearly shown in Fig. 5.2 (b) as the increased of P_{in} , which is a consequence of the thermo-optic bistability effect. The thermo-optic bistability effect is induced by the TPA, clearly shows a clear sign of optical bistability, which only occurs when the light is strongly confined in the small area [170], [198], [199]. This results from the relaxation of the carriers turning into heat, which was generated by the TPA. Thanks to the TPA, it makes the energy of the photon to be at least equal to the bandgap energy, E_g of the PhC material to excite an electron from the valence band to the conduction band. This then generate the photocurrent of the device. At the same time, a similar shape to that in Fig. 5.2 (c) is detected where the maximum photocurrent value is at the resonance cavity.

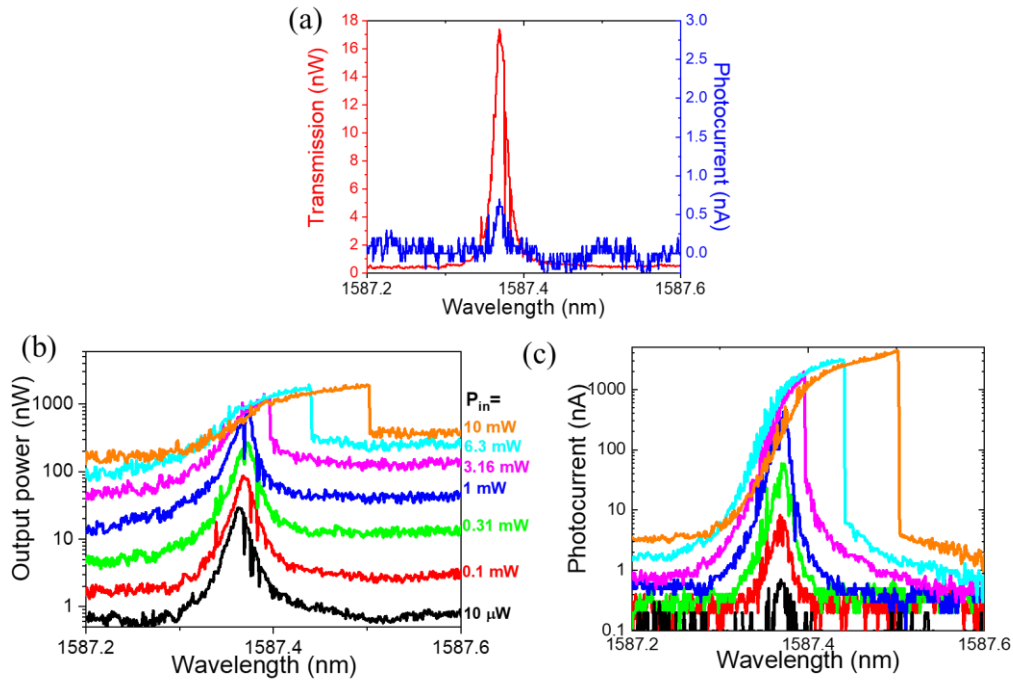


Fig. 5.2 (a) Transmission spectrum and photocurrent at 10 μ W input power as a function of the input light wavelength. (b, c) Transmission spectrum (b) and photocurrent (c) at various input powers when reverse -3 V is applied to the device.

5.3.3 Responsivity

Next, in order to show the relationship between the input power and the photocurrent of Fig. 5.2 (b) and (c), the peak of photocurrent in Fig. 5.2 (c) as a function of P_{in} has been plotted in Fig. 5.3.

Based on the plotted graph shown in Fig. 5.3, there is a linear increase when the input power is between 10^{-6} W and 10^{-4} W. This is due to the presence of the one-photon absorption that is inherent in Si device, where the linear sensitivity is 13.4 mA/W. As the power increased, the photocurrent increased non-linearly. This is because of the TPA, and the non-linear carrier formation is noticeable at a 10^{-5} W input power. However, the sensitivity then saturates owing to the free-carrier absorption loss that occur when the input power exceeds more than 10^{-4} W. Since the device is a non-linear detector device, the quantum efficiency is dependent on the input power, P_{in} . hence, at the optimized of input power, $P_{in} = 0.3$ mW, a maximum quantum efficiency of 0.89 % is obtained. Although the value appears to be unremarkable, a careful evaluation will show that the detector device has sufficient sensitivity for applications.

Although the quantum efficiency value is usually the figure-of-merit (FOM) of a photoreceiver device, the minimum detectable power could be an argument of FOM for the photonic OE device when CMOS devices are integrated on a same chip. First, an all-Si detector is superior to other devices, because the dark current is low, which allows us to detect a very weak signal light. Although the quantum efficiency appears to be low, and the sensitivity in the low power regime is only 13.4 mA/W, the minimum detectable power is very small which is at 10 μ W (-20 dBm) due to the small value of the dark current which is 36 pA. This is the key to achieve

the detection of very weak optical signal. Secondly, due to the small size of the device, the estimated capacitance is 5.9×10^{-18} F [160]. The small value makes it possible to drive the adjacent CMOS devices without using costly and noisy trans-impedance amplifier. As a result, of these two characteristics – low noise and small capacitance, the PhC nanocavity device has a potential to directly feed the signal into adjacent integrated CMOS devices. The low power of detection ability of the device, together with its wavelength selectivity will open variety of applications including in-line monitoring at various optical network components.

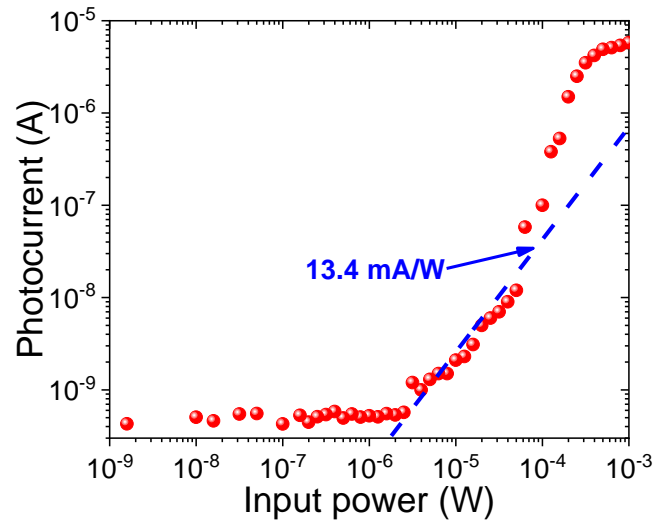


Fig. 5.3 The red dots show the photocurrent at different input powers on cavity resonance wavelength. The dotted blue line shows the calculated responsivity of the device.

If the achievement of the device is evaluate carefully to compare with previously reported studies [78], the merit of device that used in this study, is its capability to detect a low power, thanks to the small dark current. The fabrication of the device also helps the device to integrate easily with silicon photonic devices. For example, the SiO_2 -clad device is easy to integrate with spot size converter, which is difficult to accomplish with an air-bridge structure PhC devices. As a result, the loss at the coupled fiber is -1.6 dB, which is in far lower overall loss compared to devices reported in previous studies [78].

5.4 Photoreceiver operation

Then, the demonstration of photoreceiver operation is conducted by inputting a square optical signal to measure the dynamic response of the photoreceiver. System configuration of the measurement is shown in Fig. 5.4 (a). As a proof-of-principle experiment, a trans-impedance amplifier is used to amplify the output signal with a gain of 5×10^3 V/A. A square pulse signal is injected to the device structure, which has an amplitude of 0.5 mW at the resonance cavity. The result is shown in Fig. 5.4 (b).

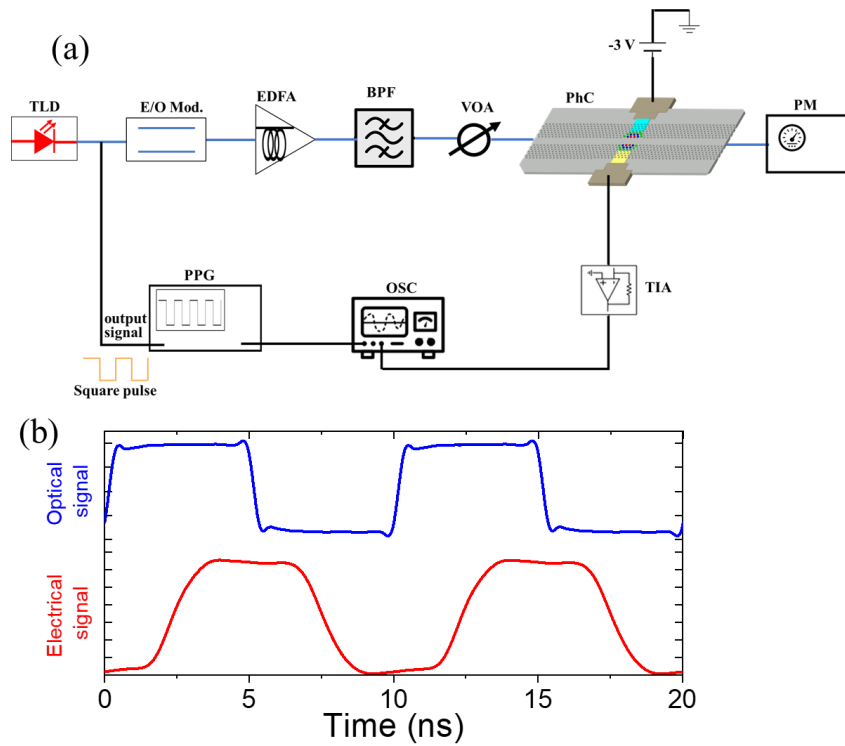


Fig. 5.4 (a) Measurement setup for 0.1-GHz photoreceiver operation. (b). The blue line shows the square pulse waveform of the optical signal input into the PhC nanocavity device. The red line shows the output electrical signal waveform at the resonance cavity.

Then, the extinction ratio from the modulation depth of each frequency from 100 MHz to 300 MHz are plotted. The result is shown in Fig. 5.5. The -3 dB cut-off frequency of the PhC nanocavity device is obtained at 0.15 GHz.

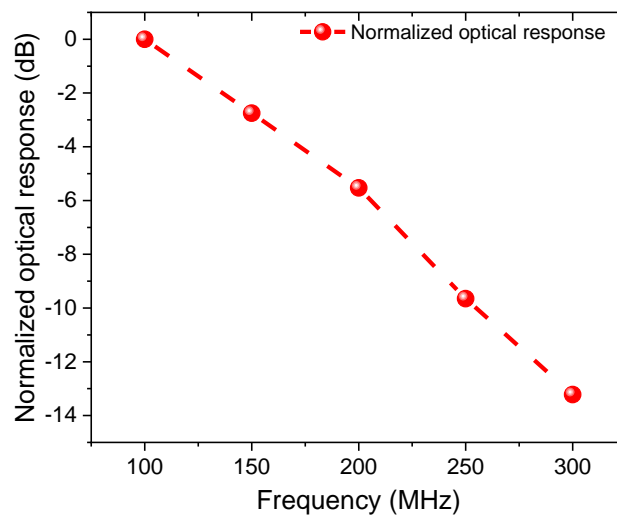


Fig. 5.5 Normalized modulation depth from 100 MHz to 300 MHz.

Finally, the 2^8-1 bit of pseudo-random non-RZ bit sequence signal waveforms at 0.1 Gbs^{-1} is injected to the device structure as shown in Fig. 5.6. The red line indicates the output electrical signal when the signal waveforms is at the resonance wavelength. However, when the wavelength is detuned to -0.01 nm away from the resonance cavity, there is no output electrical signal able to be detected by the detector, which has been indicated as blue line in Fig. 5.6. Therefore, this indicates that the device only can detect fixed wavelength (resonance wavelength). So, the PhC nanocavity device is a wavelength dependence photoreceiver which means we can detect single wavelength channel without wavelength division multiplexing (WDM) filter.

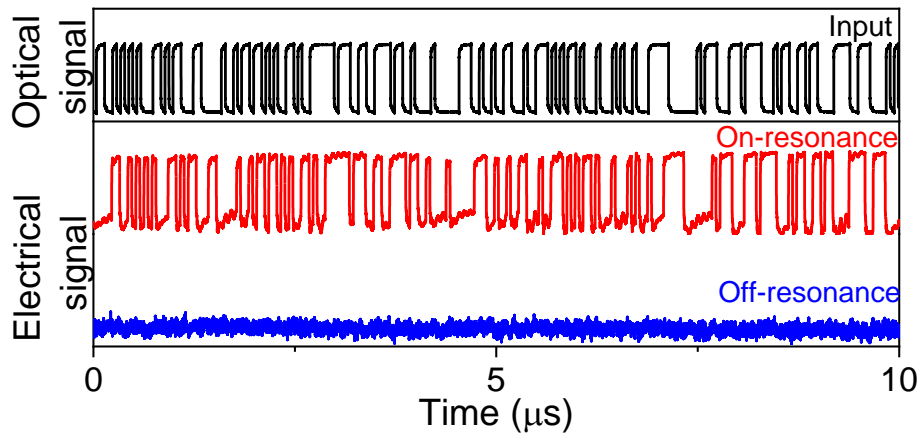


Fig. 5.6 0.1 Gb/s photoreceiver operation demonstration. The black waveform is the input optical signal, which is a 2^8-1 pattern length of pseudorandom binary sequence. The red waveform is the output electrical signal when the input signal is at the resonance of cavity. The amplitude of the electrical output is $\sim 6 \mu\text{A}$ ($\sim 0.03 \text{ V}$). The blue waveform is the output electrical signal when the input signal wavelength is detuned to 0.1 nm wavelength.

5.5 Discussion

Although the device obtained a very low dark current value, the operation speed of the device at -3 dB cut-off frequency is 0.15 GHz which determine slow speed. The limiting factor of the speed as discussed in Chapter 4, is due to the presence of parasitic capacitance and high resistance value. Since parasitic capacitance is usually occurred in electronics circuit and could not be eliminated, the value should be reduced. This can be realized by optimizing the size of Al contact pad in the device.

Next, the high capacitance value of the device can be reduced by conducting the deposition of the contact pad in a clean condition [165]. This can reduce the resistance value two times order. Another solution to reduce the capacitance value is by optimizing the doping concentration of the ions (p^+ and n^+) [166]. Another possible solution to increase the operating speed of the device is by integrating the trans-impedance amplifier (TIA) on the device. However, this will not increase the responsivity of the photoreceiver.

In order to increase the responsivity of the photoreceiver, removal of oxide (O_2) passivation through etching process is needed. This is because the PhC nanocavity device that used in this study is cladded with SiO_2 -clad which will generate fixed positive oxide charges close to the interface. The oxide passivation then will reduce the interface state density, thus, reduce the

responsivity of the device. This led the device to have lower quantum efficiency. Previously, similar work based on air-cladded PhC device has been done and achieved a high responsivity and quantum efficiency [200] due to the absence of fixed positive oxide charges at the surface. Therefore, in order to enhance the responsivity and quantum efficiency value, the oxide passivation should be removed.

Table 5.1 shows the comparison between hybrid and all-Si photoreceivers. Although in terms of quantum efficiency, all-Si photoreceiver need to be further improved, but the value of dark current in all-Si PhC shows relatively small. This is because the entire device is made by all-Si. So, it is not suffered from any defects for epitaxial growth, layered deposition or ion implantation. This makes the device superior than others. That is not all, all-Si PhC also offers a small device length, so the insertion loss of the device onto electrical circuits or other components is expected to be small.

The low dark current of all-Si PhC, makes the device becomes very sensitive to power detection. The minimum detectable power is at $10 \mu\text{W}$ which allow the device possible for power monitoring application. In addition, the device is fabricated by mature basic silicon foundry which allows an easy integration of spot size converter at the facet of the input and output of the device. This allows the coupling loss at the facet of the device with fiber as low as -1.6 dB . The coupling loss is 80 % lower compared to previous device which has been fabricated with EB lithography process. Furthermore, the most importantly, the fabrication process allows an integration with other CMOS electrical devices. By this, the optical device and electrical device can be integrated monolithically.

It also achieved a high- Q ($\sim 10^5$) without an air-bridging process which makes the device mechanically stable. This constitutes that Si PhC with SiO_2 -clad can open a path of higher density of integration, compact in size and simple fabrication process of all-Si photoreceiver. This then will lead to a reduction of device fabrication cost. Therefore, these advantages make the device possible for an application of monitoring system such as a compact and cost-effective fiber monitoring system that is needed to ensure the quality of optical networks.

Table 5.1. Comparison between hybrid and all-Si photodetectors.

Material	Hybrid		All-Silicon		
	III-V/Si [180]	Ge/Si [181]	Si ⁺ /Si [66]	Si PhC (AB) [182]	Si PhC (SiO_2) [78] This work
Quantum efficiency	~90 %	~93 %	~16 %	9.7 %	0.89%
Dark current	~140 nA	169 nA	0.5 nA	15 pA	37.6 pA
Min. detectable input power	~0.45 μW	~190 nW	~2.5 nW	0.9 nW	10 μW
Coupling with fiber	NA	NA	NA	-12 dB	-1.6 dB
Operation voltage	-3 V	-2 V	-5 V	-3 V	-3 V
Device length	400 μm	50 μm	3~4 mm	8.4 μm	8.4 μm
Fabrication & Packaging	Complex	Complex	Medium	Medium	Ease
Integration level	Medium	Medium	Large	Medium	Large

5.6 Summary

As a conclusion, due to the good crystal property which has been obtained by a high- Q PhC nanocavity photolithography fabrication with SiO₂-clad, a low dark current is achievable. The sub-GHz dynamic response of the photoreceiver has been demonstrated and successfully shows that the device is a wavelength-selective photoreceiver. This will enhance the Si PhC nanocavity technology as it allows the integration of a photonic circuit with other CMOS electrical circuit as a monolithic scheme.

Chapter 6

All-Si scheme PhC nanocavity transmission link

A passive and active optical device has been demonstrated with high- Q SiO₂-clad PhC nanocavity fabricated with photolithography such as electro-optic modulator, photoreceiver and demultiplexer filter. In this chapter, the demonstration of all-Si scheme CMOS compatible transmitter and receiver is described. The PhC nanocavity will modulate the signal and will be detected by PhC randomness structure. Both back-to-back and 5 m transmission link is demonstrated with modulation of 50 MHz square pulse signal and 2^5-1 PRBS NRZ signal.

6.1 Introduction

Over 30 years ago, Moore has predicted that there will be an increasement of transistor in electrical circuits which has become a reality nowadays [201], [202]. In 2017, the largest number of transistors in a single chip processor is 19.2 billion. Therefore, more power is needed to carry data. This has driven an urgency to downscale in feature sizes especially in the short distance region communication. That is not all, electrical signal over copper cables also has begins to show its limitation due to the amount of resistance in copper wire which will distorts the transmitted signal [203].

Optical signals have been well established for efficient data transfer from a long distance to very short distance (rack-to-rack). Due to the unique characteristics of Si, which are high refractive index and low absorption loss at telecom wavelength, makes Si is one of the best candidates to be developed. Si photonics devices has become one of the attraction due to the CMOS compatible and many highly performance devices have already been demonstrated [75], [174], [204], [205]. Plus, with the high refractive index and low loss absorption at telecom wavelengths, makes the Si photonics is possible to realize low-loss waveguides on chip due to the mature of fabrication technologies [206]–[208]. Hence, combination of silicon photonics devices with electrical circuits on a single chip have become possible due to the ease of integration. Therefore, the next step of integrated Si photonics device is towards intra-chip (chip-to-chip) data processing. It requires a nanoscale circuits, optical sources, transmitter and detectors.

On the other hand, photonic crystal nanostructure device adds unique capabilities as they offer extremely tight light confinement due to the small mode volume and high- Q . Therefore, it is possible to enhance nonlinear effects for μW power levels and modulators with very low switching energy [22], [34], [209]. Among those devices, electro-optic (EO) and opto-electronic (OE) devices are the key elements when linking electrical circuits and photonics circuits. However, since it requires a nanoscale circuits, it is necessary to have a miniaturization in size, ease in fabrication and cost-effective devices, thus, the interfaces of bridging the EO and OE devices as a transceiver has drawn an attention for a fully functional optical interconnect system.

6.2 Challenges and motivation

However, in order to successfully obtained fully functional a monolithic (all-Si scheme) transmitter and receiver, a few challenges need to consider. Firstly, since the device that is used in this study is PhC nanocavity structure, so it is cavity resonant based device. Cavity resonant based modulators function over a narrow band compared to common optical modulator such as MZI-based devices. Therefore, this will limit their applications. But the main shortcoming is the high sensitivity in fabrication tolerance that can significantly affect the device operation performance. For example, the ring-modulator resonance shifts, which has been demonstrated as a high compact resonator [55], is depending on the width of the ring waveguide [154]. Therefore, the fabrication technique should be high of precision to achieve the right resonant wavelength. This might be challenging to achieve using the CMOS compatible process.

Secondly, silicon is transparency at the telecom wavelength, thus, photocarriers could not be generated. This caused all-silicon made devices is not an efficient for a detector. As a result, combination of silicon with other material is essential through epitaxial growth, ion-implantation or layer with other materials. These in turns, relatively produce high dark current caused by the defects that may appear in the structure.

Therefore, commercial Si photonics transmitter and receiver currently utilized MZI-based modulator together with epitaxial grown silicon or heterogeneously bonded III-V photodetectors [81], [82], [180]. Those has recorded a high performance of transmitter and receiver in terms of bandwidth. However, although in present these methods are effective, but in future fast developing optical chip-level of integration that requires compact in size, low fabrication cost and simplicity of package, these methods will become inadequate.

For that reasons, researchers are start to consider all-silicon transmitter and receiver devices and on the same time try to overcome their limitations. Recently, a group of researchers from Fujikura laboratory, Japan has reported of all-Si scheme by MZI structure for both part of modulator and receiver [85]. They obtained a high-speed detection in avalanche gain region as high as 28 Gb/s which is successfully works up to 20-km optical fiber transmission link. However, the study shows that the value of the dark current is relatively high which is 4.1 nA at -3 V bias voltage with a large power consumption of 765 mW. In addition, the foot-print of the system itself is large due to the long interaction length (\sim mm orders) is required for a complete transition.

Therefore, the motivation in this study is to demonstrate all-Si scheme that is compatible with CMOS devices at low power consumption and small dark current. In this study, PhC nanocavity is used, so it does not require a high precision in terms of fabrication as silicon ring waveguide. As previous study has reported that the PhC nanocavity able to achieve an ultrahigh- Q ($\sim 10^5$) cavity with SiO₂-clad through the sophisticated of photolithography fabrication process [87]. Plus, as it is fabricated with basic Si photonics process, easy integration of heaters [117] and *p-i-n* diode [88], [89] are allowed and offer the possibility of various functionalities to this device. Owing, to the compactness of the device, it is good for use as a cost-effective power monitoring device.

In this study, first the characteristics of the EO (Tx) modulator and OE (Rx) receiver performance of the device is study. Next, towards the transmitter and receiver transmission link operation, both of the Tx and Rx cavity resonance need to be matched. Therefore, temperature dependence operation is conducted. Finally, the transceiver operation is demonstrated and the obtained results will be discussed.

6.3 Electro-optic modulator performance

Note that it is basically the same device that has been demonstrated in the electro-optic (EO) modulator based on photolithography fabrication [160].

First, the nonlinear behaviour in the ultrahigh- Q cavity is revealed. A nonlinear operation is conducted where the resonance peak is injected with different input powers, P_{in} and the laser is swept from short wavelength to the long wavelength. Fig. 6.1 shows a clear asymmetric transmittance spectrum when P_{in} is more than 1.0 mW. This is due to the thermo-optic bistability results from the carrier generation by TPA in Si [210]. Therefore, to avoid the presence of TO effect which may affect the system, P_{in} is kept as low as possible.

Next, the EO modulation demonstration is performed as shown in Fig. 6.2. The input CW laser is modulated at the resonance cavity with 100 MHz square pulse train of electrical signal. The P_{in} is set to 50 μ W. Clear ON to OFF contrast waveforms can be detected when the input wavelength is at the resonance and detune -0.06 nm apart from resonance. Note that same demonstration using same device has been demonstrated before [88], and higher frequency modulation speed of 0.5 GHz is possible.

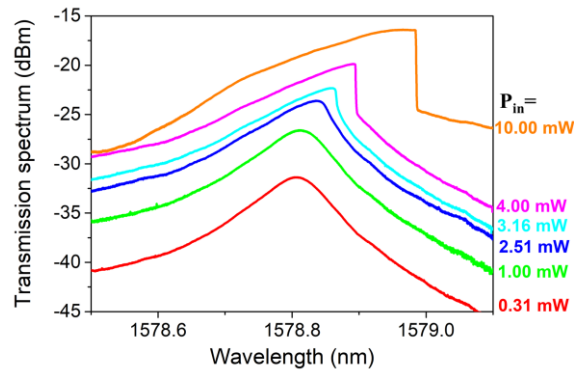


Fig. 6.1 TO effect at different input laser, P_{in} . The transmittance spectrum starts to show the asymmetric when P_{in} is 2.5 mW.

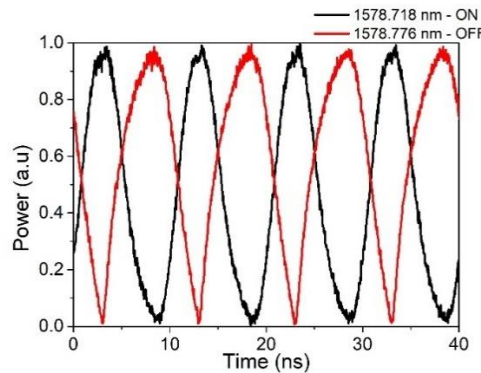


Fig. 6.2 EO modulation at 0.1 GHz. It shows clear contrast between ON and OFF modulation. The black line represents when wavelength is at the resonance of cavity and red line represents when the wavelength is detuned -0.06 nm away from the cavity

6.4 Opto-electric receiver performance

Then, the performance of the opto-electric (OE) component is evaluated. However, the device component structure is different compared to the EO component. Therefore, in this section, firstly the device design structure is described, then, the basic characteristics of the device is studied and finally a demonstration of OE receiver is conducted by the device.

6.4.1 Basic design structure

The PhC structure is normally fabricated using EB lithography where the holes are precisely patterns on the PhC slab. However, there is a possibility of holes disorder to occur due to the error during the fabrication process. As a result, this may disturb the usual performance of the PhC structure. For example, if the wavelength is at the mode-gap area of the PhC structure, the number of group velocity is small. But this will be differed if there is a fabrication error which may disorder the structure. Therefore, realizing the importance to understand the effect of disorder to PhC structure, numbers of researched has been done [211]–[215].

The structure of the device is illustrated in Fig. 6.3(a). It contains a PhC waveguides (PhC-WG) which is W0.98 sandwiched by W1.05 PhC-WG. Theoretically, the designed structure W0.98 has a smaller waveguide compared to W1.05, the mode-gap frequency of W0.98 is supposedly higher than W1.05 so, the input light will reflect at the edge of W0.98 waveguide and will not transmit to the other side of W1.05 which is the frequency below the W0.98 mode-gap as illustrated in Fig. 6.3 (b). However, in this study, due to the disorder of which caused to the frequency fluctuation at the mode-gap where light can propagate through the W0.98 waveguide and there is a possibility where the light frequency closed to the mode-gap W0.98, thus, reached the output and light confinement only occurs at W0.98 waveguide as illustrated in Fig. 6.3 (c). the fluctuations at W1.05 waveguide will not give any influence to the transmittance spectrum because the mode-gap frequency is less than W0.98.

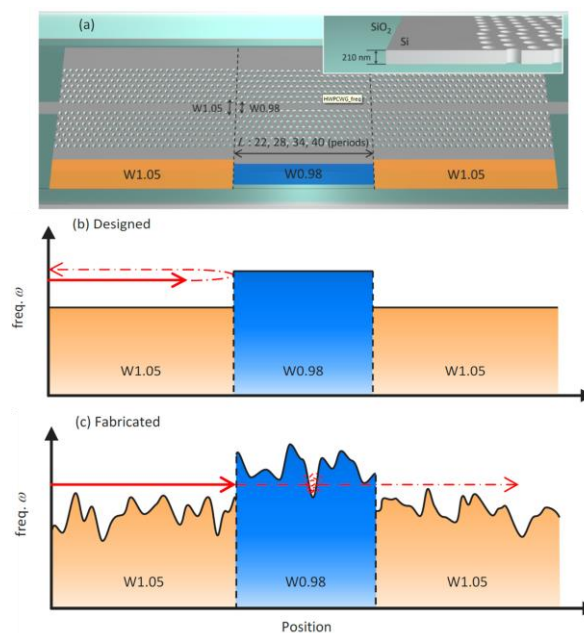


Fig.6.3 (a) Design structure of two-dimensional PhC-WG, which consists of W0.98 waveguide sandwiched by W1.05 waveguides. The silicon slab is cladded with SiO₂-clad. (b) Theoretically design structure. (c) Fabricated design structure that contains a disorder. [Reprinted with permission from Y.Ooka, *et al.*, Opt. Express, **24** (10), 2015]

The disorder happens to be in the PhC waveguide is due to the fabrication error during the fabrication process. The device is fabricated using a photolithography technique that has a low spatial resolution compared to the ordinary fabrication technique used to fabricate PhC waveguide structure which is EB lithography, thus, led to the few fabrication errors. However, the photolithography fabrication technique is suitable for mass production. In addition, the SiO₂-clad ensure the stability and robustness of the device.

Fig. 6.4 (b) shows the transmittance spectrum of the PhC-WG structure. It shows a clear peak resonance at 1579.6 nm wavelength which indicates that light is absolutely confined in the area. The light confinement occurs at the W0.98 waveguide as illustrated in Fig. 6.3 (c). Considering that the light confinement can be restricted at W0.98 waveguide through proper

design, a *p-i-n* diode is integrated on the PhC-WG structure to allow an electrically control the injection of electrons and holes in light propagation path. Since the fabrication of the device uses well developed silicon photonics technologies, the *p-n* doping and integration with high transmittance spot-size converters are both possible. The fabricated design of the PhC-Wg with integrated *p-i-n* diode is illustrated in Fig. 6.4 (a). Previously, the numerical calculation of the light confinement in the disorder PhC-WG and EO demonstration has been discussed and reported [120].

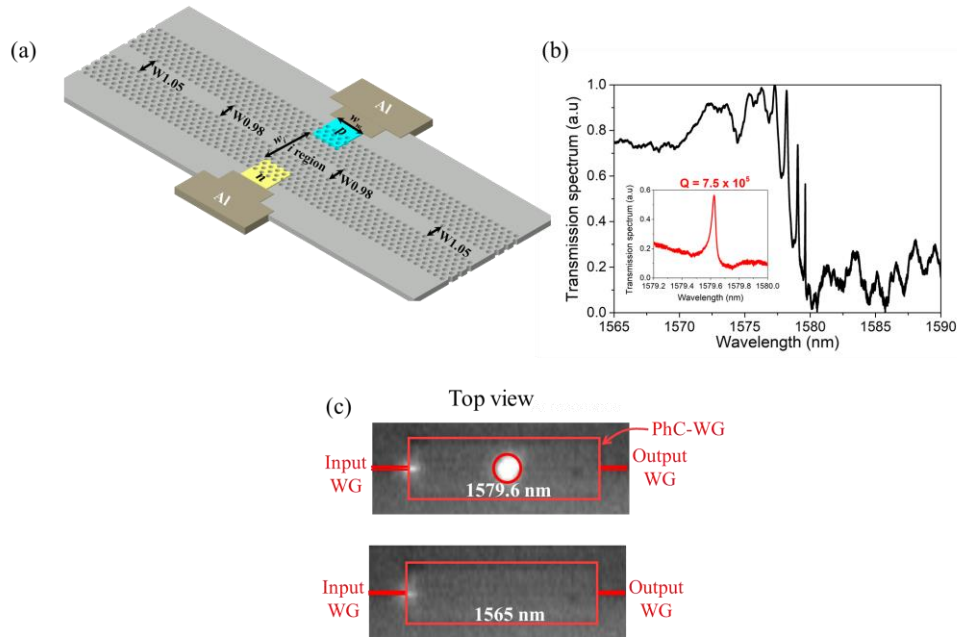


Fig. 6.4 (a) Schematic illustration of the design PhC-Wg with integrated *p-i-n* diode. (b) Transmittance spectrum of the device. The resonance peak appears to be at 1579.6 nm wavelength with high- Q value of 7.5×10^5 . (c) Images from the infrared camera at different wavelength. Light is confined at 1579.6 nm.

6.4.2 Design characteristics

As shown in Fig. 6.4 (b), the transmittance spectrum exhibits a high resonance cavity at 1579.6 nm wavelength with Q of 7.5×10^5 . The light confinement images at different input wavelengths is shown in Fig. 6.4 (c). At the input wavelength of 1579.6 nm, the image shows the light is well confined in the device which support that with a proper design, light confinement can be controlled and restricted at W0.98 waveguide.

Next, the dark current measurement is conducted to measure the value of the leak current when no light is radiated to the structure. Fig. 6.5 shows the value of the dark current when the bias voltage range from -10 V to 0 V are applied to the structure. It shows that at -3 V, the value of dark current is 78.1 pA. The dark current value is higher than the value achieved by nanocavity structure [89] is might cause by the defect at the holes that which may be produce during the fabrication.

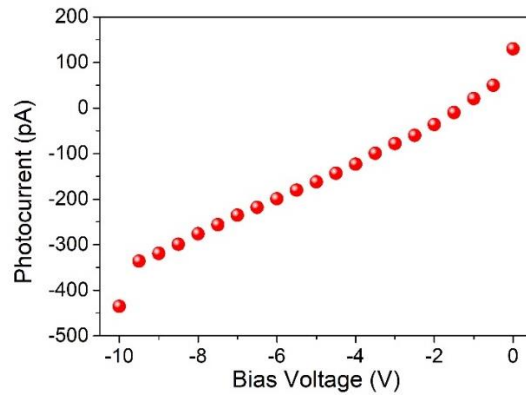


Fig. 6.5 Value of dark current at the range of 0 V to -10 V bias voltage.

6.4.3 Demonstration of OE receiver

Then, the OE receiver demonstration is demonstrated. A square train pulse signal with frequency speed of 0.1 GHz is injected to the device and the dynamic response of the receiver is measured. The signal has an amplitude of 0.5 mW at the resonance peak wavelength as shown in Fig. 6.4 (b). The result is shown in Fig. 6.6 (a).

Finally, a pseudo-random non RZ bit sequence signal waveform at bit of 2^6-1 is injected to the device, and the result is shown in Fig. 6.6 (b). The black waveform line indicates the applied signal. The red line represents the detected signal waveforms when the wavelength is set at the resonance peak. However, when the wavelength is detuned far from the resonance, no signal waveforms is detected as indicated with blue line waveforms shown in the Fig. 6.6 (b). This constitutes that the receiver is a channel selective photoreceiver. This demonstration indicates that the randomness of PhC structure is possible to be utilize for optical switching devices.

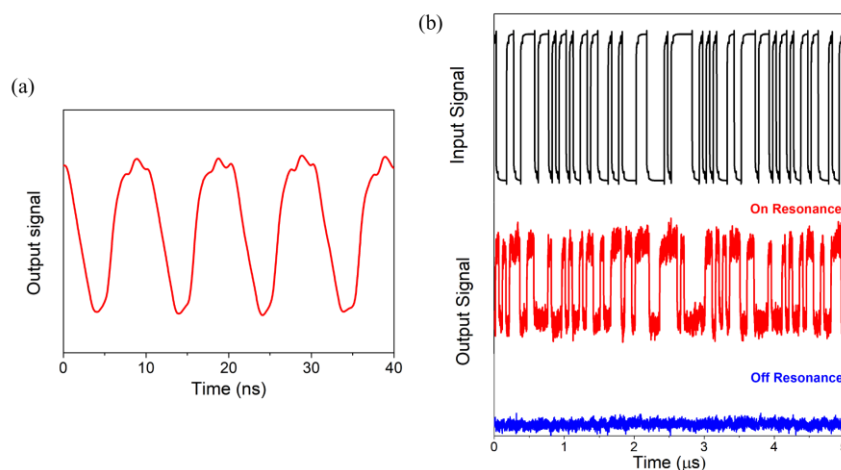


Fig. 6.6 (a) 0.1 GHz photoreceiver operation. Red line represents the output electrical signal at the resonance peak wavelength. (b) 0.1 Gbs⁻¹ receiver operation with 2^6-1 -bit pattern length non RZ signal. The red and blue line represents when the wavelength is set at the peak resonance and detune to 0.1 nm, respectively.

6.5 Temperature dependence operation

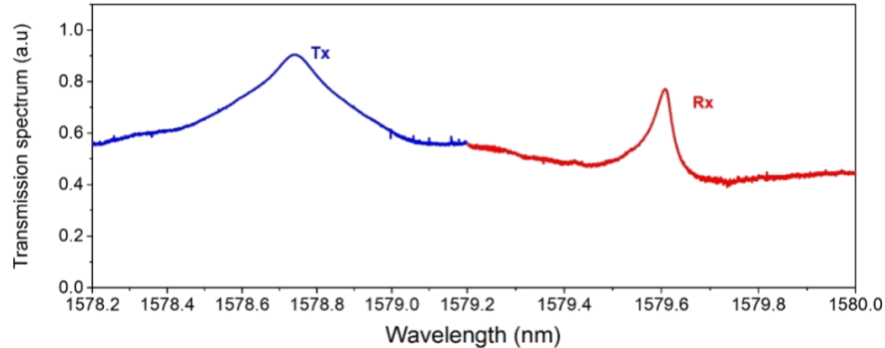


Fig. 6.7 A pair of PhC structure with closed range of resonance wavelength. The difference between two structures is approximately ~ 1 nm.

In order to conduct the PhC transmission link demonstration, two PhC structure is required – one is for the EO signal modulation (Tx) and the other is for OE signal receiver (Rx). Thus, pre-selection of a pair of two highest- Q that has close range of resonance wavelength been essential. The PhC nanocavity structure in Sec. 6.3 and PhC-WG structure in Sec. 6.4, is the close range of resonance wavelength that can be found, hence, both structures are chosen for the transceiver operation. Both resonance wavelength of the structures is shown in Fig 6.7. However, since there is still gap between both resonance wavelength, temperature dependence operation is essential to control the position of the resonance wavelength.

A Peltier unit is positioned to the sample holder to control the position of the resonance wavelength and the temperature of the units is continuously detected by a temperature sensor. The temperature is controlled by a commercial thermo-electric controller which equipped PID feedback loop. Its temperature stability is < 2 mK. The operation system is shown in Fig. 6.8.

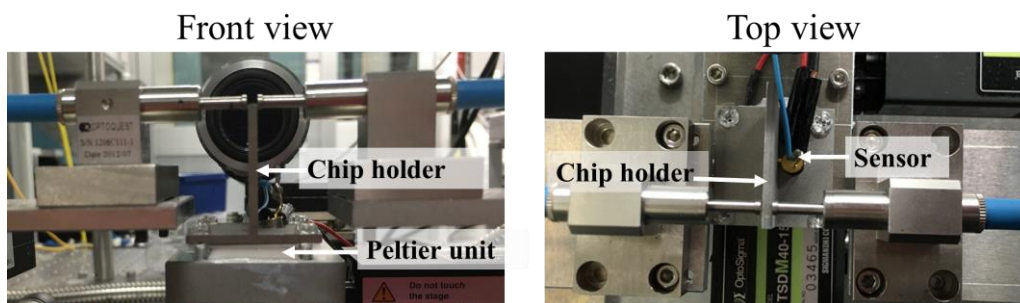


Fig. 6.8 Image of Peltier unit and temperature sensor placed at the chip holder to achieve resonance matching.

Fig. 6.9 shows the resonance shift of the PhC nanocavity structured when heat is applied. The temperature of the resonance Tx is controlled for making the resonance matched. Resonance cavity wavelength shifted for ~ 1 nm from the initial room temperature when the sample is heated to ~ 39 °C. This shows large shift of resonance wavelength is possible. Note that there will be a large fluctuation if the temperature is set at high temperature (e.g. 50 °C) due to the thermal expansion of the sample and the system. Thus, it is important to find the closest resonance wavelength.

In order to investigate the stability of the resonance shift at some temperature degree, an EO modulation operation of the structure is demonstrated after the resonance shift of Tx is matched with Rx resonance shift. A RF electrical signal of square pulse train with 100 MHz repetition rate frequency is input to the device structure. It shows clear modulation of ON to OFF contrast as shown in Fig. 6.10 which indicates that even after the resonance frequency wavelength is shifted after some temperature degree is applied, an electro-optic modulation successfully can be achieved due to the carrier-plasma effect. Therefore, it shows that the characterization of the PhC nanocavity device structure is not affected by the temperature dependence operation.

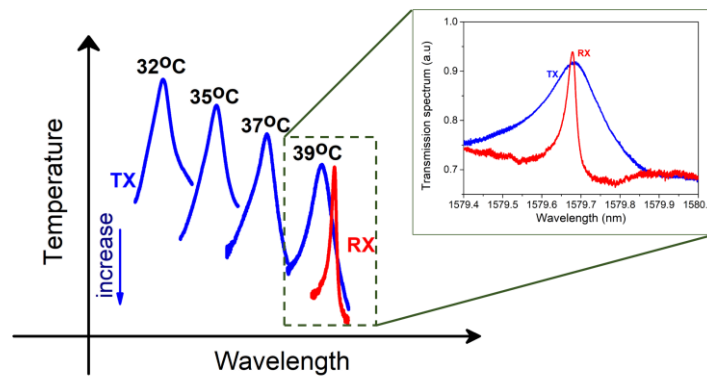


Fig. 6.9 The transmission spectrum of Tx during resonance matching. At 39 °C, Tx resonance wavelength match with Rx resonance wavelength.

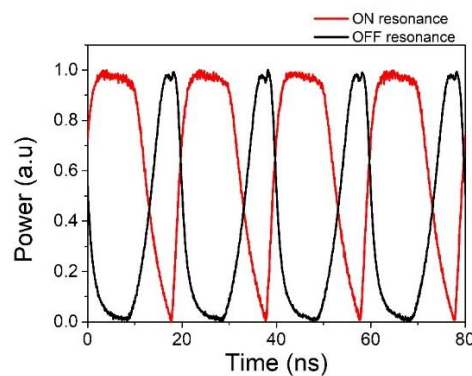


Fig. 6.10 Waveforms of modulated 50 MHz repetition rate frequency. The black and red waveforms show the signal during ON resonance (1579.65 nm) and OFF resonance (detune -0.1 nm), respectively.

6.6 All-Si scheme PhC transmission link demonstration

Next, the demonstration of transmitter and receiver transmission link operation is conducted. The PhC nanocavity structure is chosen to be the Tx component due to the better EO modulation characteristics and PhC-WG structure is chosen to be the Rx component due to the better OE receiver characteristics. The demonstration requires two measurement setup – one for the Tx operation system and the other for Rx operation system. Since both Tx and Rx component devices are basically same PhC structures device and different in terms of design structure, thus, all-Si scheme link is achieved.

After confirmed the resonance matched for both Tx and Rx components, the measurement device is set-up as Fig. 6.11 as back-to-back measurement. The wavelength is set to 1579.70 nm for Tx component working point. 100 MHz of square pulse repetition rate from the PPG is transmitted to the Tx component. The power is boost by the EDFA and the noise is eliminated by the BPF. Then, the filtered optical signal is coupled to the Rx component. -3 V reverse-biased voltage is applied at the Rx component and finally the output electrical signal is amplified by TIA with gain of 5×10^3 V/A.

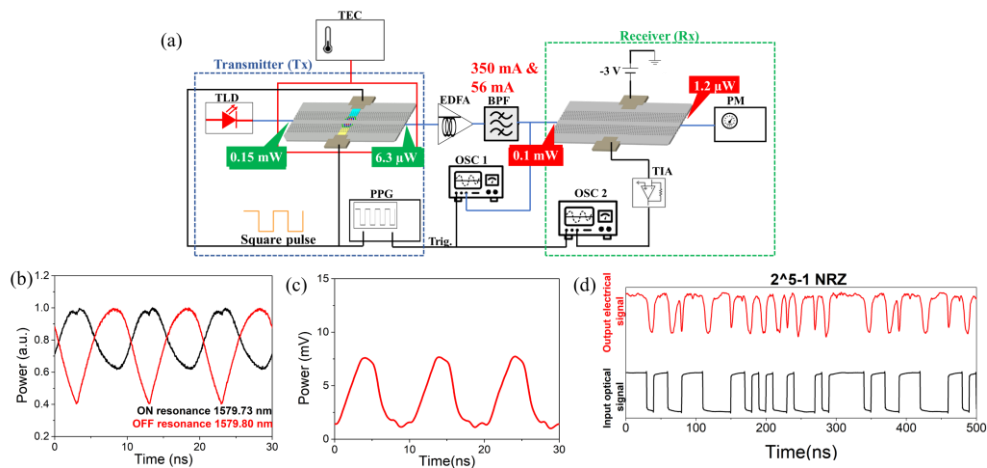


Fig. 6.11 (a) Experimental setup for all-Si scheme of transmitter and receiver demonstration for back-to-back transmission links. (b) Modulated signal observed at oscilloscope (OSC 1). The black line signal represents the on resonance and red line represents the off resonance when -0.1 nm wavelength is detuned. (c) Detected signal observed at oscilloscope (OSC 2). The signal is observed at 1579.73 nm. (d) PRBS signal is observed at NRZ 2^5-1 -bit sequence at 0.1 GHz.

The power value of modulated optical signal after the PhC nanocavity modulator is monitored before EDFA where the value is $1.99 \mu\text{W}$. The optical signal was amplified to 0.63 mW after gone through the EDFA amplification and BPF filter before reach the receiver operation system.

Fig 6.12 illustrated the measurement of 5 m transmission link and signals that observed at the modulation and receiver operation. 50 MHz square pulse signal and NRZ 2^5-1 -bit sequence PRBS signal is transmitted at the transmission link system.

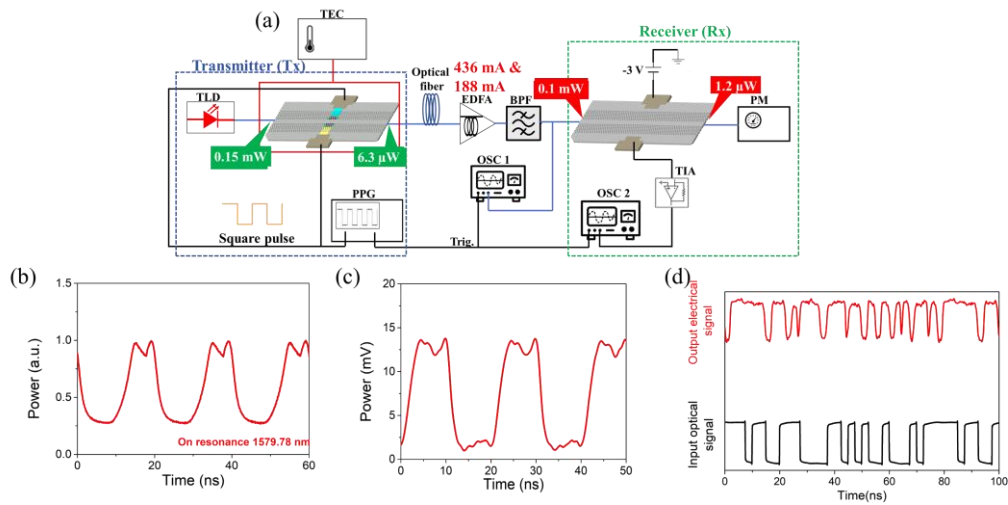


Fig. 6.12 Experimental setup for 5 m transmission link. Received electrical signal from modulated square pulse and NRZ 2^5 -1-bit sequence PRBS signal is observed at the oscilloscope.

6.7 Discussion

The results show that maximum operating speed of the device is 100 MHz by back-to-back operation. The obtained preliminary results indicate that, the proposed device structure has a potential to be a practically integrated as optical transmission link system. However, this could be realized only after further improved the operating bandwidth which can be done by optimizing doping concentration and make small Al contact pad. By overcome the limiting factor of the device, the expected bandwidth can be increased up to ~ GHz [161], [216].

Since the operating speed of the device is very low, it is very important to fully optimize the device. Therefore, although, for optical transmission link system bit-error rate (BER) measurement is commonly essential to determine the quality of transmission system, it could not be done at this stage. However, the BER measurement will be essential with an optimized PhC nanocavity device.

Both PhC nanocavity device used in this study are fabricated using photolithography fabrication technique, they are compatible with CMOS devices and the presence of SiO_2 -clad makes the device to be robust and stable. Although the fabrication of photolithography is not as precise as EB lithography and fabrication error is expected, the study has shown that the fabrication error which caused by randomness, possible to be functioned as optical device. On the other hand, due to the simple fabrication and dense integration of all-silicon scheme, high production grow with lower cost is expected which can be an option to build the transmission link in future.

Recent study has shown silicon photonic optical transmission link device is now towards chip-to-chip [85] and on chip transmission link system [86]. Therefore, as future work of this study, despite from the optimization, it is necessary to integrate both chip (Tx and Rx) monolithically (on a single chip). The integration on a single chip is possible since we fabricated the device using a mature silicon foundry fabrication process.

6.8 Summary

An all-Si scheme of transmitter and receiver by CMOS compatible PhC structure is demonstrated. The system utilized both PhC nanocavity structure and PhC-WG randomness structure that constitutes the PhC structure possible to be utilized even with the presence of fabrication error. Signal transmission of 5 m with 0.05 GHzs^{-1} of 2⁵-1-bit NRZ is successfully modulated and detected in the system. This is the first demonstration of transmitter and receiver by PhC structure, so it shows that the device has a potential for all-Si transmission link in near future.

Chapter 7

Summary and outlook

In this chapter, the thesis is concluded. First, the results obtained in each chapter in the thesis are summarized. Then, conclusion and outlook of the thesis are described. Finally, future perspective of the PhC are described.

7.1 Summary of each chapter

7.1.1 Theory of photonic crystal ([Chapter 2](#))

Chapter 2 explained fundamental theory of PhC. The chapter contains of 4 sections: (1) photonic band structure, (2) Fabry-Pèrot cavity (3) method of analysis and (4) PhC nanocavity device design structure that used in this study. Section (1) in this chapter, explained the basic concept of photonic band structure. It described the Maxwell's equation which lead to origin of PBG and cavity formation of line and point defect. Section (2), described the nanocavity where Fabry-Pèrot cavity is used as an example. In Section (3), basic method of analysis was described. It consists of plane-wave method for band gaps calculation at different polarization and light propagation calculation of FDTD. Finally, design of PhC structure that used in this study was explained in section (4). Methods to form cavity and expected value of Q -factor were described in this section. The simulation result was compared with the fabricated device. It showed the device exhibit high- Q cavity and was supported with experimental measurement results.

Therefore, contents in Chapter 2 was essential as it explained the fundamental concept which led to the device fabrication design that used in this whole study. It is important to understand technique to achieve a high- Q cavity in this study.

7.1.2 PhC nanocavity laterally embedded with $p-i-n$ diode fabrication process (Chapter 3)

In Chapter 3, PhC fabrication process was introduced. Photolithography fabrication technique that used to fabricate PhC nanocavity device also described in detail in this chapter. The chapter was divided into three sections: (1) overview of PhC fabrication process, (2) photolithography fabrication procedure used in this study and (3) comparison with previous study's device. In section (1), an overview of PhC fabrication process technique was described. PhC structure requires a precise technique to avoid scattering loss that will make the crystal properties become blur, thus, will affect the application of the device. Therefore, the holes of the PhC should be patterned carefully onto a substrate. The layer-by-layer etching technique can be performed in different methods. EB lithography, interference lithography or photolithography are some of general methods to perform etching process. Then, fabrication process that used to fabricate the PhC structure in this study was described in section (2). The section contains basic photolithography process which described type of light source that used to fabricate the device and integration process to integrate $p-i-n$ diode and contacting pads to the substrate. Finally, section (3) explained the comparison of current device structure fabrication process with previously reported device structure fabrication process.

The fabrication process that used in this study to fabricate the device constitutes an advantage in terms of stability, robustness and higher integration level. It showed it is possible to fabricate PhC device structure using a high mass productivity fabrication technique without degrade the number of Q factor. Therefore, Chapter 3 was important to the entire thesis.

7.1.3 Electro-optic modulator based on PhC nanocavity (Chapter 4)

Chapter 4, demonstrated a sub-GHz EO modulation of SiO₂-clad PhC nanocavity based on carrier plasma dispersion effect. First, refractive index modulation is investigated by carrier's injection. Although a small modulation of refractive index is achieved but due to the high- Q obtained through photolithography fabrication process, allows the device to enable large optical modulation. Next, carriers' recombination and extraction at $p-i-n$ region is observed by RF operation. Finally, 0.5 GHz modulation signal frequency is demonstrated and -3 dB cut-off frequency of the device appears to be at 0.35 GHz with maximum extinction ratio of 6.37 dB.

This study offers a smaller footprint of 50 μm^2 compared to MZI-based modulator and thus, requires lower operating power of 2.76 μA . Although similar studied has been done previously, this study proposed a high integration level as it is compatible with CMOS process. The low operating power and large optical modulation of this study becomes an important element for Chapter 6. Although in terms of speed the device is much smaller compared to other commercialized modulator device, but with the miniaturization of size and small modulation range, the device possible to be applied in pilot monitoring signal and as sensing device. The limiting factor in regards the speed of the device has been clearly discussed in the chapter.

7.1.4 PhC nanocavity photoreceiver (Chapter 5)

In chapter 5, a demonstration of PhC nanocavity photoreceiver was described. Silicon is known as transparent at telecom wavelength, therefore silicon is not an efficient material to be demonstrated as photoreceiver. Even though several methods had been introduced to enhance property of silicon as photoreceiver, they suffer with high dark current and complexity of fabrication. This chapter contained characteristics of PhC nanocavity as photoreceiver.

It showed that the device achieved low dark current value of 38 pA and minimum detectable optical power of 10 μ W. It also showed that the device can operated as channel selective photoreceiver with 0.1 Gbit/s. Therefore, it is suitable for power monitoring device application. Due to the all-silicon made, simplicity of the fabrication device and small in size, give an advantage to the device as low-cost and compact size power monitoring device.

The performance of the device was fairly compared with other types of photodetectors. Although the device is not superior for every characteristic, especially in terms of quantum efficiency, but it paved a way that PhC nanocavity is towards future mass production. Therefore, Chapter 5 one of the key elements for Chapter 6.

7.1.5 All-Si scheme PhC nanocavity transmission link (Chapter 6)

Chapter 6, demonstrated all-Si scheme of PhC nanocavity transmission link. This is the first demonstration of all-Si scheme transmission link by PhC nanocavity structure. In this demonstration, two different PhC nanocavity structures were utilized where perfectly localized light in nanocavity structure as modulator and randomly localized light due to fabrication error structure as receiver. Although the design of PhC used for modulator and receiver are different but both used same technology of light localization. The characteristics of PhC randomness structure was described and showed that even the structure was fabricated with disorder, it is still possible to be utilized as a detector. The temperature dependence operation was conducted to detune the resonance wavelength of both modulator and receiver to be as close as possible. Finally, back-to-back transmission link was demonstrated with 0.1 GHz operation speed and 5 m optical fiber transmission link was demonstrated with 50 MHz operation speed.

Although the device shown a low operating speed in which 0.1 GHz, through calculation of carrier transit time and low-pass filter shows that this device can work up until \sim 5 GHz. This can be enhanced with optimizing the doping concentration of n^+ and p^+ . By enhancing the operating speed performance of the device, it can be applied for intra-chip transmission link in data centers. Since the PhC nanocavity device is fabricated using matured silicon foundry which is compatible with CMOS electrical circuit, allows an easy integration with other circuits on a single chip. In addition, due to ease of fabrication and compact in size, makes the cost to fabricate the device low. This constitutes that future intra-chip transmission link is towards a higher dense of integration, simple in fabrication, compact in size and most importantly cost-effectively.

7.2 Conclusion and outlook of the thesis

In this thesis, the applications of PhC nanocavity slab fabricated by photolithography technique with SiO₂-clad surface have been studied so far. The applications included electro-optic

modulator and photoreceiver. To the present, PhC slab has been demonstrated as an electro-optic modulator [61] and detector [200], but the device was fabricated using high precision EB lithography technique that requires an air-bridge structure to obtain a high- Q cavity. The high precision fabrication method is necessary to fabricate holes of PhC structure accurately. Therefore, an air-bridge structure is required. This is because previously work has reported PhC slab with SiO₂-clad surface achieved a poor Q [93]. The formation of an air-bridge structure will sacrifice the SiO₂ clad of the device and makes the device fragile. In addition, the high precision EB fabrication process is challenging for mass-production due to longer time consume of device fabrication. Thus, makes the EB fabricated PhC slab with an air-bridge structure is not significant to be commercialized. The main factor to commercialize the technology, the device should be process in a CMOS fabrication facility and together with existing CMOS electronic wafers [217].

Therefore, here comes the advantages of the study where the PhC nanocavity device is fabricated using mature silicon foundry of photolithography that has higher mass-production. In addition, the device is robust and stable because it is cladded with SiO₂-clad. It is proved, even using a photolithography fabrication process, it is possible to fabricate perfectly PhC holes and without the existence of an air-bridge structure, it is possible to achieve a high- Q factor. This allows the device to be demonstrated with various functionalities. Furthermore, since the device is fabricated with CMOS compatible fabrication process, it allows the device to be fabricated with other electrical circuits on the same chip. Hence, the photolithographically fabricated with SiO₂-clad surface PhC slab appear to be promising not only in terms of compatibility with CMOS devices but also as transmission link system.

The achievements of this thesis can be summarized as follows:

- (1) The demonstration of electro-optic modulator and photoreceiver operation was experimentally investigated in detail which describe the application of high- Q PhC nanocavity structure as optical interconnect device. These are the key element to bridge the electrical circuit with photonic circuit. Although, normally, all-Si structure device is reported not a sufficient material to demonstrate as photoreceiver, however, due to the ultra-high- Q and small mode volume of the structure, optical non-linearities (χ^3) effect occur and TPA exceeds the bandgap makes light detection becomes possible. Without a high- Q factor value, the device will be an ordinary glass. This constitutes that all-Si photodetection device is possible.
- (2) The transmitter and receiver operation of PhC nanocavity structure also has been demonstrated as an optical transmission link. Although with low operating speed, this study constitutes an all-silicon transmission link is achievable with PhC structure. Since light modulation and detection is obtained through a monolithic material which is all-silicon structure, so, there is no conflict of requirements with respect to light absorption between the modulator material and detector material [218]. In addition, due to the high compatibility of the device with CMOS devices, PhC nanocavity structure promise a high degree level of integration.

Although, the device required a further improvement in terms of operating speed performance, but the miniaturization of the device in size, cost-effective fabrication, simplicity in package and compatibility with CMOS devices makes the device one of the best candidates for future optical interconnect device component. Since nowadays, silicon photonics device is towards realization of on chip distance data transmission, thus, high integration optical interconnect becomes a

demand. Early of 2018, chip-to-chip transmission signal has been demonstrated and recently, on chip system of silicon photonic data transmission has been reported. This indicates the important of the study where it allows a higher degree of integration. In addition, due to the compactness of the size, gives another advantage to the device.

References

- [1] M. D. Al-amri, M. M. El-gomati, and M. S. Zubairy, *Optics in Our Time*. 2016.
- [2] T. Barnett, A. Sumits, S. Jain, U. Andra, and T. Khurana, “Cisco Global Cloud Index,” *CISCO, Cisco Global Cloud Index 2015–2020*, 2020. .
- [3] G. E. Moore, “Cramming more components onto integrated circuits,” *Electronics*, vol. 38, no. 8, p. 114, 1965.
- [4] E. Yablonovitch, “Inhibited spontaneous emission in solid-state physics and electronics,” *Phys. Rev. Lett.*, vol. 58, no. 20, pp. 2059–2062, 1987.
- [5] N. Farrington and A. Andreyev, “Facebook ’ s Data Center Network Architecture,” in *IEEE Optical Interconnects Conference*, 2013, p. TuB5.
- [6] Z. Zhou, R. Chen, X. Li, and T. Li, “Development trends in silicon photonics for data centers,” *Opt. Fiber Technology*, vol. 44, pp. 13–23, 2018.
- [7] Lord Rayleigh, “propagation of waves through a medium endowed with a periodic structure.pdf,” *philosophical magazine*, pp. 145–159, 1887.
- [8] S. John, “Strong localization of photons in certain disorder dielectric superlattices,” *Phys. Rev. Lett.*, vol. 58, no. 23, pp. 2486–2489, 1987.
- [9] E. Yablonovitch, “In the limelight,” *Nat. Mater.*, vol. 11, no. December, pp. 1000–1001, 2012.
- [10] M. L. Dakss, L. Kuhn, P. F. Heidrich, and B. A. Scott, “GRATING COUPLER FOR EFFICIENT EXCITATION OF OPTICAL GUIDED WAVES IN THIN FILMS,” *Appl. Phys. Lett.*, vol. 16, no. 523, pp. 14–17, 1970.
- [11] T. Tamir and S. T. Peng, “Analysis and Design of Grating Couplers,” *Appl. Phys.*, vol. 14, pp. 235–254, 1977.
- [12] K. Tiefenthaler and W. Lukosz, “Sensitivity of grating couplers as integrated-optical chemical sensors,” *J. Opt. Soc. Am. B*, vol. 6, no. 2, pp. 209–220, 1989.
- [13] D. Taillaert *et al.*, “An Out-of-Plane Grating Coupler for Efficient Butt-Coupling Between Compact Planar Waveguides and Single-Mode Fibers,” *IEEE J. Quantum Electron.*, vol. 38, no. 7, pp. 949–955, 2002.
- [14] D. Taillaert *et al.*, “Grating Couplers for Coupling between Optical Fibers and Nanophotonic Waveguides,” *Jpn. J. Appl. Phys.*, vol. 45, no. 8A, pp. 6071–6077, 2006.
- [15] A. Mekis *et al.*, “A Grating-Coupler-Enabled CMOS Photonics Platform,” *IEEE J. Sel. Top. Quantum Electron.*, vol. 17, no. 3, pp. 597–608, 2011.
- [16] P. R. Villeneuve *et al.*, “Air-bridge microcavities,” *Appl. Phys. Lett.*, vol. 67, no. 167, 1995.
- [17] J. S. Foresi *et al.*, “Photonic-bandgap microcavities in optical waveguides,” *Nature*, vol. 390, pp. 143–145, 1997.
- [18] P. B. Deotare, M. W. Mccutcheon, I. W. Frank, M. Khan, and M. Lončar, “High quality factor photonic crystal nanobeam cavities,” *Appl. Phys. Lett.*, vol. 94, no. 121106, 2009.

- [19] Q. Quan and M. Loncar, “Deterministic design of wavelength scale , ultra-high Q photonic crystal nanobeam cavities,” *Opt. Express*, vol. 19, no. 19, pp. 258–265, 2011.
- [20] A. L. Bingham and D. Grischkowsky, “High , one-dimensional terahertz photonic waveguides,” *Appl. Phys. Lett.*, vol. 90, no. 091105, 2007.
- [21] M. Eichenfield, R. Camacho, J. Chan, K. J. Vahala, and O. Painter, “A picogram- and nanometre-scale photonic-crystal optomechanical cavity,” *Nature*, vol. 459, no. May, pp. 550–555, 2009.
- [22] L. Haret, T. Tanabe, E. Kuramochi, and M. Notomi, “Extremely low power optical bistability in silicon demonstrated using 1D photonic crystal nanocavity,” *Opt. Express*, vol. 17, no. 23, pp. 21108–21117, 2009.
- [23] M. Eichenfield, J. Chan, R. M. Camacho, K. J. Vahala, and O. Painter, “Optomechanical crystals,” *Nature*, vol. 461, no. November, pp. 78–82, 2009.
- [24] M. Plihal, A. Shambrook, and A. A. Maraduddin, “Two-dimensional photonic band structures,” *Opt. Commun.*, vol. 80, no. 3,4, pp. 199–204, 1991.
- [25] M. Plihal and A. A. Maraduddin, “Photonic band structure of two-dimensional systems: The triangular lattice,” *Phys. Rev. B*, vol. 44, no. 16, 1991.
- [26] R. D. Meade *et al.*, “Existence of a photonic band gap in two dimensions,” *Appl. Phys. Lett.*, vol. 61, no. 4, 1992.
- [27] E. Yablonovitch, T. J. Gmitter, D. Meade, A. M. Rappe, K. D. Brommer, and J. D. Joannopoulos, “Donor and Acceptor Modes in Photonic Band Structure,” *Phys. Rev. Lett.*, vol. 67, no. 24, pp. 3380–3383, 1991.
- [28] O. Painter, J. Vuckovic, and A. Scherer, “Defect modes of a two-dimensional photonic crystal in an optically thin dielectric slab,” *J. Opt. Soc. Am. B*, vol. 16, no. 2, pp. 275–285, 1999.
- [29] O. Painter *et al.*, “Two-Dimensional Photonic Band-Gap Defect Mode Laser,” *Science (80-.)*, vol. 284, no. June, pp. 1819–1822, 1999.
- [30] Y. Akahane, T. Asano, B. Song, and S. Noda, “High- Q photonic nanocavity in a two-dimensional photonic crystal,” *Nature*, vol. 425, no. October, pp. 944–947, 2003.
- [31] Y. Akahane, T. Asano, B. Song, and S. Noda, “Fine-tuned high-Q photonic-crystal nanocavity,” *Opt. Express*, vol. 13, no. 4, pp. 1908–1910, 2005.
- [32] T. Tanabe, M. Notomi, S. Mitsugi, A. Shinya, and E. Kuramochi, “All-optical switches on a silicon chip realized using photonic crystal nanocavities,” *Appl. Phys. Lett.*, vol. 87, p. 15112, 2005.
- [33] C. Husko, A. De Rossi, S. Combri , Q. V. Tran, F. Raineri, and C. W. Wong, “Ultrafast all-optical modulation in GaAs photonic crystal cavities,” *Appl. Phys. Lett.*, vol. 94, no. 021111, 2009.
- [34] K. Nozaki *et al.*, “Sub-femtojoule all-optical switching using a photonic-crystal nanocavity,” *Nat. Photonics*, vol. 4, no. July, pp. 477–483, 2010.
- [35] K. Nozaki, S. Kita, and T. Baba, “Room temperature continuous wave operation and controlled spontaneous emission in ultrasmall photonic crystal nanolaser,” *Opt. Express*, vol. 15, no. 12, pp. 7506–7514, 2007.

- [36] B.-S. Song, S. Noda, A. Takashi, and Y. Akahane, "Ultra-high-Q photonic double-heterostructure nanocavity," *Nat. Mater.*, vol. 4, no. March, pp. 207–210, 2005.
- [37] E. Kuramochi, M. Notomi, S. Mitsugi, A. Shinya, T. Tanabe, and T. Watanabe, "Ultrahigh-Q photonic crystal nanocavities realized by the local width modulation of a line defect," *Appl. Phys. Lett.*, vol. 88, no. 4, p. 041112, 2006.
- [38] T. Tanabe *et al.*, "Fast all-optical switching using ion-implanted silicon photonic crystal nanocavities," *Appl. Phys. Lett.*, vol. 90, no. 031115, 2007.
- [39] M. Notomi *et al.*, "Low-power nanophotonic devices based on photonic crystals towards dense photonic network on chip," *IET Circuits, Devices Syst.*, vol. 5, no. 2, p. 84, 2011.
- [40] E. Yablonovitch and T. J. Gmitter, "Photonic band structure : the face-centered-cubic case," *J. Opt. Soc. Am. A*, vol. 7, no. 9, pp. 1792–1800, 1990.
- [41] S. Takahashi, T. Tajiri, K. Watanabe, Y. Ota, S. Iwamoto, and Y. Arakawa, "High-Q nanocavities in semiconductor-based three-dimensional photonic crystals," *Electron. Lett.*, vol. 54, no. 5, pp. 305–307, 2018.
- [42] K. Ishizaki and S. Noda, "Manipulation of photons at the surface of three-dimensional photonic crystals," *Nature*, vol. 460, pp. 367–370, 2009.
- [43] A. Tandraechanurat, S. Ishida, D. Guimard, M. Nomura, S. Iwamoto, and Y. Arakawa, "Lasing oscillation in a three-dimensional photonic crystal nanocavity with a complete bandgap," *Nat. Photonics*, vol. 5, no. February, pp. 91–94, 2011.
- [44] R. A. Soref and B. R. Bennett, "Electrooptical Effects in Silicon," *IEEE J. Quantum Electron.*, vol. QE-23, no. 1, pp. 123–129, 1987.
- [45] G. T. Reed and B. L. Weiss, "ELECTRO-OPTIC EFFECT IN He + -IMPLANTED OPTICAL WAVEGUIDES MULTIPLIER USING SUPER CAPACITOR," *Electron. Lett.*, vol. 23, no. 8, pp. 424–425, 1987.
- [46] I. P. Kaminow, J. R. Carruthers, E. H. Turner, and L. W. Stulz, "Thin-film LiNbO₃ electro-optic light modulator," *Appl. Phys. Lett.*, vol. 22, no. 10, pp. 540–542, 1973.
- [47] K. Noguchi, O. Mitomi, H. Miyazawa, and S. Seki, "A Broadband Ti:LiNbO₃ Optical Modulator with a Ridge Structure," *J. Light. Technol.*, vol. 13, no. 6, pp. 1164–1168, 1995.
- [48] K. Noguchi, O. Mitomi, and H. Miyazawa, "Millimeter-Wave Ti : LiNbO₃ Optical Modulators," *J. Light. Technol.*, vol. 16, no. 4, pp. 615–619, 1998.
- [49] E. L. Wooten *et al.*, "A review of lithium niobate modulators for fiber-optic communications systems," *IEEE J. Sel. Top. Quantum Electron.*, vol. 6, no. 1, pp. 69–82, 2000.
- [50] N. Courjal *et al.*, "Simple production of membrane-based LiNbO₃ micro-modulators with integrated tapers," *Opt. Lett.*, vol. 41, no. 21, p. 5110, 2016.
- [51] R. A. Soref and B. R. Bennett, "Kramers–Kronig analysis of electro-optical switching in silicon," *Proc. SPIE Integr. Opt. Circuit Eng. IV*, vol. 704, pp. 32–37, 1987.
- [52] C. E. Png, S. P. Chan, S. T. Lim, and G. T. Reed, "Optical Phase Modulators for MHz and GHz Modulation in Silicon-On-Insulator (SOI)," *J. Light. Technol.*, vol. 22, no. 6, pp. 1573–1582, 2004.
- [53] D. J. Thomson *et al.*, "50-Gb/s silicon optical modulator," *IEEE Photonics Technol. Lett.*,

- vol. 24, no. 4, pp. 234–236, 2012.
- [54] T. Baba, H. C. Nguyen, N. Yazawa, Y. Terada, S. Hashimoto, and T. Watanabe, “Slow-light Mach–Zehnder modulators based on Si photonic crystals,” *Sci. Technol. Adv. Mater.*, vol. 15, no. 2, p. 024602, Apr. 2014.
- [55] Q. Xu, B. Schmidt, S. Pradhan, and M. Lipson, “Micrometre-scale silicon electro-optic modulator,” *Nature*, 2005. [Online]. Available: <http://www.nature.com/nature/journal/v435/n7040/pdf/nature03569.pdf>. [Accessed: 24-Mar-2016].
- [56] X. Xiao *et al.*, “25 Gbit/s silicon microring modulator based on misalignment-tolerant interleaved PN junctions,” *Opt. Express*, vol. 20, no. 3, p. 2507, 2012.
- [57] M. Soljačić, S. G. Johnson, S. Fan, M. Ibanescu, E. Ippen, and J. D. Joannopoulos, “Photonic-crystal slow-light enhancement of nonlinear phase sensitivity,” *J. Opt. Soc. Am. B*, vol. 19, no. 9, pp. 2052–2059, 2002.
- [58] Y. Jiang, W. Jiang, L. Gu, X. Chen, and R. T. Chen, “80-micron interaction length silicon photonic crystal waveguide modulator,” *Appl. Phys. Lett.*, vol. 221105, no. 87, 2005.
- [59] L. Gu, W. Jiang, X. Chen, L. Wang, and R. T. Chen, “High speed silicon photonic crystal waveguide modulator for low voltage operation,” *Appl. Phys. Lett.*, vol. 90, no. 071105, 2007.
- [60] X. Chen, Y. Chen, Y. Zhao, W. Jiang, and R. T. Chen, “Capacitor-embedded 0.54 pJ/bit silicon-slot photonic crystal waveguide modulator,” *Opt. Lett.*, vol. 34, no. 5, pp. 602–604, 2009.
- [61] T. Tanabe, K. Nishiguchi, E. Kuramochi, and M. Notomi, “Low power and fast electro-optic silicon modulator with lateral p-i-n embedded photonic crystal nanocavity,” *Opt. Express*, vol. 17, no. 25, pp. 22505–22513, Dec. 2009.
- [62] G. E. Stillman, V. M. Robbins, and N. Tabatabaie, “III-V Compound Semiconductor Devices : Optical Detectors,” *IEEE Trans. electron devices*, vol. ED-31, no. 11, pp. 1643–1655, 1984.
- [63] T. K. Woodward and A. V Krishnamoorthy, “1-Gb / s Integrated Optical Detectors and Receivers in Commercial CMOS Technologies,” *IEEE J. Sel. Top. Quantum Electron.*, vol. 5, no. 2, pp. 146–156, 1999.
- [64] J. Michel, J. Liu, and L. C. Kimerling, “High-performance Ge-on-Si photodetectors,” *Nat. Photonics*, vol. 4, no. 8, pp. 527–534, 2010.
- [65] L. Dou *et al.*, “Solution-processed hybrid perovskite photodetectors with high detectivity,” *Nat. Commun.*, vol. 5, pp. 1–6, 2014.
- [66] J. Zhang, M. A. Itzler, H. Zbinden, and J. W. Pan, “Advances in InGaAs/InP single-photon detector systems for quantum communication,” *Light Sci. Appl.*, vol. 4, no. January, pp. 1–13, 2015.
- [67] N. Duan, T. Liow, A. E. Lim, L. Ding, and G. Q. Lo, “310 GHz gain-bandwidth product Ge / Si avalanche photodetector for 1550 nm light detection,” *Opt. Express*, vol. 20, no. 10, pp. 11031–11036, 2012.
- [68] L. Q. Chen *et al.*, “High-performance Ge p-i-n photodetector on Si substrate,” *Optoelectron. Lett.*, vol. 11, no. 3, pp. 195–198, 2015.

- [69] J. Cui and Z. Zhou, "High-performance Ge-on-Si photodetector with optimized DBR location," *Opt. Lett.*, vol. 42, no. 24, p. 5141, 2017.
- [70] J. Wang and S. Lee, "Ge-photodetectors for Si-based optoelectronic integration," *Sensors*, vol. 11, no. 1, pp. 696–718, 2011.
- [71] I. Umezu *et al.*, "Emergence of very broad infrared absorption band by hyperdoping of silicon with chalcogens," *J. Appl. Phys.*, vol. 113, no. 21, 2013.
- [72] Y. Berencén *et al.*, "Room-temperature short-wavelength infrared Si photodetector," *Sci. Rep.*, vol. 7, no. January, pp. 1–9, 2017.
- [73] S. Oh, Y. Jung, M. A. Mastro, J. K. Hite, C. R. Eddy, and J. Kim, "Development of solar-blind photodetectors based on Si-implanted β -Ga₂O₃," *Opt. Express*, vol. 23, no. 22, p. 28300, 2015.
- [74] Y. Li and A. W. Poon, "Active resonance wavelength stabilization for silicon microring resonators with an in-resonator defect-state-absorption-based photodetector," *Opt. Express*, vol. 23, no. 1, p. 360, 2015.
- [75] J. K. Doylend, P. E. Jessop, and a P. Knights, "Silicon photonic resonator-enhanced defect-mediated photodiode for sub-bandgap detection.," *Opt. Express*, vol. 18, no. 1, pp. 14671–14678, 2010.
- [76] R. R. Grote, K. Padmaraju, B. Souhan, J. B. Driscoll, K. Bergman, and R. M. Osgood, "10 Gb/s error-free operation of all-silicon ion-implanted-waveguide photodiodes at 1.55 μ m," *IEEE Photonics Technol. Lett.*, vol. 25, no. 1, pp. 67–70, 2012.
- [77] H. Zhu, L. Zhou, Y. Zhou, Q. Wu, X. Li, and J. Chen, "All-Silicon Waveguide Avalanche Photodetectors With Ultrahigh Gain-Bandwidth Product and Low Breakdown Voltage," *IEEE J. Sel. Top. Quantum Electron.*, vol. 20, no. 6, pp. 1–6, 2014.
- [78] T. Tanabe, H. Sumikura, H. Taniyama, A. Shinya, and M. Notomi, "All-silicon sub-Gb/s telecom detector with low dark current and high quantum efficiency on chip," *Appl. Phys. Lett.*, vol. 96, p. 101103, 2010.
- [79] X. Li, Z. Li, X. Xiao, H. Xu, J. Yu, and Y. Yu, "40 Gb / s All-Silicon Photodetector Based on Microring Resonators," *IEEE Photonics Technol. Lett.*, vol. 27, no. 7, pp. 729–732, 2015.
- [80] B. Analui, D. Guckenberger, D. Kucharski, and A. Narasimha, "A Fully Integrated 20-Gb / s Optoelectronic Transceiver Implemented in a Standard," *IEEE J. Solid-State Circuits*, vol. 41, no. 12, pp. 2945–2955, 2006.
- [81] T. Pinguet *et al.*, "Monolithically Integrated High-Speed CMOS Photonic Transceivers," in *2008 5th IEEE International Conference on Group IV Photonics*, 2008, vol. 1, pp. 362–364.
- [82] L. Chen, K. Preston, S. Manipatruni, and M. Lipson, "Integrated GHz silicon photonic interconnect with micrometer-scale modulators and detectors," *Opt. Express*, vol. 17, no. 17, pp. 15248–15256, 2009.
- [83] J. F. Buckwalter, X. Zheng, G. Li, K. Raj, and A. V Krishnamoorthy, "A Monolithic 25-Gb / s Transceiver With Photonic Ring Modulators and Ge Detectors in a 130-nm CMOS SOI Process," *IEEE J. Solid-State Circuits*, vol. 47, no. 6, pp. 1309–1322, 2012.
- [84] C. Li *et al.*, "Silicon Photonic Transceiver Circuits With Microring Resonator Bias-Based

- Wavelength Stabilization in 65 nm CMOS,” *IEEE J. Solid-State Circuits*, vol. 49, no. 6, pp. 1419–1436, 2014.
- [85] H. Zhu, K. Goi, and K. Ogawa, “All-Silicon Waveguide Photodetection for Low-Bias Power Monitoring and 20-km 28-Gb/s NRZ-OOK Signal Transmission,” *IEEE J. Sel. Top. Quantum Electron.*, vol. 24, no. 2, p. 4400207, 2018.
- [86] A. H. Atabaki *et al.*, “Integrating photonics with silicon nanoelectronics for the next generation of systems on a chip,” *Nature*, vol. 556, no. 7701, pp. 349–354, 2018.
- [87] Y. Ooka, T. Tetsumoto, A. Fushimi, W. Yoshiki, and T. Tanabe, “CMOS compatible high-Q photonic crystal nanocavity fabricated with photolithography on silicon photonic platform,” *Sci. Rep.*, vol. 5, no. February, p. 11312, 2015.
- [88] D. Nurul Ashikin Binti, Y. Ooka, T. Tabata, T. Tetsumoto, and T. Tanabe, “Electro-Optic Modulator Based on Photolithography Fabricated p-i-n Integrated Photonic Crystal Nanocavity,” *IEICE Trans. Electron.*, vol. E-100-C, no. 8, pp. 670–674, 2017.
- [89] N. A. B. Daud and T. Tanabe, “Photolithographically fabricated silicon photonic crystal nanocavity photoreceiver with laterally integrated p-i-n diode,” *AIP Adv.*, vol. 8, no. 105224, 2018.
- [90] K. M. Leung and Y. F. Liu, “Full Vector Wave Calculation of Photonic Band Structures in Face-Centered-Cubic Dielectric Media,” *Phys. Rev. Lett.*, vol. 65, no. 21, pp. 2646–2649, 1990.
- [91] K. M. Ho, C. T. Chan, and C. M. Soukoulis, “Existence of a Photonic Gap in Periodic Dielectric Structures,” *Phys. Rev. Lett.*, vol. 65, no. 25, pp. 3152–3155, 1990.
- [92] M. Notomi, K. Yamada, a Shinya, J. Takahashi, C. Takahashi, and I. Yokohama, “Extremely large group velocity dispersion of line-defect waveguides in photonic crystal slabs,” *Phys. Rev. Lett.*, vol. 87253902, pp. 1–4, 2001.
- [93] M. Notomi, A. Shinya, S. Mitsugi, E. Kuramochi, and H. Ryu, “Waveguides , resonators and their coupled elements in photonic crystal slabs,” *Opt. Express*, vol. 12, no. 8, pp. 1551–1561, 2004.
- [94] K. Srinivasan and O. Painter, “Momentum space design of high-Q photonic crystal optical cavities,” *Opt. Express*, vol. 10, no. 15, pp. 670–684, Jul. 2002.
- [95] K. Srinivasan, P. E. Barclay, M. Borselli, and O. Painter, “Optical-fiber-based measurement of an ultrasmall volume high- Q photonic crystal microcavity,” *Phys. Rev. B*, vol. 70, no. 081306, pp. 1–4, 2004.
- [96] P. Russell, “Photonic Crystal Fibers,” *Rev. Appl. Phys.*, vol. 299, pp. 358–362, 2003.
- [97] J. C. Knight, “Photonic crystal fibres,” *Nature*, vol. 424, no. August, pp. 847–851, 2003.
- [98] P. S. J. Russell, “Photonic-Crystal Fibers,” *J. Light. Technol.*, vol. 24, no. 12, pp. 4729–4749, 2006.
- [99] M. A. Mccord and M. J. Rooks, “SPIE Handbook of Microlithography , Micromachining and Microfabrication Volume 1 : Microlithography Chapter 2 E Beam Lithography,” in *SPIE*, vol. 1, 2000.
- [100] L. Zhou and A. W. Poon, “Silicon electro-optic modulators using p-i-n diodes embedded 10-micron-diameter microdisk resonators,” *Opt. Express*, vol. 14, no. 15, pp. 6851–6857,

- 2006.
- [101] B. Schmidt, Q. Xu, J. Shakya, S. Manipatruni, and M. Lipson, “Compact electro-optic modulator on silicon-on-insulator substrates using cavities with ultra-small modal volumes,” *Opt. Express*, vol. 15, no. 6, pp. 3140–3148, 2007.
 - [102] M. Gnan, S. Thoms, D. S. Macintyre, R. M. D. La Rue, and M. Sorel, “Fabrication of low-loss photonic wires in silicon-on-insulator using hydrogen silsesquioxane electron-beam resist,” *Electron. Lett.*, vol. 44, no. 2, 2008.
 - [103] B. Berčič, “Introduction to Electron Beam Lithography.” p. www.optik.uni-erlangen.de/odem/download/v43/v43_el.
 - [104] N. D. Lai *et al.*, “Fabrication of Two- and Three-Dimensional Photonic Crystals and Photonic Quasi-Crystals by Interference Technique,” *Hologr. Res. Technol.*, no. INTECH book, pp. 253–278, 2011.
 - [105] A. J. Wolf, H. Hauser, V. Kübler, C. Walk, O. Höhn, and B. Bläsi, “Origination of nano- and microstructures on large areas by interference lithography,” *Microelectron. Eng.*, vol. 98, pp. 293–296, 2012.
 - [106] B. Bläsi, N. Tucher, O. Höhn, V. Kübler, T. Kroyer, and C. Wellens, “Large area patterning using interference and nanoimprint lithography,” in *proceedings of SPIE 9888, Micro-Optics 2016*, 2016, no. 98880H.
 - [107] A. Fernandez *et al.*, “Use of interference lithography to pattern arrays of submicron resist structures for field emission flat panel displays,” *J. Vac. Sci. Technol. B Microelectron. Nanom. Struct. Process. Meas. Phenom.*, vol. 15, no. 729, pp. 729–735, 1997.
 - [108] T. Kondo, S. Juodkazis, V. Mizeikis, and H. Misawa, “Holographic lithography of periodic two- and three-dimensional microstructures in photoresist SU-8,” *Opt. Express*, vol. 14, no. 17, pp. 7943–7953, 2006.
 - [109] C. W. Hsu *et al.*, “Observation of trapped light within the radiation continuum,” *Nature*, vol. 499, pp. 188–191, 2013.
 - [110] L. Liu *et al.*, “Large area and deep sub-wavelength interference lithography employing odd surface plasmon modes,” *Sci. Rep.*, vol. 6, no. 30450, pp. 1–8, 2016.
 - [111] C. G. Willson, R. R. Dammel, and A. Reiser, “Photoresist materials: a historical perspective,” in *proceedings of SPIE 3051, Optical Microlithography X*, 1997.
 - [112] A. del Campo and E. Arzt, “Fabrication Approaches for Generating Complex Micro- and Nanopatterns on Polymeric Surfaces,” *Chem. Rev.*, vol. 108, pp. 911–945, 2008.
 - [113] F. Yang, K.-P. Ma, Y. Qian, and T. Itoh, “A Uniplanar Compact Photonic-Bandgap (UC-PBG) Structure and Its Applications for Microwave Circuits,” *IEEE Trans. Microw. Theory Tech.*, vol. 47, no. 8, pp. 1509–1514, 1999.
 - [114] B. Jo, L. M. Van Lerberghe, K. M. Motsegood, and D. J. Beebe, “Three-Dimensional Micro-Channel Fabrication in Polydimethylsiloxane (PDMS) Elastomer,” *J. Microelectromechanical Syst.*, vol. 9, no. 1, pp. 76–81, 2000.
 - [115] S. K. Selvaraja, P. Jaenen, W. Bogaerts, D. Van Thourhout, P. Dumon, and R. Baets, “Fabrication of Photonic Wire and Crystal Circuits in Silicon-on-Insulator Using 193-nm Optical Lithography,” *J. Light. Technol.*, vol. 27, no. 18, pp. 4076–4083, 2009.

- [116] H. Kim *et al.*, “Structural colour printing using a magnetically tunable and lithographically fixable photonic crystal,” *Nat. Photonics*, vol. 3, pp. 534–540, 2009.
- [117] Y. Ooka, T. Tetsumoto, N. A. B. Daud, and T. Tanabe, “Ultrasmall in-plane photonic crystal demultiplexers fabricated with photolithography,” *Opt. Express*, vol. 25, no. 2, pp. 1521–1528, 2017.
- [118] M. Settle, M. Salib, A. Michaeli, and T. F. Krauss, “Low loss silicon on insulator photonic crystal waveguides made by 193nm optical lithography,” *Opt. Express*, vol. 14, no. 6, pp. 2440–2445, 2006.
- [119] S. Cheung, T. Su, K. Okamoto, and S. J. B. Yoo, “Ultra-Compact Silicon Photonic 512 x 512 25GHz Arrayed Waveguide Grating Router,” *IEEE J. Sel. Top. Quantum Electron.*, vol. 20, no. 4, 2014.
- [120] Y. Ooka, N. A. B. Daud, T. Tetsumoto, and T. Tanabe, “Compact resonant electro-optic modulator using randomness of a photonic crystal waveguide,” *Opt. Express*, vol. 24, no. 10, pp. 11199–11207, 2016.
- [121] S. P. Anderson and P. M. Fauchet, “Ultra-low power modulators using MOS depletion in a high-Q SiO₂-clad silicon 2-D photonic crystal resonator,” *Opt. Express*, vol. 18, no. 18, pp. 19129–19140, 2010.
- [122] I. Märki *et al.*, “Optically tunable microcavity in a planar photonic crystal silicon waveguide buried in oxide,” *Opt. Lett.*, vol. 31, no. 4, pp. 513–515, 2006.
- [123] C. A. Barrios, V. R. De Almeida, and M. Lipson, “Low-power-consumption short-length and high-modulation-depth silicon electrooptic modulator,” *J. Light. Technol.*, vol. 21, no. 4, pp. 1089–1098, 2003.
- [124] W. M. J. Green, M. J. Rooks, L. Sekaric, and Y. A. Vlasov, “Ultra-compact, low RF power, 10 Gb/s silicon Mach-Zehnder modulator,” *Opt. Express*, vol. 15, no. 25, pp. 17106–17113, 2007.
- [125] K. Ohashi *et al.*, “On-chip optical interconnect,” *Proc. IEEE*, vol. 97, no. 7, pp. 1186–1196, 2009.
- [126] D. A. B. Miller, “Energy consumption in optical modulators for interconnects,” *Opt. Express*, vol. 20, no. S2, pp. A293–A308, 2012.
- [127] J. Liu, D. Pan, S. Jongthammanurak, K. Wada, L. C. Kimerling, and J. Michel, “Design of monolithically integrated GeSi electro-absorption modulators and photodetectors on a SOI platform,” *Opt. Express*, vol. 15, no. 2, pp. 623–628, 2007.
- [128] J. Liu *et al.*, “Waveguide-integrated, ultralow-energy GeSi, electroabsorption modulators,” *Nat. Photonics*, vol. 2, pp. 433–437, 2008.
- [129] L. Lever *et al.*, “Modulation of the absorption coefficient at 1.3 μ m in Ge/SiGe multiple quantum well heterostructures on silicon,” *Opt. Lett.*, vol. 36, no. 21, pp. 4158–4160, 2011.
- [130] P. Chaisakul *et al.*, “23 GHz Ge/SiGe multiple quantum well electro-absorption modulator,” *Opt. Express*, vol. 20, no. 3, pp. 3219–3224, 2012.
- [131] E. H. Edwards *et al.*, “Low-voltage broad-band electroabsorption from thin Ge/SiGe quantum wells epitaxially grown on silicon,” *Opt. Express*, vol. 21, no. 1, pp. 867–876, 2013.

- [132] M. Hochberg *et al.*, “Terahertz all-optical modulation in a silicon-polymer hybrid system,” *Nat. Mater.*, vol. 5, no. 9, pp. 703–709, 2006.
- [133] J.-M. Brosi, C. Koos, L. C. Andreani, M. Waldow, J. Leuthold, and W. Freude, “High-speed low-voltage electro-optic modulator with a polymer-infiltrated silicon photonic crystal waveguide,” *Opt. Express*, vol. 16, no. 6, pp. 4177–4191, 2008.
- [134] R. Ding *et al.*, “Demonstration of a low $V \pi$ L modulator with GHz bandwidth based on electro-optic polymer-clad silicon slot waveguides,” *Opt. Express*, vol. 18, no. 15, pp. 15618–15623, 2010.
- [135] C. Y. Lin *et al.*, “Electro-optic polymer infiltrated silicon photonic crystal slot waveguide modulator with 23 dB slow light enhancement,” *Appl. Phys. Lett.*, vol. 97, no. 093304, pp. 2–5, 2010.
- [136] M. Gould *et al.*, “Silicon-polymer hybrid slot waveguide ring-resonator modulator,” *Opt. Express*, vol. 19, no. 5, pp. 3952–3961, 2011.
- [137] M. J. R. Heck *et al.*, “Hybrid silicon photonics for optical interconnects,” *IEEE J. Sel. Top. Quantum Electron.*, vol. 17, no. 2, pp. 333–346, 2011.
- [138] Y. Tang, J. D. Peters, and J. E. Bowers, “Over 67 GHz bandwidth hybrid silicon electroabsorption modulator with asymmetric segmented electrode for 1.3 μm transmission,” *Opt. Express*, vol. 20, no. 10, pp. 11529–11535, 2012.
- [139] A. Abbasi *et al.*, “Direct and Electroabsorption Modulation of a III-V-on-Silicon DFB Laser at 56 Gb/s,” *IEEE J. Sel. Top. Quantum Electron.*, vol. 23, no. 6, 2017.
- [140] A. Liu *et al.*, “A high-speed silicon optical modulator based on a metal – oxide – semiconductor capacitor,” *Nature*, vol. 427, no. February, pp. 615–618, 2004.
- [141] L. Liao *et al.*, “High speed silicon Mach-Zehnder modulator,” *Opt. Express*, vol. 13, no. 8, pp. 3129–3135, 2005.
- [142] A. Liu *et al.*, “High-speed optical modulation based on carrier depletion in a silicon waveguide,” *Opt. Express*, vol. 15, no. 2, pp. 660–8, 2007.
- [143] L. Liou *et al.*, “40 Gbit/s silicon optical modulator for high-speed applications,” *Electron. Lett.*, vol. 43, no. 22, 2007.
- [144] D. J. Thomson *et al.*, “50-Gb / s Silicon Optical Modulator,” *IEEE Photonics Technol. Lett.*, vol. 24, no. 4, pp. 234–236, 2012.
- [145] Q. Xu, S. Manipatruni, B. Schmidt, J. Shakya, and M. Lipson, “12.5 Gbit/s carrier-injection-based silicon microring silicon modulators,” *Opt. Express*, vol. 15, no. 2, pp. 430–436, 2007.
- [146] P. Dong *et al.*, “Low V_{pp} , ultralow-energy, compact, high-speed silicon electro-optic modulator,” *Opt. Express*, vol. 17, no. 25, pp. 22484–22490, 2009.
- [147] L. Liao *et al.*, “High speed silicon Mach-Zehnder modulator,” *Opt. Express*, vol. 13, no. 8, pp. 3129–3135, 2005.
- [148] T. Sakamoto, T. Kawanishi, and M. Izutsu, “Asymptotic formalism for ultraflat optical frequency comb generation using a Mach – Zehnder modulator,” *Opt. Lett.*, vol. 32, no. 11, pp. 1515–1517, 2007.
- [149] P. Dong, L. Chen, and Y. Chen, “High-speed low-voltage single-drive push-pull silicon

- Mach-Zehnder modulators,” *Opt. Express*, vol. 20, no. 6, pp. 6163–6169, 2012.
- [150] C. Haffner *et al.*, “All-plasmonic Mach-Zehnder modulator enabling optical high-speed communication at the microscale,” *Nat. Photonics*, vol. 9, no. 8, pp. 525–528, 2015.
- [151] J. You, M. Park, J. Park, and G. Kim, “12.5 Gbps optical modulation of silicon racetrack resonator based on carrier-depletion in asymmetric p-n diode,” vol. 16, no. 22, pp. 18340–18344, 2008.
- [152] P. Dong *et al.*, “Low V_{pp} , ultralow-energy, compact, high-speed silicon electro-optic modulator,” *Opt. Express*, vol. 17, no. 25, pp. 22484–22490, 2009.
- [153] T. Baba *et al.*, “50-Gb/s ring-resonator-based silicon modulator,” *Opt. Express*, vol. 21, no. 10, pp. 11869–11876, 2013.
- [154] T. Barwicz *et al.*, “Silicon photonics for compact, energy-efficient interconnects,” *J. Opt. Netw.*, vol. 6, no. 1, pp. 63–73, 2007.
- [155] P. Bermel, A. Rodriguez, S. G. Johnson, J. D. Joannopoulos, and M. Soljačić, “Single-photon all-optical switching using waveguide-cavity quantum electrodynamics,” *Phys. Rev. A*, vol. 74, no. 043818, 2006.
- [156] K. Nozaki, A. Shinya, S. Matsuo, T. Sato, E. Kuramochi, and M. Notomi, “Ultralow-energy and high-contrast all-optical switch involving Fano resonance based on coupled photonic crystal nanocavities,” *Opt. Express*, vol. 21, no. 10, pp. 11877–11888, 2013.
- [157] T. P. White, L. O’Faolain, J. Li, L. C. Andreani, and T. F. Krauss, “Silica-embedded silicon photonic crystal waveguides,” *Opt. Express*, vol. 16, no. 21, p. 17076, 2008.
- [158] A. Brimont *et al.*, “Slow-light-enhanced silicon optical modulators under low-drive-voltage operation,” *IEEE Photonics J.*, vol. 4, no. 5, pp. 1306–1315, 2012.
- [159] T. Tamura, K. Kondo, Y. Terada, Y. Hinakura, N. Ishikura, and T. Baba, “Silica-Clad Silicon Photonic Crystal Waveguides for Wideband Dispersion-Free Slow Light,” *J. Light. Technol.*, vol. 33, no. 14, pp. 3034–3040, 2015.
- [160] N. A. B. Daud, Y. Ooka, T. Tabata, T. Tetsumoto, and T. Tanabe, “Electro-Optic Modulator Based on Photolithography Fabricated p-i-n Integrated Photonic Crystal Nanocavity,” *IEICE Trans. Electron.*, vol. E100–C, no. 8, pp. 670–674, 2017.
- [161] Q. Xu, B. Schmidt, S. Pradhan, and M. Lipson, “Micrometre-scale silicon electro-optic modulator,” *Nature*, vol. 435, pp. 325–327, 2005.
- [162] T. Tille, J. Sauerbrey, and D. Schmitt-landsiedel, “A 1.8-V MOSFET-Only $\Sigma\Delta$ Modulator Using Substrate Biased Depletion-Mode MOS Capacitors in Series Compensation,” *IEEE J. Solid-State Circuits*, vol. 36, no. 7, pp. 1041–1047, 2001.
- [163] T. Tanabe, H. Taniyama, and M. Notomi, “Carrier Diffusion and Recombination in Photonic Crystal Nanocavity Optical Switches,” *Cleo/QELS*, vol. 26, no. 11, pp. 3–4, 2008.
- [164] T. H. Windhorn, L. W. Cook, and G. E. Stillman, “Temperature Dependent Electron Velocity-Field Characteristics For In_{0.53}Ga_{0.47}As At High Electric Fields,” *J. Electron. Mater.*, vol. 11, no. 6, pp. 1065–1082, 1982.
- [165] T. J. Faith, R. S. Irvén, S. K. Plante, and J. J. O’Neill, “Contact resistance: Al and Al–Si to diffused N + and P + silicon,” *J. Vac. Sci. Technol. A Vacuum, Surfaces, Film.*, vol. 1, no. 2, pp. 443–448, 1983.

- [166] Y. Terada, H. Ito, H. C. Nguyen, and T. Baba, “Theoretical and experimental investigation of low-voltage and low-loss 25-Gbps Si photonic crystal slow light Mach-Zehnder modulators with interleaved p/n junction,” *Front. Phys.*, vol. 2, no. November, pp. 1–9, 2014.
- [167] M. Lipson, “Guiding, modulating and emitting light on silicon—challenges and opportunities,” *J. Light. Technol.*, vol. 23, no. 12, pp. 4222–4238, 2005.
- [168] R. Soref, “The past, present, and future of silicon photonics,” *IEEE J. Sel. Top. Quantum Electron.*, vol. 12, no. 6, pp. 1678–1687, 2006.
- [169] D. A. B. Miller, “Device requirements for optical interconnects to silicon chips,” *Proc. IEEE*, vol. 97, no. 7, pp. 1166–1185, 2009.
- [170] L. Haret, T. Tanabe, E. Kuramochi, and M. Notomi, “Extremely low power optical bistability in silicon demonstrated using 1D photonic crystal nanocavity,” *Opt. Express*, vol. 17, no. 23, pp. 21108–21117, 2009.
- [171] P. Dong *et al.*, “Low V_{π} , ultralow-energy, compact, high-speed silicon electro-optic modulator,” *Opt. Express*, vol. 17, no. 25, pp. 22484–22490, 2009.
- [172] G. T. Reed, G. Mashanovich, F. Y. Gardes, and D. J. Thomson, “Silicon optical modulators,” *Nat. Photonics*, vol. 4, pp. 518–526, 2010.
- [173] D. M. Gill *et al.*, “Internal Bandwidth Equalization in a CMOS-Compatible Si-Ri Modulator,” *IEEE Photonics Technol. Lett.*, vol. 21, no. 4, pp. 200–202, 2009.
- [174] C. Gunn, “CMOS photonics for high-speed interconnects,” *IEEE Micro*, vol. 26, no. 2, pp. 58–66, 2006.
- [175] L. Tang *et al.*, “Nanometre-scale germanium photodetector enhanced by a near-infrared dipole antenna,” *Nat. Photonics*, vol. 2, no. April, pp. 226–229, 2008.
- [176] Y. Kang *et al.*, “Monolithic germanium/silicon avalanche photodiodes with 340 GHz gain–bandwidth product,” *Nat. Photonics*, vol. 3, pp. 59–63, 2009.
- [177] X. Wang, Z. Cheng, K. Xu, H. K. Tsang, and J.-B. Xu, “High-responsivity graphene/silicon-heterostructure waveguide photodetectors,” *Nat. Photonics*, vol. 7, no. September, pp. 1–4, 2013.
- [178] A. Pospischil *et al.*, “CMOS-compatible graphene photodetector covering all optical communication bands,” *Nat. Photonics*, vol. 7, pp. 892–896, 2013.
- [179] L. Zimmermann, G. B. Preve, T. Tekin, T. Rosin, and K. Landles, “Packaging and Assembly for Integrated Photonics — A Review of the ePIXpack Photonics Packaging Platform,” *IEEE J. Sel. Top. Quantum Electron.*, vol. 17, no. 3, pp. 645–651, 2011.
- [180] A. E. Lim *et al.*, “Review of Silicon Photonics Foundry Efforts,” *IEEE J. Sel. Top. Quantum Electron.*, vol. 20, no. 4, 2014.
- [181] M. W. Geis *et al.*, “CMOS-compatible all-Si high-speed waveguide photodiodes with high responsivity in near-infrared communication band,” *IEEE Photonics Technol. Lett.*, vol. 19, no. 3, pp. 152–154, 2007.
- [182] J. Bravo-Abad, E. P. Ippen, and M. Soljačić, “Ultrafast photodetection in an all-silicon chip enabled by two-photon absorption,” *Appl. Phys. Lett.*, vol. 94, no. 24, 2009.
- [183] M. Casalino, G. Coppola, R. M. D. La Rue, and D. F. Logan, “State-of-the-art all-silicon

- sub-bandgap photodetectors at telecom and datacom wavelengths,” *Laser Photonics Rev.*, vol. 10, no. 6, pp. 895–921, 2016.
- [184] H. Y. Fan and A. K. Ramdas, “Infrared Absorption and Photoconductivity in Irradiated Silicon,” *J. Appl. Phys.*, vol. 30, no. 1127, 1959.
- [185] Y. Liu, C. W. Chow, W. Y. Cheung, and H. K. Tsang, “In-line channel power monitor based on helium ion implantation in silicon-on-insulator waveguides,” *IEEE Photonics Technol. Lett.*, vol. 18, no. 17, pp. 1882–1884, 2006.
- [186] A. P. Knights *et al.*, “Silicon-on-insulator waveguide photodetector with self-ion-implantation- engineered-enhanced infrared response,” *J. Vac. Sci. Technol. A Vacuum, Surfaces Film.*, vol. 24, no. 3, pp. 783–786, 2006.
- [187] J. K. Doyle, P. E. Jessop, and A. P. Knights, “Silicon photonic resonator-enhanced defect- mediated photodiode for sub-bandgap detection,” *Opt. Express*, vol. 18, no. 14, pp. 14671–14678, 2010.
- [188] M. Koshiya, “Wavelength Division Multiplexing and Demultiplexing With Photonic Crystal Waveguide,” *J. Light. Technol.*, vol. 19, no. 12, pp. 1970–1975, 2001.
- [189] B. Momeni *et al.*, “Compact wavelength demultiplexing using focusing negative index photonic crystal superprisms,” *Opt. Express*, vol. 14, no. 6, p. 2413, 2006.
- [190] A. Y. Piggott, J. Lu, K. G. Lagoudakis, J. Petykiewicz, T. M. Babinec, and J. Vuckovic, “Inverse design and demonstration of a compact and broadband on-chip wavelength demultiplexer,” *Nat. Photonics*, vol. 9, no. June, pp. 374–378, 2015.
- [191] Y. Vlasov, W. M. J. Green, and F. Xia, “High-throughput silicon nanophotonic wavelength-insensitive switch for on-chip optical networks,” *Nat. Photonics*, vol. 2, no. April, pp. 242–246, 2008.
- [192] N. Duan, T.-Y. Liow, A. E.-J. Lim, L. Ding, and G. Q. Lo, “310 GHz gain-bandwidth product Ge-Si avalanche photodetector for 1550 nm light detection,” *Opt. Express*, vol. 20, no. 10, p. 11031, 2012.
- [193] D. Zhang *et al.*, “High-responsivity GeSn short-wave infrared p-i-n photodetectors,” *Appl. Phys. Lett.*, vol. 102, no. 141111, 2013.
- [194] A. Novack *et al.*, “Germanium photodetector with 60 GHz bandwidth using inductive gain peaking,” *Opt. Express*, vol. 21, no. 23, pp. 28387–28393, 2013.
- [195] P. Chaisakul *et al.*, “Integrated germanium optical interconnects on silicon substrates,” *Nat. Photonics*, vol. 8, no. 6, pp. 482–488, 2014.
- [196] M. W. Geis *et al.*, “All silicon infrared photodiodes: photo response and effects of processing temperature,” *Opt. Express*, vol. 15, no. 25, pp. 16886–16895, 2007.
- [197] R. R. Grote, K. Padmaraju, B. Souhan, J. B. Driscoll, K. Bergman, and R. M. Osgood, “10 Gb / s Error-Free Operation of All-Silicon Ion-Implanted-Waveguide Photodiodes at 1.55 μm ,” *IEEE Photonics Technol. Lett.*, vol. 25, no. 1, pp. 67–70, 2013.
- [198] M. Notomi, A. Shinya, S. Mitsugi, G. Kira, E. Kuramochi, and T. Tanabe, “Optical bistable switching action of Si high-Q photonic-crystal nanocavities,” *Opt. Express*, vol. 13, no. 7, pp. 2678–2687, 2005.
- [199] T. Uesugi, B. Song, T. Asano, and S. Noda, “Investigation of optical nonlinearities in an

- ultra-high- Q Si nanocavity in a two-dimensional photonic crystal slab,” *Opt. Express*, vol. 14, no. 1, pp. 377–386, 2006.
- [200] T. Tanabe, H. Sumikura, H. Taniyama, A. Shinya, and M. Notomi, “All-silicon sub-Gb/s telecom detector with low dark current and high quantum efficiency on chip,” *Appl. Phys. Lett.*, vol. 96, no. 10, p. 101103, Feb. 2010.
- [201] M. Lundstrom, “Moore’s Law Forever?,” *Science (80-.)*, vol. 299, no. 5604, pp. 210–212, 2003.
- [202] J. R. Powell, “The Quantum Limit to Moore’s Law,” *Proceeding IEEE*, vol. 96, no. 8, pp. 1247–1248, 2008.
- [203] N. Savage, “Linking with light,” *IEEE Spectr.*, vol. 39, no. 8, pp. 32–36, 2002.
- [204] K. W. Goossen *et al.*, “GaAs MQW Modulators Integrated with Silicon CMOS,” *IEEE Photonics Technol. Lett.*, vol. 7, no. 4, pp. 360–362, 1995.
- [205] S. Assefa *et al.*, “A 90nm CMOS Integrated Nano-Photonics Technology for 25Gbps WDM Optical Communications Applications,” in *2012 International Electron Devices Meeting*, 2012, pp. 809–811.
- [206] Y. A. Vlasov and S. J. McNab, “Losses in single-mode silicon-on-insulator strip waveguides and bends,” *Opt. Express*, vol. 12, no. 8, pp. 1622–1631, 2004.
- [207] M. H. R. Lankhorst, B. W. S. M. M. Ketelaars, and R. A. M. Wolters, “Low-cost and nanoscale non-volatile memory concept for future silicon chips,” *Nat. Mater.*, vol. 4, no. 4, pp. 347–352, 2005.
- [208] W. Bogaerts *et al.*, “Nanophotonic waveguides in silicon-on-insulator fabricated with CMOS technology,” *J. Light. Technol.*, vol. 23, no. 1, pp. 401–412, 2005.
- [209] Y. Takahashi, Y. Inui, M. Chihara, T. Asano, R. Terawaki, and S. Noda, “A micrometre-scale Raman silicon laser with a microwatt threshold,” *Nature*, vol. 498, no. 7455, pp. 470–474, Jun. 2013.
- [210] H. K. Tsang *et al.*, “Optical dispersion, two-photon absorption and self-phase modulation in silicon waveguides at 1.5 μ m wavelength,” *Appl. Phys. Lett.*, vol. 80, no. 3, pp. 416–418, 2002.
- [211] E. Kuramochi, M. Notomi, S. Hughes, A. Shinya, T. Watanabe, and L. Ramunno, “Disorder-induced scattering loss of line-defect waveguides in photonic crystal slabs,” *Phys. Rev. B - Condens. Matter Mater. Phys.*, vol. 72, no. 16, pp. 2–5, 2005.
- [212] S. Hughes, L. Ramunno, J. F. Young, and J. E. Sipe, “Extrinsic Optical Scattering Loss in Photonic Crystal Waveguides : Role of Fabrication Disorder and Photon Group Velocity,” *Phys. Rev. Lett.*, vol. 94, no. 033903, pp. 1–4, 2005.
- [213] T. Schwartz, G. Bartal, S. Fishman, and M. Segev, “Transport and Anderson localization in disordered two-dimensional photonic lattices,” *Nature*, vol. 446, no. March, pp. 52–55, 2007.
- [214] M. Patterson and S. Hughes, “Disorder-Induced Coherent Scattering in Slow-Light Photonic Crystal Waveguides,” *Phys. Rev. Lett.*, vol. 102, no. 253903, pp. 1–4, 2009.
- [215] N. Mann, A. Javadi, P. D. Garc, P. Lodahl, and S. Hughes, “Theory and experiments of disorder-induced resonance shifts and mode-edge broadening in deliberately disordered

- photonic crystal waveguides,” *Phys. Rev. A*, vol. 92, no. 023849, pp. 1–9, 2015.
- [216] H. C. Nguyen, Y. Sakai, M. Shinkawa, N. Ishikura, and T. Baba, “10 Gb/s operation of photonic crystal silicon optical modulators,” *Opt. Express*, vol. 19, no. 14, pp. 13000–13007, 2011.
- [217] N. Izhaky *et al.*, “Development of CMOS-Compatible Integrated Silicon Photonics Devices,” vol. 12, no. 6, pp. 1688–1698, 2006.
- [218] M. Haurylau *et al.*, “On-Chip Optical Interconnect Roadmap : Challenges and Critical Directions,” vol. 12, no. 6, pp. 1699–1705, 2006.
- [219] M. Notomi, A. Shinya, and E. Kuramochi, “Photonic Crystals: Towards Ultrasmall Lightwave Circuits,” *NTT Tech. Rev.*, vol. 2, no. 2, pp. 36–47, 2004.
- [220] Y. Terada, K. Miyasaka, K. Kondo, N. Ishikura, T. Tamura, and T. Baba, “Optimized optical coupling to silica-clad photonic crystal waveguides,” *Opt. Lett.*, vol. 42, no. 22, pp. 4695–4698, 2017.

Acknowledgments

All praise to Allah s.w.t the Almighty, for giving me the blessing, the strength, the chance and endurance to complete this study. Without His graces and blessing, this study would not have been possible.

I would like to express my sincere gratitude to my supervisor Professor Takasumi Tanabe for the continuous support of my doctoral study, for his patience and time, for his high motivation and encouragement even during my grimmest of time, and his immense knowledge. His guidance helped me in all the time of research and writing of this thesis. Due to his unyielding belief in my ability, I manage to complete this study.

Besides my advisor, I would also like to acknowledge the rest of my thesis committee; Prof. Naoki Yamanaka, Prof. Ryogo Kubo and Prof. Takeshi Kinoshita, for their insightful comments and encouragement, which incited me to widen my research from various perspective. Also, Dr. Satoki Kawanishi who has shared his knowledge and experience in improvising the thesis.

My doctoral study would be impossible without the financial support from Malaysia-Japan Higher Education Programme (MJHEP) scholarship, 研究のすゝめ奨学金 and 田村淳記念奨学金. I also would like to thank Keio University Doctorate Student Grant-in-Aid Program (KLL) by financially supporting my doctoral research activities.

I am also indebted with previous PhC team colleague, Mr. Yuta Ooka and Dr. Tomohiro Tetsumoto who has given me a great deal of input in my early years of conducting the experiment, analysing the experimental result and their credible ideas and information during group meeting discussion. Also, to former bachelor student, Mr. Tomohisa Tabata who has conducted the early measurement of photodetector and Mr. Hajime Kumazaki who has helped me designed the experimental setup in conducting the transceiver demonstration.

I have great pleasure in acknowledging my gratitude to all PhC group members for the stimulating discussions during the weekly team meeting and to all members of Tanabe Laboratory. They have made my stay here very pleasant and also for helping me to use some of the measurement instrument.

My doctoral study is the toughest phase in my life since it coincided with the early phase of my marriage and of giving birth to my child. Being a mother and a doctoral student on the same time is full of struggles. I would not able to surpass this without the assistant of countless individuals who has aided in my daily life.

I would like to thank to my Malaysian colleagues in Keio University – Adni, Iza and Siti who has helped me a lot during my first-year life in Keio University. Also, to my fellow Malaysian friends who lived all around Japan. Thank you for their warm friendship and support which had made my live in Japan more delightful. Many thanks to my *usrah* mates in Japan – Kak Hana, Kak Fiza, Illany, Asma, Mawaddah, Nadia, Anugerah and Syazana for their understanding and companion. Also, for others who I did not specifically mentioned here.

ACKNOWLEDGEMENTS

My acknowledgement would be incomplete without thanking the biggest source of my strength, my family. Of course, to stay for almost 10 years abroad requires a lot of understanding and support from family and relatives. The blessing and prayers of my parents, parent's in-law and the love and care of my sister have made a tremendous contribution in helping me reach this stage of life. I thank them for putting up with me in difficult moments where I felt stumped and for goading me on to follow my dream. I dedicate this work to you all.

I also dedicate this Ph.D thesis to my cheerful daughter, Nihlah Insyirah who is the pride and joy of my life. I appreciate all your patience and support during my Ph.D studies especially in my final year.

Last but not the least, to my soul mate, my dearest husband and my best friend, Atiq. Thank you for everything, for being so understanding and for putting up with me through the toughest moments of my life especially in our early parenthood and on the same time as a doctoral student. I thank Allah for enlightening my life with your presence.

List of publications

Journal papers (related to this thesis)

- [1] N.A.B. Daud, Y. Ooka, T. Tabata, T. Tetsumoto, and T. Tanabe, “Electro-Optic Modulator Based on Photolithography Fabricated p-i-n Integrated Photonic Crystal Nanocavity,” IEICE Trans. Electron., vol. E100–C, no. 8, pp. 670–674, 2017.
- [2] N. A. B. Daud and T. Tanabe, “Photolithographically fabricated silicon photonic crystal nanocavity photoreceiver with laterally integrated p-i-n diode,” AIP Adv., vol. 8, no. 105224, 2018.

Other journal papers

- [1] Y. Ooka, N. A. B. Daud, T. Tetsumoto and, T. Tanabe, “Compact resonant electro-optic modulator using randomness of a photonic crystal waveguide,” Opt. Express, Vol. 24, No. 10, pp. 11199-11207 (2016).
- [2] Y.Ooka, T. Tetsumoto, N. A. B. Daud, and T. Tanabe, “Ultrasmall in-plane photonic crystal demultiplexers fabricated with photolithography,” Opt. Express, Vol. 25, No. 2, pp. 1521-1528 (2017).

International conferences

- [1] Y. Ooka, N. A. B. Daud, T. Tetsumoto, and T. Tanabe, "Efficient electro-optic modulation of a weakly localized resonance in a photonic crystal waveguide," *Frontiers in Optic/Laser Science Conference (FiO/LS)*, FTu5C.6, San Jose, October 18-22 (2015).
- [2] T. Tanabe, T. Tetsumoti, Y. Ooka, and N. A. B. Daud, "Recent progress on high-Q photonic crystal nanocavities: Photolithographic fabrication and reconfigurable system," *Progress In Electromagnetics Research Symposium (PIERS2016)*, SC3, Shanghai, August 8-11 (2016). (invited)
- [3] N. A. B. Daud, Y. Ooka, and T. Tanabe, "p-i-n integrated photonic crystal nanocavity optical functional device," *The 5th Advances Laser and Photon Sources Conference (ALPS' 16)*, ALPSp14-03, Yokohama, Japan, May 17-20 (2016).
- [4] Y. Ooka, N. A. B. Daud, T. Tetsumoto, and T. Tanabe, "Ultrasmall in-plane photonic crystal demultiplexer fabricated with photolithography," *Frontiers in Optics/Laser Science Conference (FiO/LS)*, FTu2D.3, Rochester, October 17-21 (2016).
- [5] N. A. B. Daud, Y. Ooka, T. Tetsumoto, and T. Tanabe, "Photonic crystal nanocavity photodetector integrated with p-i-n junction fabricated by photolithography process," *International Conference on Nano-photonics and Nano-optoelectronics (ICNN2017)*, ICNN8-3, Yokohama, Japan, April 18-21 (2017).
- [6] T. Tetsumoto, N. A. B. Daud, Y. Ooka, N. Kamioka, T. Okamura, and T. Tanabe, "A CMOS compatible in-plane compact wavelength demultiplexer based on photonic crystal nanocavities," *International Conference on Nano-photonics and Nano-optoelectronics (ICNN2017)*, ICNN2-5, Yokohama, Japan, April 18-21 (2017).
- [7] N. A. B. Daud, Y. Ooka, T. Tetsumoto, and T. Tanabe, "SiO₂ clad active and passive photonic crystal nanocavity devices fabricated with photolithography," *The Pacific Rim Conferences on Lasers and Electro-Optics (CLEO-Pacific Rim 2017)*, P3-119, Singapore, July 31- August 4 (2017).
- [8] T. Tanabe, Y. Ooka, N. A. B. Daud, T. Tetsumoto, "Robust CMOS compatible photonic crystal nanocavity and DEMUX filter," *Asia Communications and Photonics Conference (ACP) 2017*, M1F.1, Guangzhou, 10-13 November (2017).
- [9] N. A. B. Daud, T. Tetsumoto, and T. Tanabe, "Photolithographically Fabricated Silicon Photonic Crystal Nanocavity Photoreceiver with a Laterally Integrated Pin Diode," *Progress In Electromagnetics Research Symposium (PIERS)*, 2P15a-3, Toyama, Aug 1-4 (2018).
- [10] S. Jin, Y. Ooka, T. Tetsumoto, N. A. B. Daud, N. Kamioka, T. Okamura, and T. Tanabe, "Improved CMOS compatible photonic crystal demultiplexer," *CLEO Pacific Rim 2018*, W4H.3, HongKong, Jul 29-Aug 3 (2018).

Domestic conferences

- [1] 大岡 勇太, スル アシキン ダウド, 鐵本 智大, 田邊 孝純, フォトニック結晶におけるランダム性の影響とその制御による利用, 第63回応用物理学会春季学術講演会, 東工大大岡山キャンパス, 平成28年1月9日~11日 (2016)
- [2] 金 セイ基, スル アシキン ダウド, 鐵本 智大, 田邊 孝純, フォトリソグラフィによるフォトニック結晶波長分波器の最適化, 第65回応用物理学会春季学術講演会, 早稲田大学 西早稲田キャンパス, 平成30年3月17日~20日 (2018)

Appendix A

Product values of optical equipment's

Name	Model	Abbreviation
Band pass filter	TFF-15-1-PM-L-100-SS	BPF
DC source	Yokogawa GS 610	DC
E-O data converter	PriTel. Inc	E/O Mod.
IR camera	SU320 – KTS	IR
L-band erbium doped fiber amplifier	LNHP-PMFA-18-L	L-EDFA
Optical attenuator	OZ Optics DA-100-SCU-1550-8/125-P-50	VOA
Optical fiber	Single mode, optical fiber SC to SC	-
Optical sampling oscilloscope	Agilent 86100B	OSC
Oscilloscope	Rohde & Schwarz RTE 1104	OSC
Photodetector	Model 1411 20-GHz IR Photodetector	PD
Power meter	Agilent 81634B	PM
Pulse pattern generator	Keysight 81134A	PPG
RF probe (ACP probe)	ACP40-A-GS-150 ACP/10137 SS-200	-
TEC controller	TED200C	TEC
Trans-impedance amplifier	HCA-400M-5K-C DDPCA-300	TIA
Tunable laser source	TSL – 510 (Santec)	TLD

Appendix B

Loss measurement of PhC device

Loss in PhC device that used in this study is discussed in this section. In PhC device which utilize PBG waveguide, radiative loss is the most significant loss. Radiative loss occurs when the mode lies above the light line of the cladding material. Usually this loss is larger than 100 dB/mm [93]. By appropriate employing the device structure to make sure the working area is below the light line, the radiative loss of the device can be reduced. However, for this device, as described by O. Yuta *et. al*, since the PhC waveguide mode is lossless and the perturbation is small, the vertical scattering is kept to a minimum [87], therefore, the radiative loss should not have to be worried.

Another factor, that can contribute to the loss in this device is the coupling loss. Usually, coupling loss between PhC waveguides and single-mode fibers (SMF) is larger than 30 dB, which is unacceptable for practical application [219]. However, in the device that used in this study, the PhC structure is incorporating with spot-size converter (SSC) to reduce the coupling loss. Basically, PhC device consists of SSC at input and output facet, Si wire waveguide and PhC waveguide as shown in Fig. B1. Facet of the SSC are formed by deep trench etching of $> 60 \mu\text{m}$ depth. The SSCs consist of Si inverse taper buried by a silica waveguide. The tip width of the inverse taper is $0.20 \mu\text{m}$, and is positioned inside the silica by $0.2 \mu\text{m}$ from the trench-etched facet. The taper length is $199.8 \mu\text{m}$ to reduce loss. To obtained total loss of the device, loss at every part is measured.

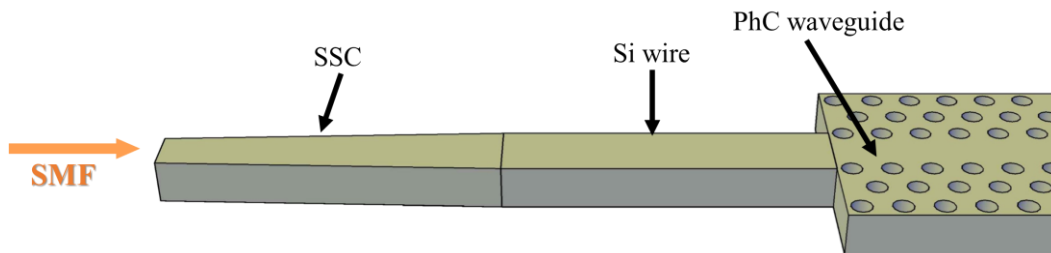


Fig. B-1 Schematic view of spot-size converter (SSC) for PhC waveguide (left).

Figs. B-2 (a) and (b) shows the transmittance spectrum for two different structure. Fig. B-2 (a) is measured transmittance spectrum of structure that only consists of SSC and Si wire waveguide and Fig. B-2 (b) is measured transmittance spectrum of structure as shown in Fig. B-1 that consists of SSC, Si wire waveguide and PhC waveguide. The light intensity from TLD output is kept constant for both measurement with -20 dBm . Loss obtained in Fig. B-2 (a) is -5 dB in which -2.5 dB at each side. In Fig. B-2 (b), loss is -15 dB in which loss at each side is -7.5 dB . Since the measurement device structure of Fig. B-2 (b) consists of SSC and Si wire waveguide, loss of light coupled to PhC waveguide is -5 dB at each side.

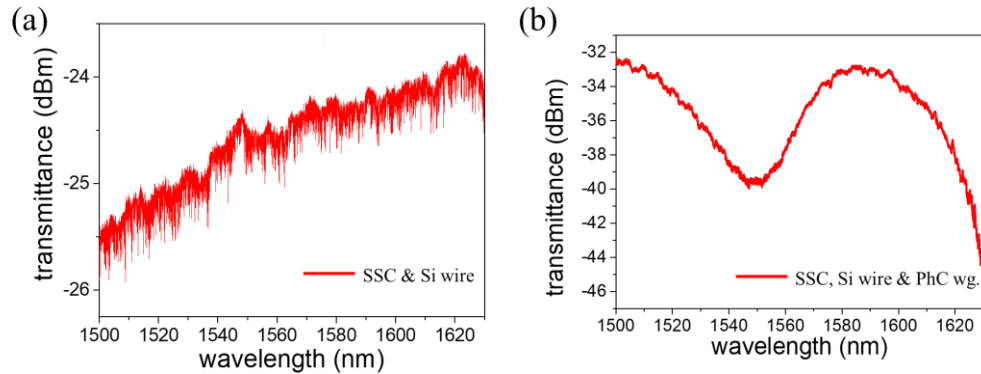


Fig. B-2 (a) Transmittance spectrum measured from a structure that consist only spot-size converter and Si wire waveguide. (b) Transmittance spectrum of structure consist of spot-size converter, Si wire waveguide and PhC waveguide.

Next, total loss of PhC nanocavity device namely consists of SSC, Si wire waveguide, PhC waveguide and nanocavity structure is measured. Fig. B-3 shows the transmittance spectrum when light intensity from TLD output is -20 dBm. It shows total loss of the structure is approximately -35 dB. Based on the loss achieved as shows in Fig. B-2, light coupling loss to the nanocavity structure can be calculated. The value is -2.5 dB loss at each side.

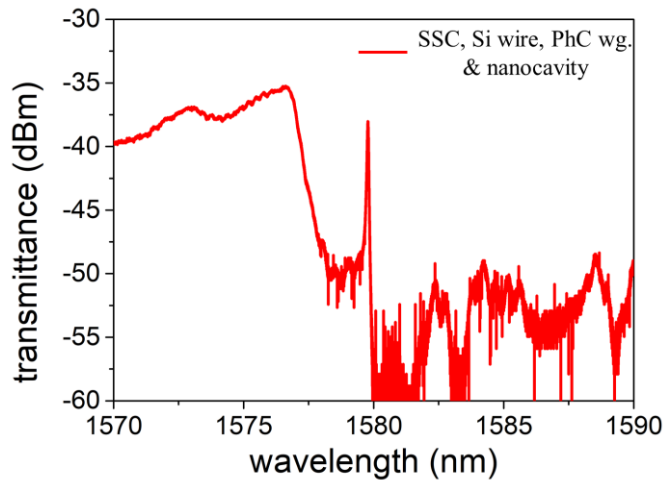


Fig. B-3 Transmission spectrum of PhC nanocavity structure consist of spot-size converter, Si wire, PhC waveguide and nanocavity.

Many researched has been done to minimize light coupling loss in PhC device. In fact, due to the mature of silicon foundry fabrication, integration of SSC into the device makes the coupling loss between single mode fiber with the device as low as -1.6 dB. The value is far lower compared to other PhC devices [93], [219]. However, coupling loss between Si wire waveguide and PhC waveguide can be further improved. Based on Y. Terada *et. al*, if light simply coupled to input/output silicon wire waveguide, more than 4 dB optical loss will occur [220]. They had

proposed a tapered line junction structure from the Si wire waveguide to SiO₂-clad PhC waveguide to reduce the optical loss. This method could far reduce the coupling loss to 0.46 dB.